



저작자표시-비영리-변경금지 2.0 대한민국

이용자는 아래의 조건을 따르는 경우에 한하여 자유롭게

- 이 저작물을 복제, 배포, 전송, 전시, 공연 및 방송할 수 있습니다.

다음과 같은 조건을 따라야 합니다:



저작자표시. 귀하는 원저작자를 표시하여야 합니다.



비영리. 귀하는 이 저작물을 영리 목적으로 이용할 수 없습니다.



변경금지. 귀하는 이 저작물을 개작, 변형 또는 가공할 수 없습니다.

- 귀하는, 이 저작물의 재이용이나 배포의 경우, 이 저작물에 적용된 이용허락조건을 명확하게 나타내어야 합니다.
- 저작권자로부터 별도의 허가를 받으면 이러한 조건들은 적용되지 않습니다.

저작권법에 따른 이용자의 권리는 위의 내용에 의하여 영향을 받지 않습니다.

이것은 [이용허락규약\(Legal Code\)](#)을 이해하기 쉽게 요약한 것입니다.

[Disclaimer](#)

공학박사 학위논문

Computational study of reactions on surfaces

Development of a ReaxFF reactive force field for silicon
dioxide/hydrogen fluoride etching systems and
first-principle calculation of adsorption energies in
lithium-sulfur batteries

계산화학 방법론을 이용한 표면 반응 모사 및
해석에 관한 연구

2021년 8월

서울대학교 대학원

화학생물공학부

김 동 현

Computational study of reactions on surfaces

Development of a ReaxFF reactive force field for silicon
dioxide/hydrogen fluoride etching systems and
first-principle calculation of adsorption energies in
lithium-sulfur batteries

계산화학 방법론을 이용한 표면 반응 모사 및
해석에 관한 연구

지도 교수 이 원 보

이 논문을 공학박사 학위논문으로 제출함
2021 년 8 월

서울대학교 대학원
화학생물공학부
김 동 현

김동현의 공학박사 학위논문을 인준함
2021 년 8 월

위 원 장 _____

부위원장 _____

위 원 _____

위 원 _____

위 원 _____

Abstract

Computational study of reactions on surfaces

Development of a ReaxFF reactive force field for silicon dioxide/hydrogen fluoride etching systems and first-principle calculation of adsorption energies in lithium-sulfur batteries

Dong Hyun Kim

School of Chemical and Biological Engineering

Seoul National University

In this thesis, etching processes with silicon dioxide/hydrogen fluoride gas systems and adsorption mechanisms of lithium polysulfides (LPS) and battery components such as functional binder in sulfur cathode and separator coated with functional metal oxide shields are modelled and calculated with various computational methods.

First, a new ReaxFF reactive force field has been developed to describe reactions in the Si-O-H-F system. The ReaxFF force field parameters have been fitted to a quantum mechanical (QM) training set containing structures and energies related to bond dissociation energies, angle and dihedral distortions, and reactions between silicon dioxide and hydrogen fluoride as well as experimental crystal structures, heats of formation and various reaction mechanisms. Model configurations for the training set were based on density functional theory (DFT) calculations on molecular clusters and periodic bulk and surface systems. ReaxFF reproduces accurately the QM training data for structures and energetics of small

clusters and surfaces. The results of ReaxFF match reasonably well with those of QM for energies of initial etching process, transition state, and final production process. In addition to this, this force field was applied to etching simulations for silicon dioxide and hydrogen fluoride gas. In etching simulations, silicon dioxide slab models with hydrogen fluoride gas were used in molecular dynamics simulations. The etching yield and number of reaction products with different incident energies of hydrogen fluoride etchant are investigated.

Second, the adsorption energies of LPS with functional binder and functional shield in lithium-sulfur batteries were calculated with DFT method. Before various actual evaluations, the chemical adsorption capacity of the prepared polymer binders composed with chitosan and carboxylated nitrile butadiene rubber (XNBR) for LPS (Li_2S_x , $x = 4, 6, 8$) based on DFT calculations. In addition, the adsorption capability of metal oxides to LPS was investigated by predicting the interaction of the as-prepared metal oxides with LPS with DFT calculations. Calculation included well-known metal oxides for comparison. As a result, with computational method, functional binder and functional shield for enhanced lithium-sulfur batteries were investigated.

Keyword : Density Functional Theory, ReaxFF Reactive Force Field, Force Field Parametrization, Multi-Scale Modelling, Etching Process, Li-S Battery

Student Number : 2016–21008

Table of Contents

| | |
|---|-----------|
| List of Figures | v |
| List of Tables | xi |
| Chapter 1. Introduction | 1 |
| 1.1. Overall Introduction | 1 |
| 1.2. Outline | 1 |
| Chapter 2. Theoretical Background for Computational Chemistry.. | 4 |
| 2.1. DFT calculations..... | 4 |
| 2.1.1. Introduction | 4 |
| 2.1.2. Kohn-Sham method..... | 5 |
| 2.2. The ReaxFF reactive force field | 8 |
| 2.2.1. Introduction | 8 |
| 2.2.2. The ReaxFF reactive force field method | 10 |
| 2.2.3. Energy descriptions in ReaxFF..... | 12 |
| Chapter 3. Molecular Dynamics Simulation of Silicon Dioxide Etching by Hydrogen Fluoride Using ReaxFF Reactive Force Field | 16 |
| 3.1. Introduction | 16 |
| 3.2. Simulation model and details | 19 |
| 3.3. Results | 21 |
| 3.4. Summary and discussion | 26 |
| 3.5. Acknowledgement..... | 27 |
| Chapter 4. Adsorption energy calculations in Lithium–Sulfur Batteries..... | 56 |
| 4.1. Elastic chitosan based lean content binder | 56 |
| 4.1.1. Introduction | 56 |
| 4.1.2. Model and computational method..... | 58 |
| 4.1.3. Results | 60 |
| 4.1.4. Conclusions | 64 |
| 4.1.5. Acknowledgement..... | 64 |
| 4.2. Multifunctional Ga ₂ O ₃ shield for Li-S batteries | 75 |
| 4.2.1. Introduction | 75 |
| 4.2.2. Model and computational method | 75 |

| | |
|-------------------------------------|------------|
| 4.2.3. Results | 77 |
| 4.2.4. Conclusions | 83 |
| 4.2.5. Acknowledgement..... | 84 |
| Chapter 5. Conclusions | 101 |
| Bibliography..... | 103 |
| 국문 초록 | 115 |

List of Figures

| | |
|---|----|
| Figure 1.1. Various computational methods according to the scale of simulation..... | 3 |
| Figure 3.1. Minimum energy difference calculated using DFT and ReaxFF of (a) bond dissociation between Si and F for SiF ₄ , (b) valence angle distortion between (F-Si-F) for SiF ₄ , (c) bond dissociation between Si and F for SiO ₂ cluster containing two Si-F bonds, and (d) bond dissociation between Si and F for SiO ₂ cluster containing three Si-F bonds. | 28 |
| Figure 3.2. Four subsequent reactions forming SiF ₄ using SiO ₂ cluster model: HF reacting with (a) Si ₄ O ₁₀ H ₄ , (b) F-Si ₄ O ₉ H ₃ , (c) F ₂ -Si ₄ O ₉ H ₄ , and (d) F ₃ -Si ₄ O ₉ H ₅ | 29 |
| Figure 3.3. Early stage reactions using SiO ₂ slab model. (a) HF reacts with surface forming one Si-F bond and one O-H bond where -Si* and -O* represent reactions sites. (b) HF reacts with surface containing one Si-F bond and one O-H bond forming additional Si-F bond in the same Si atom and additional O-H bond in neighboring Si atom. (c) HF reacts with surface containing one Si-F bond and one O-H bond forming additional Si-F bond in neighboring Si atom and producing H ₂ O where -Si* represents reaction site. | 30 |
| Figure 3.4. Schematic of reaction between silicon dioxide cluster and hydrogen fluoride gas..... | 31 |
| Figure 3.5. Schematic of reaction between silicon dioxide cluster with triple Si-F bond and hydrogen fluoride gas. | 32 |
| Figure 3.6. Schematic of reaction between silicon dioxide surface with single Si-F bond and hydrogen fluoride gas. | 33 |

| | |
|--|----|
| Figure 3.7. Schematic of reaction between silicon dioxide surface with single Si-F bond and hydrogen fluoride gas. | 34 |
| Figure 3.8. Images of etching process simulation with incident energy of 40 eV at (a) $t = 0$, (b) $t = 100$ ps, and (c) $t = 300$ ps. Insets of (b) show images of Si-F bond formation at $t = 1.075$ ps, O-H bond formation at $t = 6.075$ ps, and SiF_4 formation at $t = 39.425$ ps. | 35 |
| Figure 3.9. Final images of each etching simulation with different incident energies: (a) 20 eV, (b) 30 eV, (c) 40 eV, and (d) 80 eV. | 36 |
| Figure 3.10. Temporal variations of silicon dioxide etching configurations with HF, 20eV incident energy. (a. $t=100\text{ps}$, b. $t=200\text{ps}$, c. $t=300\text{ps}$)..... | 37 |
| Figure 3.11. Temporal variations of silicon dioxide etching configurations with HF, 40eV incident energy. (a. $t=100\text{ps}$, b. $t=200\text{ps}$, c. $t=300\text{ps}$)..... | 38 |
| Figure 3.12. Temporal variations of silicon dioxide etching configurations with HF, 80eV incident energy. (a. $t=100\text{ps}$, b. $t=200\text{ps}$, c. $t=300\text{ps}$)..... | 39 |
| Figure 3.13. (a) Dissociation fraction and (b) etching initiation time with respect to incident energy of HF molecule. | 40 |
| Figure 3.14. (a) Numbers of generated SiF_x , (b) H_2O , and (c) byproduct molecules with respect to time for four incident energies. | 41 |
| Figure 3.15. Radial distribution functions between Si and F for the four cases with different incident energies. | 42 |
| Figure 3.16. Radial distribution functions between Si and F for the three cases with different system temperature. | 43 |
| Figure 3.17. Etching yield of SiO_2 by HF molecule as a function of ion incident energy. | 44 |

| | |
|---|----|
| Figure 4.1.1. (a) Schematic expression of modulating binder, (b) formation of intramolecular bond between chitosan and XNBR (c) Characterization of chitosan, chitosan-XNBR, and XNBR by FT-IR, (d) XPS C1s core-level spectra and (e) N1s core-level spectra of chitosan-XNBR. | 66 |
| Figure 4.1.2. Solubility test in acetic acid of prepared polymer films..... | 67 |
| Figure 4.1.3. DFT modeling for chitosan and XNBR molecules. | 68 |
| Figure 4.1.4. DFT modeling for chitosan and XNBR molecules adsorbed with Li ₂ S ₆ molecules. | 69 |
| Figure 4.1.5. (a) computational calculation of polymer-LPS(Li ₂ S ₆) binding energy using density-functional theory, (b) UV–Vis spectra of Li ₂ S ₆ and various polymer films according to ratio of chitosan and XNBR (right; optical images), (c) Average reduced moduli and elastic recovery parameter of electrode with prepared various binders determined <i>via</i> nanoindentation, and (d) Evaluation chart of prepared binders for Li-S battery | 70 |
| Figure 4.1.6. Computational calculation of polymer-LPS(Li ₂ S ₆) binding energy using density-functional theory. | 71 |
| Figure 4.1.7. Ionic conductivity of prepared polymer films at 25 °C from EIS (electrochemical impedance spectroscopy)..... | 72 |
| Figure 4.1.8. (a) discharging specific capacities of the Li–S cells at a rate of 0.2 C, (b) cyclic voltammetry of Li-S cell with various amount of X1C3 binder, (c) discharging specific capacities of the Li–S cells according to the contents of X1C3 binder at a rate of 0.2 C, (d) cyclic voltammetry of Li-S cell with 3 wt.% X1C3 binder at 0.1-0.5 mV s ⁻¹ , (e) Linear relationship of redox peak current from Figure 3(d), and (f) rate capability test of the Li–S cell with 3 wt.% X1C3 binder at 0.05, 0.2, 1, 2, 5, 10, 15, and 20 C. | 73 |

| | |
|--|----|
| Figure 4.1.9. The voltage difference between the charge and discharge plateau of prepared Li-S cells. | 74 |
| Figure 4.2.1. (a) Schematic expression of the multifunctional Ga ₂ O ₃ shield in LSBs, (b) TEM images of the as-prepared Ga ₂ O ₃ , (c) XRD pattern of the as-prepared Ga ₂ O ₃ , and (d) XPS spectra of the as-prepared Ga ₂ O ₃ | 85 |
| Figure 4.2.2. XPS spectra of pristine Ga ₂ O ₃ at O 1s core level..... | 86 |
| Figure 4.2.3. Computational calculation of interaction between various metal oxides (Ga ₂ O ₃ , Al ₂ O ₃ , Ti ₄ O ₇ , Fe ₃ O ₄ , MoO ₃ (010), MoO ₃ (001), and V ₂ O ₅)..... | 87 |
| Figure 4.2.4. (a) DFT calculation results of the interaction between Ga ₂ O ₃ , Al ₂ O ₃ , and LPS, (b) UV–Vis spectra of Ga ₂ O ₃ in LPS solution for 6 h and optical image (inset), (c) XPS spectra of Ga ₂ O ₃ after adsorption in LPS solution, and (e) Schematic expression of the oxidation of the initially formed polysulfides by Ga ₂ O ₃ to form thiosulfate on the surface..... | 88 |
| Figure 4.2.5. Computational calculation of interaction between Ga ₂ O ₃ and Li ₂ S _n (n=4, 6, and 8) | 89 |
| Figure 4.2.6. (a) Ionic conductivity with various contents of Ga ₂ O ₃ evaluated by EIS, (b) SEM images of Ga ₂ O ₃ shield (surface, scale bar; 500 nm), (c) Voltage profiles of lithium symmetric cells with Celgard 2500 (PP) and Ga ₂ O ₃ shield as separators at a current density of 2 mA cm ⁻² (4 mAh cm ⁻²), (d) optical images of the PP separator and the as-prepared Ga ₂ O ₃ shield after heating at 150 °C for 1 h, and (e) optical image of the diffusion of LPS: H-type cell with the as-prepared Ga ₂ O ₃ shield after 48 h. | 90 |
| Figure 4.2.7. SEM images of prepared G60 interlayer (a), (c) and G90 interlayer (b), (d) (surface, scale bar; 500 nm and 50 nm). | 91 |

| | |
|---|----|
| Figure 4.2.8. SEM images of Li-metal surface after Li symmetric cell test; (a) Li metal with Celgard 2500 (PP membrane), (b) Li-metal with G60 interlayer, and (c) magnification of (b)..... | 92 |
| Figure 4.2.9. (a) Discharging specific capacities of the as-prepared Li–S cells at a rate of 0.2 C, (b) Galvanostatic charge–discharge profiles of the Li–S cells without interlayer, and with the G60 interlayer at the initial cycle (0.2 C) (c) CV profiles of the Li–S cells with the G60 interlayer according to various scan rates, (d) Rate capability test of the Li–S cells without interlayer and with the G60 interlayer at 0.2 to 8 C, and (e) Long-term cycling of the as-prepared Li–S cells with the G60 interlayer at 2 C for 4,000 cycles. | 93 |
| Figure 4.2.10. Galvanostatic charge-discharge profiles of prepared LSBs at the initial cycle of 0.2C. | 94 |
| Figure 4.2.11. Voltage difference of prepared LSBs obtained from galvanostatic charge-discharge profiles and its results..... | 95 |
| Figure 4.2.12. Cyclic voltammetry of prepared Li-S cell without interlayer (PE separator) according to various scan rates..... | 96 |
| Figure 4.2.13. (a) The relationships between current density of redox peaks and square root of scan rate about prepared Li-S cells (without interlayer and with G60 interlayer) and (b) its detailed slope values..... | 97 |
| Figure 4.2.14. Periodic table of reported metal-oxide-based interlayer for LSBs, and their battery performance (cycle life of LSBs and capacity decay retention per cycle) | 98 |
| Figure 4.2.15. Electrochemical impedance spectroscopic data of the Li–S cell before and after 4000 cycles. (a) Nyquist plot and (b) detailed data of Fig. S11a. SEM image of prepared G60 interlayer after 4000 cycles (surface, scale bar; 100 | |

nm).99

List of Tables

| | |
|---|-----|
| Table 3.1. Fitted parameters in developing Si-O-H-F force field..... | 45 |
| Table 3.2. Corrections to the ReaxFF parameter optimization ranges..... | 46 |
| Table 3.3. Optimized ReaxFF parameters for Si/O/H/F..... | 47 |
| Table 4.2.1. Reported LSB performance with metal-oxide interlayer system.. | 100 |

Chapter 1. Introduction

1.1. Overall Introduction

Computational chemistry (or computational nano-science) is a technique which designs and optimizes materials in nano scale, processes, and nano systems with computational simulations and information technology. Due to the sharp progress of computing power, simulations with more atoms or large systems with higher accuracy is possible. There are numerous computational methods for investigation of chemical system. The simulation techniques are classified according to its scale of system as shown in Figure 1.1. The length and time scale of interests in this dissertation range from the quantum mechanical (QM) to the microscopic level, using multi-scale simulation methods to simulate complicated chemical etching processes of silicon dioxide substrate with hydrogen fluoride gas systems and adsorption energy calculations in Li-S batteries.

1.2. Outline

In Chapter 2, theoretical background for computational chemistry is briefly described. As multi-scale simulation that conducted in this thesis is from

QM method to molecular dynamics (MD) scale, fundamental theory on density functional theory (DFT) and the ReaxFF reactive force field method is provided. In Chapter 3, the procedure of constructing the ReaxFF reactive force field from QM calculation results to simulate etching processes of silicon dioxide with hydrogen fluoride gas and its results are described. Lastly, in Chapter 4, adsorption energy calculations of components in Li-S batteries with lithium polysulfides (LPS) to suggest functional binder and functional separator coating metal oxides with enhanced durability, electronic/ionic conductivity, and thus increasing energy density of battery is described. Finally, in Chapter 5. the significance and applicability of this thesis is described as final remark.

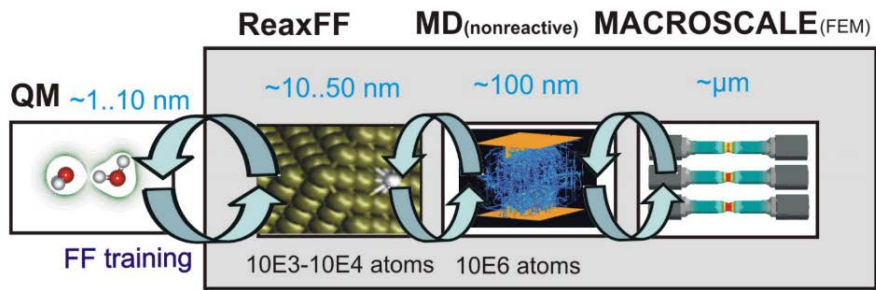


Figure 1.1. Various computational methods according to the scale of simulation.

Chapter 2.

Theoretical Background for Computational Chemistry

2.1. DFT calculations

2.1.1 Introduction

Density functional theory (DFT) which is based on two Hohenberg-Kohn theorems method is one of the computational modelling technique that is widely used in the fields of condensed matter physics, chemistry, and materials science to study the fundamental structures such as electronic and nuclear structure of many-particle systems. Hohenberg-Kohn theorem states that the ground state properties of an atom or molecule, by determining its electron density function, and that the trial electron density must present equal or more energy to the actual energy. The energy of a system is formulated as a deviation from the energy of an idealized system with non-interacting electrons in the Kohn-Sham approach. From the energy equation, the Kohn-Sham equations can be derived by minimizing the energy with respect to the Kohn-Sham orbital which is similar to the Hartree-Fock equations. Finding a good functionals is an important issue in DFT calculations.

The only unknown function in DFT calculation is the exchange correlated energy (or exchange-correlation energy), which is a minor part compared to the total energy. Even a relatively simple approximation of the exchange correlation energy can provide accuracy to the computational model. The simplest is the local density approximation (LDA), which assumes that the electron density changes slowly and that the exchange correlation energy can be calculated using a uniform electron density equation. This is achieved by making the exchange correlation functional more accurate by also relying on the first derivative of the density. Further improvements can be made with adding a quadratic derivative and mixing the Hartree-Fock exchange with the functional. DFT and Hartree-Fock theory are conceptually and computationally very similar, but DFT gives far superior results. As a result, it became a very popular method in condensed matter physics, computational chemistry, and computational physics.

2.1.2 Kohn-Sham method

Kohn and Sham suggested that the orbitals can be introduced for the basis for the use of the DFT method in computational chemistry since it is inadequate to represent the kinetic energy with the orbital-free model. Kohn-Sham equation divide the kinetic energy functional into two separate parts, one that can be exactly calculated and the other minor correction term. When the orbit is reintroduced, the complexity increases from the $3N$ variable to the $3N$ variable, and its electron correlation reappears as a separate term. The Kohn-Sham model and

the Hartree-Fock method are closely related and shares the same equations for kinetic energy, Coulomb electron-electron energy, and electron nuclear energy.

The main contribution of which is equivalent to the kinetic energy of Hartree-Fock kinetic energy, with the division of the electron kinetic energy into two parts that can be justified as follows. Assume the moment of the Hamiltonian operator in the form of eq. (2.1) with $0 \leq \lambda \leq 1$.

$$\mathbf{H}_\lambda = \mathbf{T} + \mathbf{V}_{\text{ext}}(\lambda) + \lambda \mathbf{V}_{\text{ee}} \quad (2.1)$$

The external potential operator \mathbf{V}_{ext} is equal to \mathbf{V}_{ne} for $\lambda = 1$. For intermediate λ values, $\mathbf{V}_{\text{ext}}(\lambda)$ is expected to be adjusted such that the same density is obtained for $\lambda = 1$ (actual system), for $\lambda = 0$, (virtual system with non-interacting electrons) and for all intermediate λ values. In the case of $\lambda = 0$, the electrons do not interact. The exact solution of the Schrodinger equation is given as a Slater determinant consisting of molecular orbitals ϕ_i , and the exact kinetic energy functional is given by the eq. (2.2).

$$T_s = \sum_{i=1}^{N_{\text{elec}}} \left\langle \phi_i \left| -\frac{1}{2} \nabla^2 \right| \phi_i \right\rangle \quad (2.2)$$

Where the subscript S denotes that it is the kinetic energy calculated from a Slater determinant. The $\lambda = 1$ case corresponds to interacting electrons, and eq. (2.2) is the only an approximation to the real kinetic energy, but a substantial improvement over the Thomas-Fermi theory.

Another way to justify the use of eq. (2.2) in the calculation of kinetic energy refers to the natural orbital. From the natural orbital resulting from the exact density matrix, the exact kinetic energy can be evaluated.

$$\begin{aligned}
T[\rho_{exact}] &= \sum_{i=1}^{\infty} n_i \left\langle \phi_i^{NO} \left| -\frac{1}{2} \nabla^2 \right| \phi_i^{NO} \right\rangle \\
\rho_{exact} &= \sum_{i=1}^{\infty} n_i |\phi_i^{NO}|^2 \\
N_{elec} &= \sum_{i=1}^{\infty} n_i
\end{aligned} \tag{2.3}$$

The orbital occupancy number n_i (eigenvalues of density matrix) is between 0 and 1, depending on the number of electrons in the spin orbit. An infinite number of natural orbitals are required to represent an accurate density. N_{elec} occupancy is close to 1 at first and near 0 for the rest. In terms of auxiliary one-electron functions or orbitals can be written as eq. (2.4) since the exact density matrix is unknown.

$$\rho_{approx} = \sum_{i=1}^{N_{elec}} |\phi_i|^2 \tag{2.4}$$

This corresponds to the eq. (2.3) When the occupied number is exactly 0 or 1. This missing kinetic energy from eq. (2.2), can be considered as kinetic correlation energy, is because the occupation number is not exactly 0 or 1.

The key to Kohn-Sham theory is to calculate the kinetic energy from equation eq under the assumption of non-interacting electrons. (2.2). In the real system, electrons interact, eq. (2.2) neither provides nor represents total kinetic energy. However, the calculated difference between accurate kinetic energy and kinetic energy assuming non-interacting orbitals is negligible, similar to the Hartree-Fock theory, which provides over 99 percent consistency. The remaining kinetic energy is absorbed by the exchange correlation term, and the general DFT energy equation can be written as in eq. (2.5).

$$E_{DFT}[\rho] = T_S[\rho] + E_{ne}[\rho] + J[\rho] + E_{xc}[\rho] \tag{2.5}$$

By making the E_{DFT} equivalent to the exact energy, this equation defines the E_{xc} , the remaining part after the elimination of the non-interacting kinetic energy, and the potential energy terms of E_{ne} and J .

$$E_{xc}[\rho] = (T[\rho] - T_s[\rho]) + (E_{ee}[\rho] - J[\rho]) \quad (2.6)$$

Each part of the eq. (2.6) is considered as the kinetic correlation energy and the other one as the potential correlation and exchange energy.

While the task of developing orbital-free models is to derive approximations for motion, exchange, and correlated energy functionals, the Kohn-Sham theory has the corresponding task of deriving approximations for exchange-correlated energy functionals. Since the exchange-correlated energy is about one-tenth of kinetic energy, the Kohn-Sham theory is less sensitive to functional inaccuracy than the orbital-free theory. The orbital-free theory is a true density functional theory (including three variables), while the Kohn-Sham method is an independent particle model (including $3N$ variables) similar to the Hartree-Fock theory, but still less complicated than many-body correlation wave function models.

2.2. The ReaxFF reactive force field

2.2.1 Introduction

Atomic-scale simulation techniques are powerful tools for investigating, developing, and optimizing the properties of materials. Simulation techniques based on quantum mechanics (QM) have grown in popularity in recent decades, allowing widespread access to quantum-level computation through the development of software packages and improvements in computational power. With such availability, computational simulations have provided a theoretical guidance and worked as good screening tools. However, in quantum-level calculations, the computational cost severely limits the scale of the simulation. This limitation often precludes QM methods from taking into account the dynamic evolution of systems, hampering theoretical understanding of key factors influencing the overall behavior of materials. To reduce this deficiencies, attempts have been made to build empirical force fields using QM structure and energy data as train sets. Simulations using empirical force fields better describe the dynamic process because empirical force fields require significantly lower computational costs compared to QM calculations. Such empirical methods, including reaction fields (ReaxFF), trade accuracy with lower computational resources, allow us to reach simulation scales above the QM level and close to the molecular dynamics (MD) level.

Empirical force field methods use empirically determined intermolecular force fields or potentials to calculate the energy of a system as a whole with a function of atomic positions. It is suitable for non-reactive interactions, such as angular transformations represented by classical approximate harmonic potentials, dispersion represented by van der Waals potentials, and Coulomb interactions represented by various polarization schemes. However, these techniques are unable to model the changes in atomic linkages required to model newly formed chemical

reactions because atomic bonds are broken. ReaxFF represents a reaction in the form of an atomic potential bond order. The bond order is calculated empirically based on the distance between atoms. For the electronic interactions driving chemical bonds, the method is implicitly handled so that chemical reactions can be modeled without considering explicit QMs.

The classical treatment of reactive chemistry made available by the ReaxFF has enabled many studies to be conducted on a scale that was previously beyond the scope of computational methods. With ReaxFF, the processing of each element of ReaxFF is a transmissible reaction that occurs between the phases, giving you access to simulations that include reactive events at the interface between the solid, liquid, and gas phases. Such transferability, along with lower computational costs compared to QM, is not only the reactivity of the species in which ReaxFF is involved, but also the dynamics such as diffusion coefficient and solubility that affect how the species move through the system. This allows ReaxFF to model complex processes involving multiple phases that are in contact with each other.

2.2.2 The ReaxFF reactive force field method

While QM methods are applicable to all the chemical systems, it involves expensive computational cost thus hinder its capability. However, ReaxFF allows us to model large systems with lower computational cost while retaining the computational accuracy compared to QM method. ReaxFF avoids explicit bonds in favor of bond orders, allowing continuous bond formation/breaking, whereas

traditional force field are unable to describe chemical reactions because of the requirement of breaking and forming bonds. ReaxFF has been parametrized and tested for various kinds of systems containing reactions for hydrocarbon, li-ion battery components, and transition-metal-catalyzed nanotube formation. ReaxFF force field parameters are developed by fitting against experimental and QM calculations.

The forces are derived from a general energy expression in the ReaxFF method.

$$E_{system} = E_{bond} + E_{over} + E_{under} + E_{lp} + E_{val} + E_{vdWaals} + E_{coulomb} \quad (2.7)$$

The E_{system} includes bond energy (E_{bond}), energy term that contributes to penalize over-coordination (E_{over}) and stabilizes under-coordination of atoms (E_{under}), lone-pair energy (E_{lp}), valence angle energy (E_{val}), and terms to describe non-bonded Coulomb ($E_{coulomb}$), and van der Waals ($E_{vdWaals}$) interaction energies. Except non-bonded Coulomb and van der Waals interaction, all energy terms include dependencies on bond-order and the local environment of each atom. By general relationship between bond order and interatomic distance, bond order in ReaxFF is described. Bond order equation contains a set of parameters that are tuned primarily to fit the volumetric energy relationships (equation of state or EOS) of 4, 6, and 8-coordinated crystals. Then the bond order is calculated directly from the instantaneous interatomic distance that is continuously updated during the simulation. A sharp-dependent charge distribution determined with the Electronegativity Equalization Method (EEM) is used for calculating the Coulomb energy of the system. In this method, the individual atomic charges change with dynamics. This allows ReaxFF to model charge transfer in chemical reactions.

All other non-bonded interactions (short-range Pauli repulsion and long-range variance) are included in the Van der Waals term ($E_{coulomb}$). Non-bond order dependent terms ($E_{coulomb}$ and $E_{vdWaals}$) are screened by the taper function and shielded to avoid excessive repulsion over short distances. The Si-O-H-F force field presented in this thesis has almost the same Si/O/H parameters as the recently published description of ReaxFF in Kapton/POSS, and these force field parameters can be integrated as the parameters are transferable in general. Containing all elements of interest and all combinations of the bond/angle/dihedral parameters is necessary to utilize ReaxFF parameters.

2.2.3 Energy descriptions in ReaxFF

Bond order and Bond Energy (E_{bond})

In the ReaxFF method, the bond order is obtained from interatomic distance as described in eq. (2.8).

$$BO'_{ij} = \exp \left[p_{bo,1} \left(\frac{r_{ij}}{r_0} \right)^{p_{bo,2}} \right] + \exp \left[p_{bo,3} \left(\frac{r_{ij}^\pi}{r_0} \right)^{p_{bo,4}} \right] + \exp \left[p_{bo,5} \left(\frac{r_{ij}^{\pi\pi}}{r_0} \right)^{p_{bo,6}} \right] \quad (2.8)$$

$P_{bo,i}$ ($i=1$ to 6) are force field parameters and are optimized against experimental and QM data. Eq. (2.8) consists of three exponential terms. The first term is for the sigma bond within rather short distances, the second term corresponds to first pi bond within middle range distances and third term refers to second pi bond within

rather long distances. From this uncorrected bond order, uncorrected over-coordination is calculated for each atom which is further used in calculating the corrected bond order, BO_{ij} . The corrected bond orders are used for calculating bond energy given in eq. (2.9)

$$E_{bond} = -D_e^{-\sigma} \cdot BO_{ij}^{\sigma} \cdot \exp \left[p_{be,1} \left(1 - (BO_{ij}^{\sigma})^{p_{be,2}} \right) - D_e^{\pi} BO_{ij}^{\pi} - D_e^{\pi\pi} BO_{ij}^{\pi\pi} \right] \quad (2.9)$$

where, $p_{be,1}$, $p_{be,2}$, D_e^{π} , $D_e^{\pi\pi}$ are force field parameters.

Valence Angle Energy (E_{val})

Bond order dependent form is used for calculating energy associated with deviations in valence angle. The deviations in valence angle Θ_{ikj} from its equilibrium value Θ_0 is used as described in eq. (2.11). The equilibrium angle Θ_0 for Θ_{ikj} depends on the sum of pi bond orders around the central atom j.

$$E_{val} = f_7(BO_{ij}) \times f_7(BO_{kj}) \times f_8(\Delta_j) \times \{ p_{val1} - p_{val1} \exp[-p_{val2} (\Theta_0(BO) - \Theta_{ijk})^2] \} \quad (2.11)$$

where p_{val1} and p_{val2} are force field parameters.

Torsion Angle Energy (E_{tor})

Torsion angle energy term is dependent on bond order just as with bond and angle energy terms. The torsion angle energy term is described as eq. (2.12).

$$E_{tor} = f_{10}(BO_{ij}, BO_{jk}, BO_{kl}) \times \sin \Theta_{ijk} \times \left[\frac{1}{2} V_1 (1 + \cos \omega_{ikjl}) + \frac{1}{2} V_2 \times \exp \{ p_{tor1} (BO_{jk}^{\pi} - 1 + f_{11}(\Delta_j, \Delta_k))^2 \} (1 - \cos 2\omega_{ijk}) + \frac{1}{2} V_3 (1 + \cos 3\omega_{ijk}) \right] \quad (2.12)$$

Lone Pair Energy (E_{lp})

Lone pair is the difference between the total number of electrons in outer shell of an atom and the sum of bond orders around the range of atomic center. The lone pair energy penalty is described in eq. (2.10).

$$E_{lp} = \frac{p_{lp2} \Delta_i^{lp}}{1 + \exp(-75 \times \Delta_i^{lp})} \quad (2.10)$$

where Δ_i^{lp} is the number of lone pairs and p_{lp2} is the force field parameter.

Non-bonded Van der Waals Interaction Energy ($E_{vdWaals}$)

Non-bonded van der Waals interactions are included in describing the long range interactions as a formation of distance-corrected Morse potential as given in eq. (2.13). Additionally, excessively high repulsions between bonded atoms and atoms that sharing a valence angle are prevented with inclusion of the shielded interaction.

$$E_{vdWaals} = Tap \times D_{ij} \times \left\{ \exp \left[\alpha_{ij} \left(1 - \frac{f_{13}(r_{ij})}{r_{vdw}} \right) \right] - 2 \times \exp \left[\frac{1}{2} \alpha_{ij} \left(1 - \frac{f_{13}(r_{ij})}{r_{vdw}} \right) \right] \right\} \quad (2.13)$$

where Tap is a taper term which eschews discontinuities when charged species move in and out of the non-bonded cutoff radius.

$$f_{13}(r_{ij}) = \left[r_{ij}^{p_{vdw}} + \left(\frac{1}{\gamma_w} \right)^{p_{vdw}} \right]^{\frac{1}{p_{vdw1}}} \quad (2.14)$$

Non-bonded Coulomb Interaction Energy ($E_{coulomb}$)

As with the van der Waals interactions, Coulomb interactions between all atom pairs are calculated. The orbital overlap at near atomic distance is adjusted with the use of a shielded Coulomb potential. The electron equilibrium method (EEM) is used for the calculation of atomic charges.

$$E_{coulomb} = Tap \cdot C \cdot \frac{q_i q_j}{\left[r_{ij}^3 + \left(\frac{1}{r_{ij}} \right)^3 \right]^{1/3}} \quad (2.15)$$

Chapter 3.

Molecular Dynamics Simulation of Silicon

Dioxide Etching by Hydrogen Fluoride Using

ReaxFF Reactive Force Field

Reproduced in part with permission from Dong Hyun Kim, Seung Jae Kwak, Jae Hun Jeong, Suyoung Yoo, Sang Ki Nam, YongJoo Kim, and Won Bo Lee. Molecular dynamics simulation of silicon dioxide etching by hydrogen fluoride using the reactive force field. ACS Omega, 2021. Copyright 2021 American Chemical Society.

3.1. Introduction

Owing to the continuous improvement in the performance of electronic devices, it has become more important to understand plasma–surface interactions at the atomic scale in semiconductor processing. Dry etching processes have been developed and widely used to achieve both high aspect ratios and selectivity in the etching process. In dry etching techniques using remote plasma sources, defects

and structure quality degradation can be avoided. ⁽¹⁾ Fluorine-based etching gases such as SF₆, CF₄, and SiF₄ are typically used in plasma processing for etching because F atoms are the most reactive among all halogens on Si and produce volatile products such as SiF₄ after reacting with Si atoms. ⁽²⁻⁶⁾

For plasma–surface interactions, computational studies have been widely performed to analyze the mechanisms of various plasma processes, such as etching and deposition. Hoshino *et al.* ⁽⁷⁾ theoretically suggested the etching reaction mechanism of SiO₂ caused by HF molecules using *ab initio* quantum chemical calculations. Kang *et al.* ⁽⁸⁾ conducted a detailed quantum chemical investigation on the chemical etching mechanism of SiO₂ with HF and H₂O etchants. Several studies based on using molecular dynamics (MD) simulations have been performed to analyze etching processes involving a system comprising Si and SiO₂ with halogen/fluorine etchant gases. Abrams *et al.* ⁽⁹⁾ presented a new empirical interatomic potential for Si/C/F systems to simulate their etching reactions with Si and CF₃⁺. Barone *et al.* ⁽¹⁰⁾ reported MD simulation results of energetic F⁺ and Cl⁺ impacting Si surfaces at normal incidence. Ohta *et al.* ⁽¹¹⁾ performed MD simulations for Si and SiO₂ etching using energetic halogens (F, Cl) with sets of interatomic potentials. Iwakawa *et al.* ⁽¹²⁾ conducted Si etching using Cl-based plasmas, including both high-energy Cl⁺ ions and low-energy neutral Cl radicals, using MD simulations. Brichon *et al.* ⁽¹³⁾ performed MD simulations of low-energy Cl⁺ and Cl₂⁺ bombardment on Si(100) surfaces to investigate the effect of plasma dissociation on Si etch applications. Miyake *et al.* ⁽¹⁴⁾ investigated the mechanisms of SiN and SiO₂ etching by fluorocarbon or hydrofluorocarbon plasmas using MD simulations. Nakazaki *et al.* ⁽¹⁵⁾ performed MD simulations for Cl⁺ and Br⁺ ions incident on Si(100) surfaces with Cl and Br neutrals, respectively, to obtain a better

understanding of surface reaction kinetics during Si etching. Numezawa *et al.*⁽¹⁶⁾ investigated the adsorption mechanisms of F radicals on Si, SiO₂, and Si₃N₄ surfaces during the reactive ion etching using MD simulations and an extended Langmuir model.

Although significant studies based on MD simulations have been reported, it is necessary to study the dynamics of the formation and breaking of bonds to further understand the dynamics of surface etching reactions during dry etching. Hence, the reactive force field (ReaxFF), which allows the formation and breaking of bonds in chemical reactions, should be used as a force field in MD simulations.⁽¹⁷⁾ The ReaxFF method combines a bond order/bond distance relationship with a polarizable charge description using the electronegativity equalization method (EEM)⁽¹⁸⁾ and bond-order-dependent three- and four-body interactions. Owing to the combination of bond/non-bond order terms, ReaxFF is applicable to a wide range of materials, including covalent,^(19, 20) metallic^(21, 22), and multicomponent metal hydride/oxide/carbide systems.^(23, 24, 25) When optimizing the ReaxFF parameters, substantial quantum mechanical (QM) training sets that contain energies of corresponding structures and reactions are used. As parameters are trained against QM data, MD simulations using the ReaxFF guarantee the accuracy of density functional theory (DFT) calculations with a larger simulation system size and lower computational cost compared with DFT calculations.

In this study, we conducted MD simulations of SiO₂ substrates using active HF molecules. First, we optimized the ReaxFF parameters of the Si/O/H/F system against QM training sets using DFT calculations. Next, we conducted MD simulations of the etching process of an α -cristobalite SiO₂ substrate using HF molecules and our optimized ReaxFF parameters. Finally, simulation results with

different incident energies of the HF molecules were analyzed for a systematic study of the system. In the current study, we optimized the force-field parameters for SiO₂-hydrogen fluoride systems.

3.2. Simulation model and details

The system of interest includes etching of the SiO₂ layer using high-energy HF gas. Therefore, ReaxFF should capture chemical reactions between Si/O/H/F atoms for the etching simulation, where F ions participate in reactions as anions in the etching process. Previously, the ReaxFF, which included Si/O/H/F atoms, was developed to simulate Kapton polyimide, polyhedral oligomeric silsesquioxane (POSS), silica, and Teflon to investigate the surface chemistry of these materials when exposed to oxygen.⁽²⁶⁾ However, to utilize the previously developed ReaxFF, the parameters for Si/O/F must be modified to capture the etching of SiO₂ and the formation of SiF_x. Based on previously developed ReaxFF parameters for Si/O/H/F atoms, we re-optimized parameters for Si/O/F and bond parameters for Si-F and H-F, and the valence angle parameters for F-Si-F and F-Si-O against QM resulted in the training sets, which included the structures and energies of reactions using the covariance matrix adaptation evolution strategy (CMA-ES) technique.^(27, 28) Each CMA-ES step was iteratively conducted to improve a multivariate normal distribution in the parameter space to identify a distribution that minimizes the objective function or cost function. Without refitting

general parameters for ReaxFF, total 76 parameters were fitted to training sets. (Table 3-1) In addition, we updated some of the intervals to exclude (combinations) of EEM related parameters that are known to cause unrealistic results. EEM hardness parameter η_i (Atom parameter index 15), and the corresponding short-range screening parameter for the electrostatic interaction γ_i , (Atom parameter index 6) must satisfy the following inequality.

$$\eta_i > \frac{\gamma_i}{8\pi\epsilon_0} \quad (1)$$

New ranges for listed EEM parameters are listed in Table 3-2.

The box for the MD simulation was set to 2.1 nm \times 1.1 nm \times 6.5 nm, which included an α -cristobalite SiO₂ substrate measuring 2.1 nm \times 1.1 nm \times 2.4 nm. The initial geometry of the SiO₂ substrate was optimized using a limited Broyden–Fletcher–Goldfarb–Shanno minimization method and a convergence criterion of 1.0 (kcal/mol)/Å, followed by a relaxation process with an NVT ensemble for 100 ps with a timestep of 0.25 fs. After the SiO₂ substrate was relaxed, the SiO₂ etching process was performed for 300 ps, which is enough time to investigate various etching properties in our simulation. For the etching process, incident HF molecules were added to the system with incident energies of 20, 30, 40, and 80 eV. Each HF molecule was added from the top surface of the simulation box with randomly selected x- and y-coordinates every 250 fs, and 200 molecules were inserted over 50 ps. In each insertion step, the initial velocity of the inserted HF molecule contained only the z-direction component with the associated incident energy to simplify the zero-incident-angle system. After 200 HF molecules were inserted, additional simulations were conducted for 50 ps without further insertion of the HF molecule. Subsequently, gas molecules produced such as H₂, H₂O, O₂,

and SiF_x were removed to simulate the purge process. This entire simulation procedure was repeated three times, resulting in a total simulation time of 300 ps. All MD simulations with an optimized ReaxFF were conducted at $T = 308.15$ K using a Berendsen thermostat with a damping constant of 100 fs.

3.3. Results

Figure 3.1 shows a comparison of the energies of the SiF_4 and SiO_2 clusters ($\text{Si}_4\text{O}_{10}\text{H}_4$ containing two or three Si–F bonds) with respect to the bond length and valence angle using DFT and our optimized ReaxFF. DFT calculations were conducted using the Amsterdam density functional program ^(29, 30) with a generalized gradient approximation in the Perdew–Burke–Ernzerhof Grimme DFT-D3 dispersion exchange-correction functional form and triple zeta with two polarization function basis sets for all atoms. In Figures 3.1-(a) and (b), the energy differences from the equilibrium using DFT and the ReaxFF between Si and F in SiF_4 are shown as functions of Si–F distance and valence angle, respectively. The bond distance between Si and F changed from 1.3 to 2.3 Å, and the valence angle of F–Si–F changed from 89.5° to 129.5°. Energy differences using DFT and the ReaxFF near the equilibrated bond lengths of SiO_2 clusters containing SiF_2 and SiF_3 are shown in Figures 3.1-(c) and (d), respectively. In general, the energy difference plots using the ReaxFF showed good agreement with the results from DFT calculations.

In optimizing the ReaxFF parameters, reaction paths including transition states and their associated energies (enthalpy changes and activation energies of reactions using DFT) that produce Si–F bonds or SiF_x gases were included in the training sets. The main reaction between SiO₂ and HF molecules that produce SiF₄ gas is as follows:



To simulate the etching mechanism, we assumed that four Si–F bonds were subsequently formed to produce SiF₄ from the previously suggested subsequent reaction mechanism of SiO₂ etching.^(7,8) Using the previously explained SiO₂ cluster model (Si₄O₁₀H₄ containing a number of Si–F bonds), we calculated the enthalpy changes and activation energies of four subsequent reactions forming SiF₄, and the molecular illustration of each state (initial, transition, and final state in each reaction) is presented in Figure 3.2. The transition state location and activation energy for each reaction were calculated using both the nudged elastic band (NEB) method and dimer method.^(31, 32) Using the NEB method, one can easily determine the intermediate states of the reaction because the NEB method conducts energy calculations in many molecular images. The transition state search process is as follows: First, 30 iterations of geometry relaxation were conducted using the generated images from linear interpolation. Next, the saddle point was searched using the climbing image NEB method.⁽³³⁾ When the energy diverged, we converged the force in the image of the latest step using the dimer method. To implement the NEB and dimer methods, the Vienna Ab-initio Software Package was used^(34, 35, 36, 37) with the projector augmented wave pseudopotential and the exchange-correlation function described by Perdew–Burke–Ernzerhof functional.

The plane wave energy cutoff was set to 400 eV. The structures were fully relaxed until the energy difference in the self-consistent field cycle was lower than 10^{-7} eV and maximum force acting on each atom was lower than 0.02 eV/Å in ionic steps.

For further optimization, we calculated the enthalpy change and activation energy of the additional reactions using the SiO₂ slab model shown in Figure 3.3. Additional reactions occurred are in the relatively early stage of the etching process, where HF reacted with a slab containing either no or one Si–F bond. For the reaction of HF with a SiO₂ slab containing one Si–F bond, two different paths are possible depending on the location of the additional Si–F bond from the reaction. For the reaction where an additional Si–F bond is formed at the same Si atom containing the Si–F bond, additional O–H bonds are formed at neighboring Si atoms, as shown in Figure 3.3-(b). Meanwhile, when an additional Si–F bond is formed at the neighboring Si atom, H₂O is produced, as shown in Figure 3.3-(c). Despite the mismatches of enthalpy change and activation energy in some reactions, both the ReaxFF and DFT results demonstrated consistency in general. Detailed schematics of reactions are shown in Figure 3.4, Figure 3.5, Figure 3.6, and Figure 3.7. Figure 3.8 shows images of the etching process simulation with an incident energy of 40 eV at $t = 0, 100,$ and 300 ps. At $t = 0$ in Figure 3.8-(a), the stable structure of the SiO₂ film is clearly depicted. However, incident HF molecules collided with the SiO₂ surface, and the H–F bond of the HF molecule dissociated and created a new Si–F bond at the SiO₂ surface, as shown in the inset of Figure 3.8-(b) at $t = 1.075$ ps. The O–H bond was created with a left H atom near the previously formed Si–F bond (inset of Figure 3.8-(b) at $t = 6.075$ ps), as suggested in the NEB calculation results. When a sufficient number of Si–F bonds were created in a single Si atom, SiF₄ was formed, as shown in the inset of Figure 3.8-

(b) at $t = 39.425$ ps, after the dangling Si–O bond was dissociated when an additional O–H bond was formed or the incident HF molecule collided with the dangling Si–O bond. At $t = 100$ ps, the produced gas molecules were purged and additional insertion of active HF was repeated, as previously explained. At the final stage of the simulation at $t = 300$ ps, a single layer of SiO₂ was removed, and it is expected that more SiO₂ layers will be etched as the simulation time progresses.

For the systematic study of incident energy dependence on etching, we conducted additional simulations with incident energies of 20, 30, and 80 eV. Images of the final structure of all the simulations are presented in Figure 3.9. As shown, the amount of etched SiO₂ increased with the incident energy. For more information about temporal variations of silicon dioxide etching configurations with HF, temporal variations of incident energy of 20eV, 40eV, and 80eV are shown in Figure 3.10, Figure 3.11, and Figure 3.12. To analyze the effect of the incident energy of each HF molecule on the local chemical reaction at the SiO₂ surface, we calculated the dissociation fraction as a function of the incident energy, as shown in Figure 3.13-(a). The dissociation fraction is the probability of incident HF dissociating at the SiO₂ surface upon collision, and it is calculated by counting undissociated HF molecules during the purge process. As shown in Figure 3.13-(a), the dissociation fraction is an incremental function of the incident energy of HF. For a better understanding, we calculated the etching initiation time as a function of the incident energy, as shown in Figure 3.13-(b). The etching initiation time was defined as the moment when the first S–F bond was formed at the SiO₂ surface. Based on Figure 3.13-(b), we can conclude that the earlier initiation of etching with higher incident energy resulted in more chemical reactions at the SiO₂ surface during the etching process.

To provide a comprehensive explanation of the etching process for each simulation with different incident energies of HF molecules, we counted the number of SiF_x ($x = 4, 5, \text{ and } 6$) and H_2O molecules produced in the systems with different incident energies with respect to time, as shown in Figures 3.14-(a) and (b), respectively. Although SiF_4 was the primary volatile gas among the SiF_x gases that contributed to the etching process, SiF_5^- and SiF_6^{2-} were also produced from unreacted active HF reacting with SiF_4 . It is noteworthy that the numbers of SiF_x and H_2O molecules from $t = 50$ to 100 ps, $t = 150$ to 200 ps, and $t = 250$ to 300 ps did not show significant changes because no incident HF molecules were added to the system in the corresponding time steps for all cases with different incident energies. As shown in Figures 3.14-(a) and (b), more SiF_x and H_2O molecules were produced through the etching reaction with higher incident energy of HF molecules. Additionally, undesired byproduct molecules such as HF_3OSi , HF_5Si , and HF_4Si , other than SiF_x and H_2O , were present prior to the purge process. However, the amounts of these byproducts were relatively low, and some of these byproducts dissociated naturally prior to the purge process, as shown in Figure 3.14-(c); hence, they did not significantly affect the entire etching process. Also, radial distribution functions between Si and F for different incident energies and for different system temperature are shown in Figure 3.15, and Figure 3.16.

Finally, we plotted the etching yield, which refers to the number of removed SiO_2 molecules from the initial SiO_2 substrate per incident HF molecule, as shown in Figure 3.17. We discovered that the etching yield of the high-energy HF on the SiO_2 substrate increased with the incident energy, which is consistent with previous explanations regarding the effect of incident energy on the dissociation fraction and etching initiation time. During etching, physical sputtering of the substrate

occurred when the incident energy exceeded 100 eV. Therefore, because the incident energy of the etchant was less than that of the physical sputtering regime, we believe that our optimized ReaxFF can well describe the incident energy behavior of SiO₂ dry etching with incident HF molecules. Under the incident energy level where physical sputtering can be disregarded, the simulation results suggest that more etching reactions occurred when the incident energy of the etchant molecules increased. We believe that our simulation study will enable the systematic study of the dry etching process, and that the model used can be expanded to other chemical etching processes for various applications in the semiconductor industry.

3.4. Summary and discussions

In summary, we conducted an intermediate-size etching MD simulation using newly optimized ReaxFF field parameters for a Si/O/H/F system. The ReaxFF was developed by training against DFT data for energies of geometries and associated reactions in SiO₂ clusters and SiO₂ slabs (surface) for the etching process using HF molecules as an etchant. Through NEB and dimer method, we theoretically calculated reaction mechanisms of etching process of both SiO₂ cluster and SiO₂ slab using HF molecules. To validate the newly optimized ReaxFF parameters, we compared the calculated results using the ReaxFF and DFT, which indicated good agreement. Using this optimized ReaxFF, MD simulations of the

etching process of the SiO₂ surface using HF molecules were conducted. In MD simulations, we confirmed that the etching reaction occurs continuously as reaction mechanisms calculated in DFT. Because physical sputtering was accompanied by etching reactions with incident energies exceeding 100 eV, simulations with etchant incident energies of less than 100 eV were performed to investigate the chemical reactions between the SiO₂ substrate and HF molecules. In the SiO₂ etching process with an HF incident energy of 40 eV and a simulation runtime of 300 ps, we discovered that a single layer of SiO₂ substrate was removed and SiF_x gases were produced from etching reactions. By performing a systematic study based on different incident energies of 20, 30, and 80 eV, we observed a faster initiation of the etching reaction and higher dissociation fractions with higher incident energies. The SiO₂ etching simulation with HF etchant using the ReaxFF potential developed in this study facilitates a more comprehensive understanding of the computational chemical modeling of the etching process using Si-related surfaces with halogen/fluorine etchants.

3.5. Acknowledgment

This study was supported by a National Research Foundation of Korea (NRF) grant funded by the Korean government (Creative Material Discovery Project, NRF-2018M3D1A1058633) and Samsung Electronics.

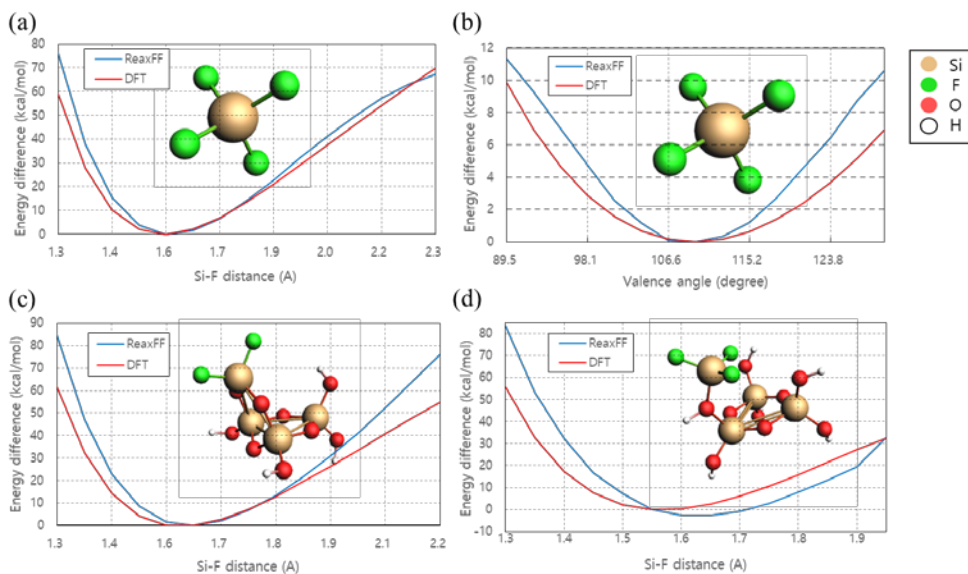


Figure 3.1 Minimum energy difference calculated using DFT and ReaxFF of (a) bond dissociation between Si and F for SiF₄, (b) valence angle distortion between (F–Si–F) for SiF₄, (c) bond dissociation between Si and F for SiO₂ cluster containing two Si–F bonds, and (d) bond dissociation between Si and F for SiO₂ cluster containing three Si–F bonds.

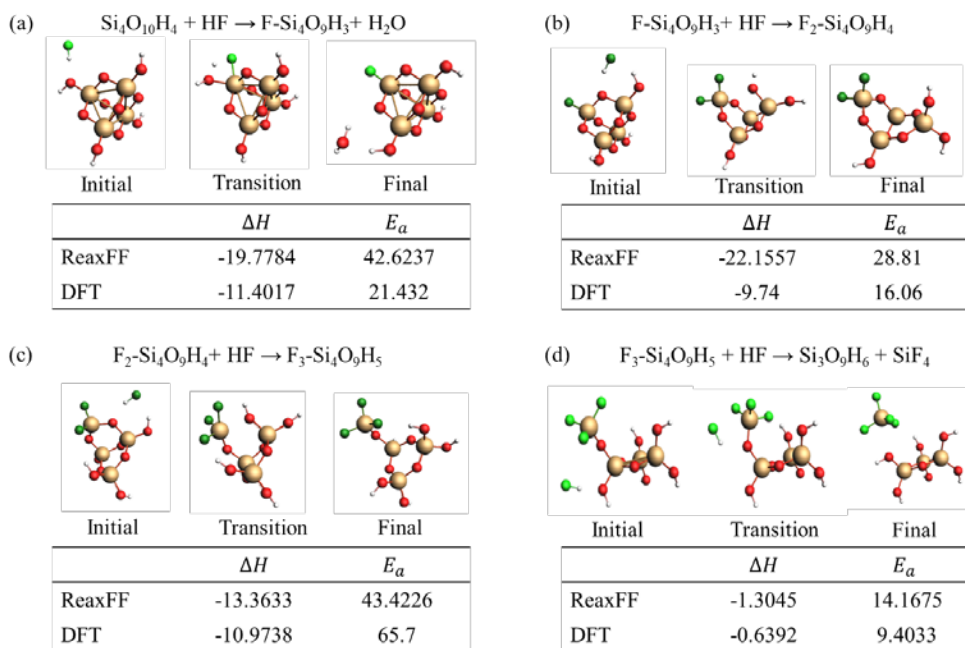


Figure 3.2 Four subsequent reactions forming SiF_4 using SiO_2 cluster model: HF reacting with (a) $\text{Si}_4\text{O}_{10}\text{H}_4$, (b) $\text{F-Si}_4\text{O}_9\text{H}_3$, (c) $\text{F}_2\text{-Si}_4\text{O}_9\text{H}_4$, and (d) $\text{F}_3\text{-Si}_4\text{O}_9\text{H}_5$.

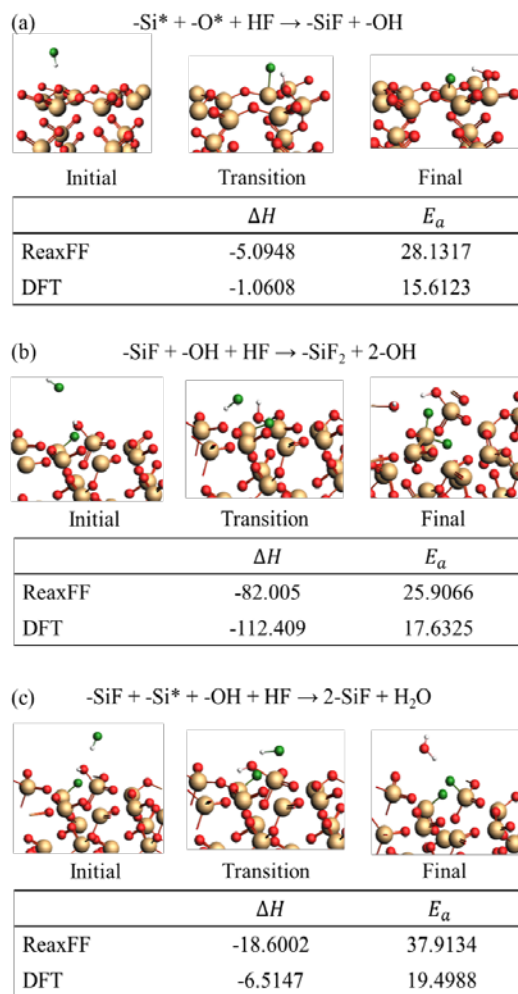


Figure 3.3 Early stage reactions using SiO_2 slab model. (a) HF reacts with surface forming one Si-F bond and one O-H bond where $-\text{Si}^*$ and $-\text{O}^*$ represent reactions sites. (b) HF reacts with surface containing one Si-F bond and one O-H bond forming additional Si-F bond in the same Si atom and additional O-H bond in neighboring Si atom. (c) HF reacts with surface containing one Si-F bond and one O-H bond forming additional Si-F bond in neighboring Si atom and producing H_2O where $-\text{Si}^*$ represents reaction site.

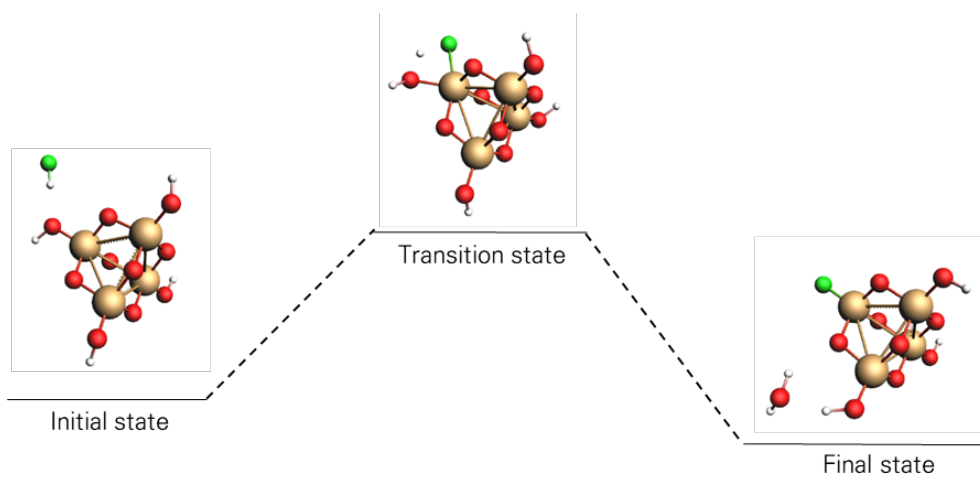


Figure 3.4 Schematic of reaction between silicon dioxide cluster and hydrogen fluoride gas.

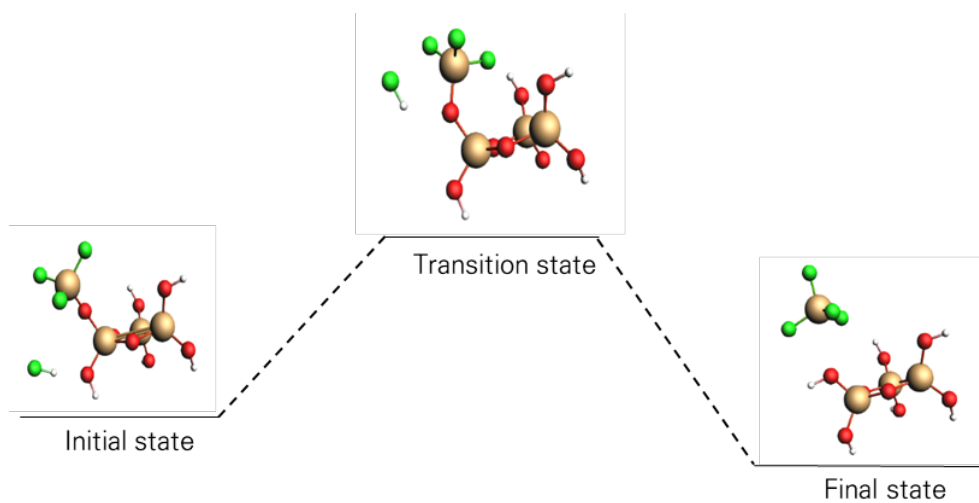


Figure 3.5 Schematic of reaction between silicon dioxide cluster with triple Si-F bond and hydrogen fluoride gas.

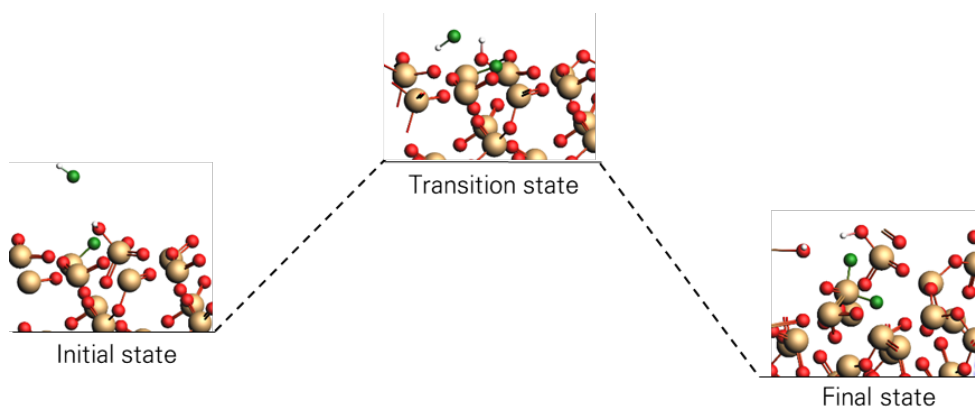


Figure 3.6 Schematic of reaction between silicon dioxide surface with single Si-F bond and hydrogen fluoride gas.

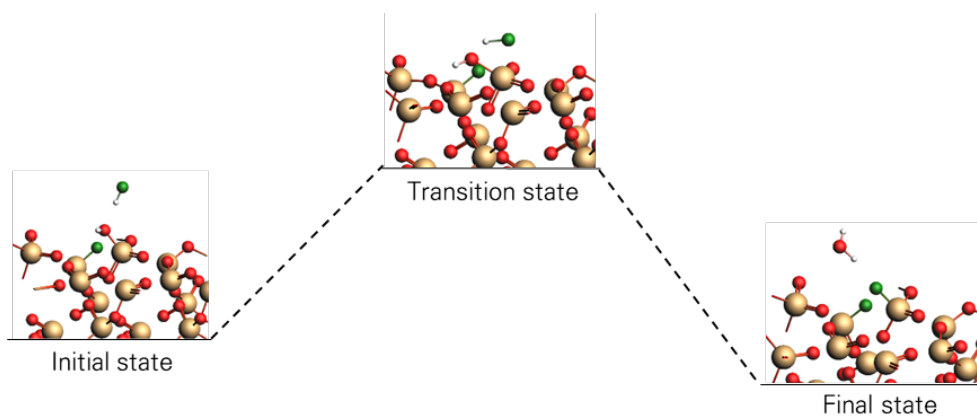


Figure 3.7 Schematic of reaction between silicon dioxide surface with single Si-F bond and hydrogen fluoride gas.

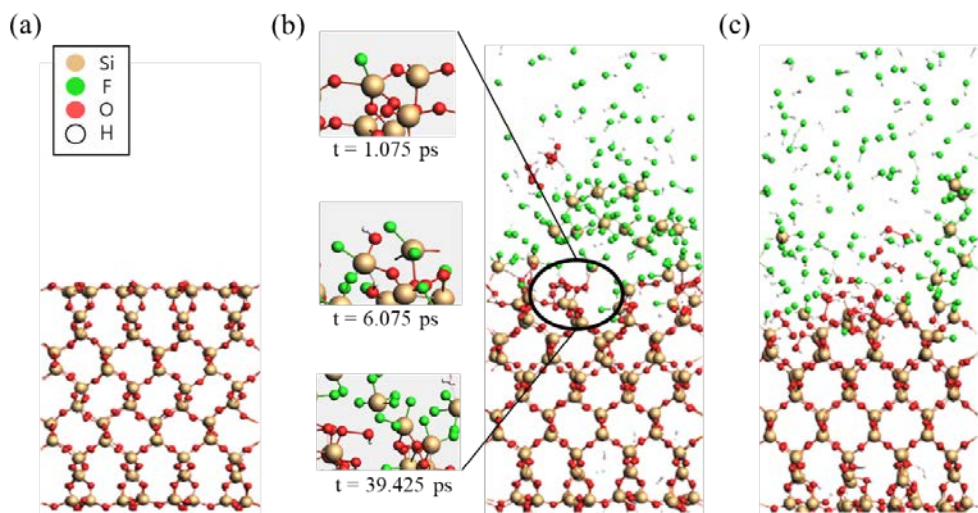


Figure 3.8 Images of etching process simulation with incident energy of 40 eV at (a) $t = 0$, (b) $t = 100$ ps, and (c) $t = 300$ ps. Insets of (b) show images of Si-F bond formation at $t = 1.075$ ps, O-H bond formation at $t = 6.075$ ps, and SiF₄ formation at $t = 39.425$ ps.

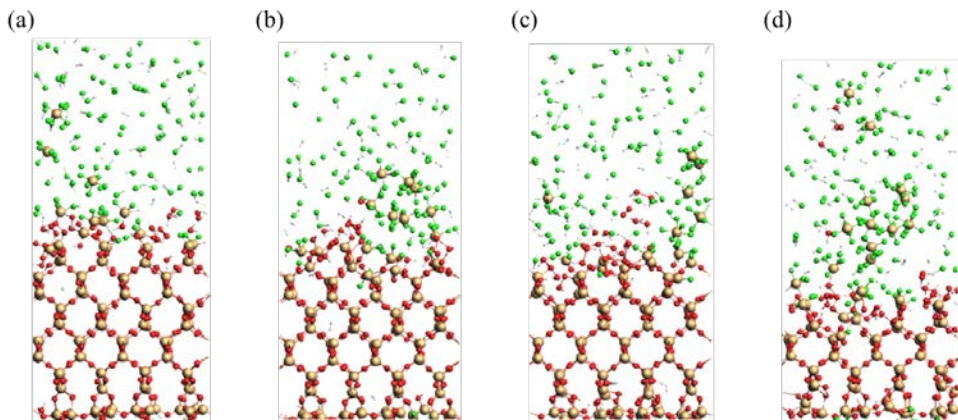


Figure 3.9 Final images of each etching simulation with different incident energies: (a) 20 eV, (b) 30 eV, (c) 40 eV, and (d) 80 eV.

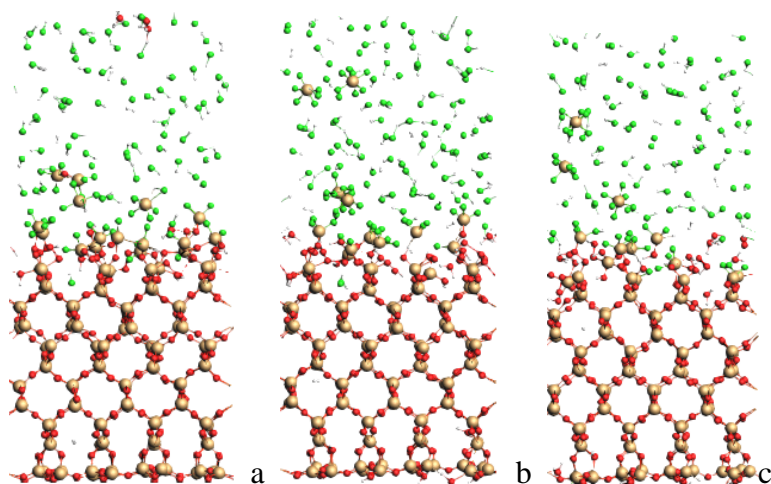


Figure 3.10 Temporal variations of silicon dioxide etching configurations with HF, 20eV incident energy. (a. $t=100\text{ps}$, b. $t=200\text{ps}$, c. $t=300\text{ps}$)

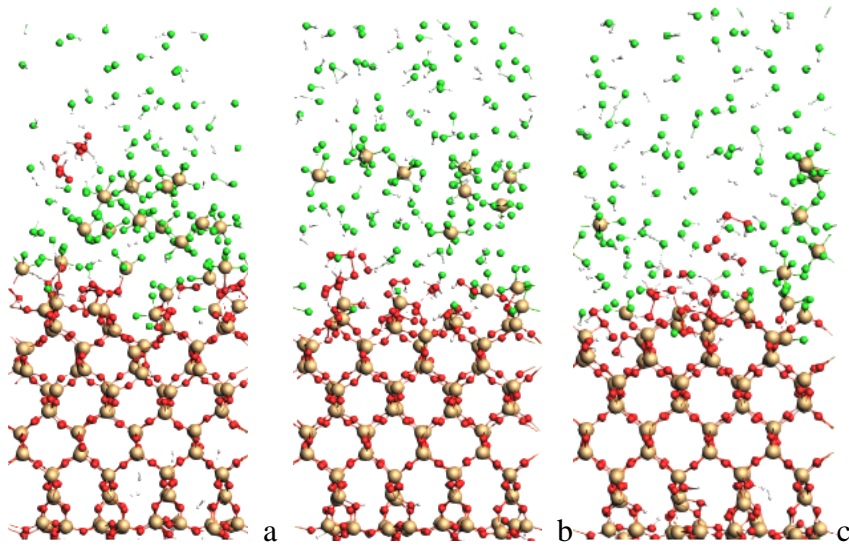


Figure 3.11 Temporal variations of silicon dioxide etching configurations with HF, 40eV incident energy. (a. $t=100\text{ps}$, b. $t=200\text{ps}$, c. $t=300\text{ps}$)

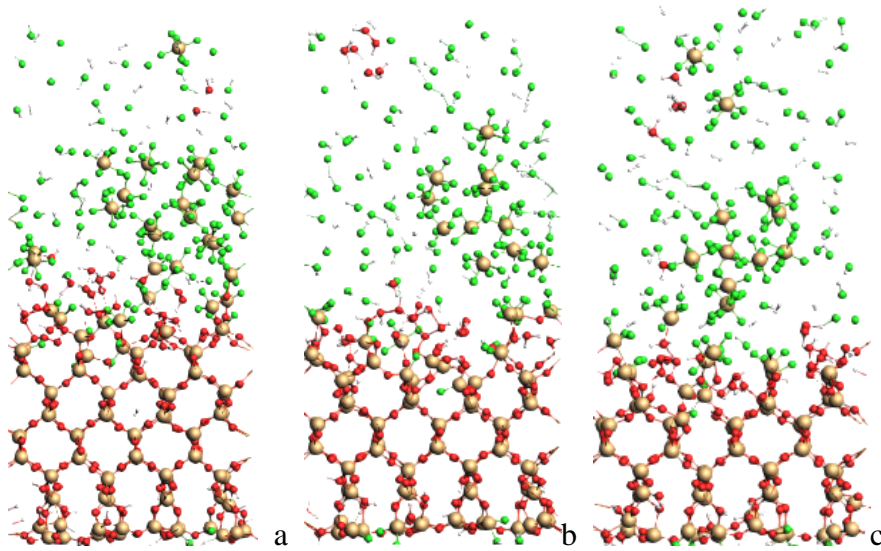


Figure 3.12 Temporal variations of silicon dioxide etching configurations with HF, 80eV incident energy. (a. $t=100\text{ps}$, b. $t=200\text{ps}$, c. $t=300\text{ps}$)

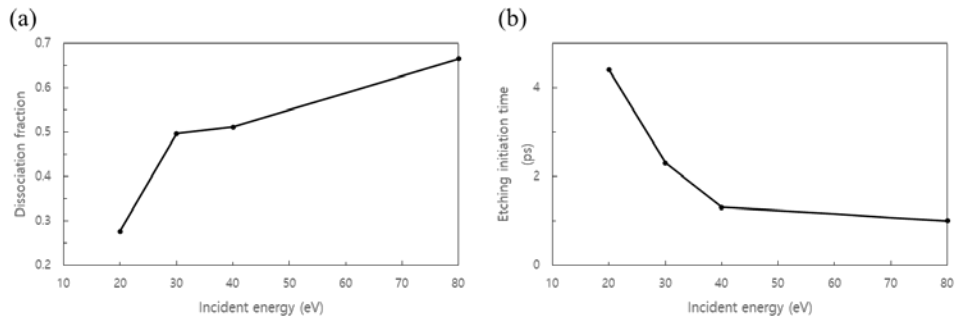


Figure 3.13 (a) Dissociation fraction and (b) etching initiation time with respect to incident energy of HF molecule.

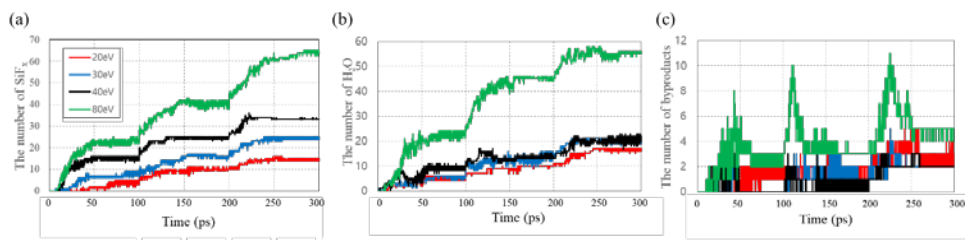


Figure 3.14 (a) Numbers of generated SiF_x , (b) H_2O , and (c) byproduct molecules with respect to time for four incident energies.

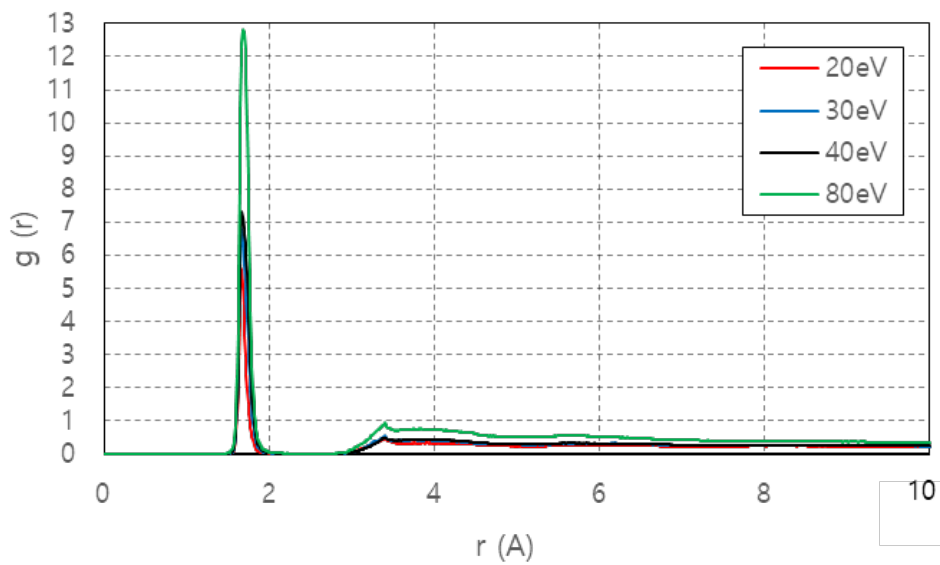


Figure 3.15 Radial distribution functions between Si and F for the four cases with different incident energies.

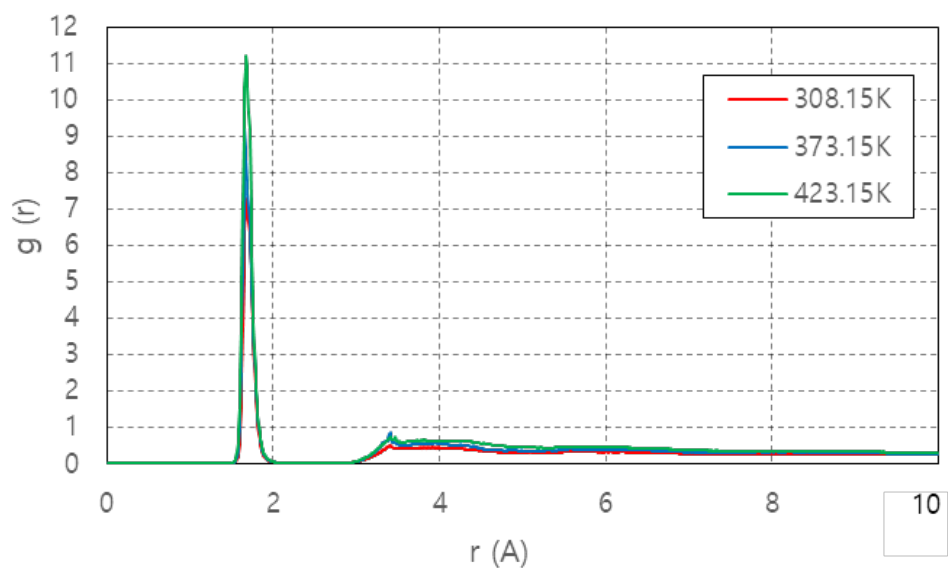


Figure 3.16 Radial distribution functions between Si and F for the three cases with different system temperature.

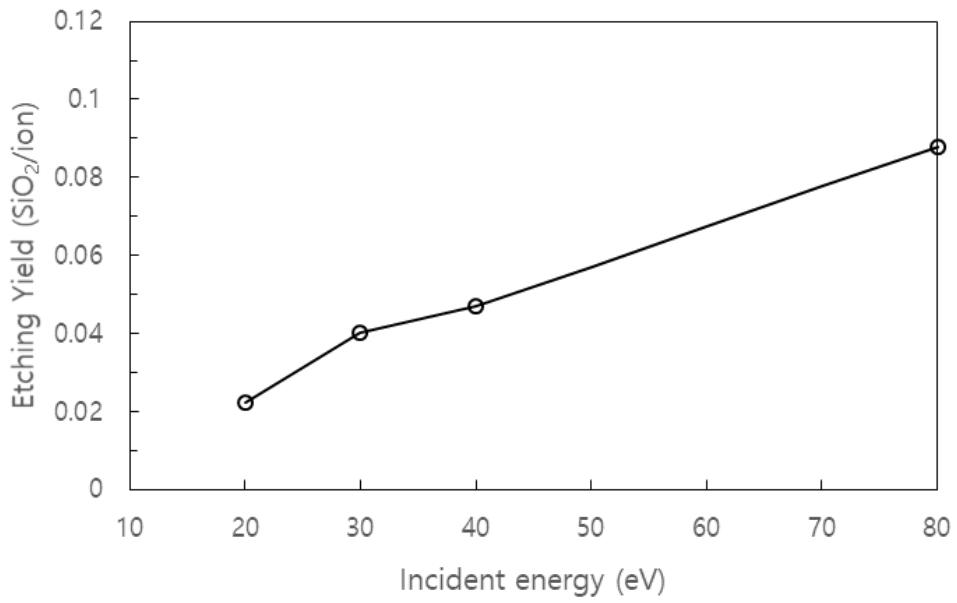


Figure 3.17 Etching yield of SiO₂ by HF molecule as a function of ion incident energy.

Table 3.1 Fitted parameters in developing Si-O-H-F force field

| Atom parameter (Si, F parameters) | | | | | |
|--|--|--|---|---------------------------------------|-----------------------------|
| Sigma bond radius (r_sigma) | van der Waals radius (r_vdW) | van der Waals dissociation energy (D_ij) | gammaEEM; EEM shielding (gamma_i) | van der Waals parameter (alpha_ij) | |
| van der Waals shielding (1/gamma_w) | Undercoordination energy (p_ovun5) | EEM electronegativity (chi_i) | EEM hardness (eta_i) | Bond order correction (p_boc4) | |
| Bond order correction (p_boc3) | Bond order correction (p_boc5) | Valence angle parameter (p_ovun2) | Valence angle parameter (p_val3) | Valence angle parameter (p_val5) | |
| Bond parameter (F-H, F-Si parameters) | | | | | |
| Sigma-bond dissociation energy (D_sigma) | Bond energy parameter (p_be1) | Overcoordination penalty (p_ovun1) | Bond energy parameter (p_be2) | Sigma bond order (p_bo1) | Sigma bond order (p_bo2) |
| Off diagonal parameter (F-H, F-Si parameters) | | | | | |
| VdW energy (D_ij) | VdW radius (r_vdW) | VdW parameter (alpha_ij) | Sigma bond length (r_sigma) | | |
| Valence angle parameter (F-Si-F, F-Si-O parameters) | | | | | |
| 180-[equilibrium angle] (Theta_0) | Valence angle parameter (p_val1) | Valence angle parameter (p_val2) | Undercoordination (p_val7) | Valence angle parameter (p_val4) | |

Table 3.2 Corrections to the ReaxFF parameter optimization ranges

| Parameter block | Atom types | Parameter index | Old ranges | New ranges |
|------------------------|-------------------|------------------------|-------------------|-------------------|
| Atoms | Si | 6 | [0.5947 0.8925] | [0.5947 0.75] |
| | | 15 | [5.5558 6.00] | [6.00 9.00] |
| Atoms | F | 6 | [0.30 0.30] | [0.30 0.80] |
| | | 15 | [15.00 15.00] | [6.00 15.00] |

Table 3.3 Optimized ReaxFF parameters for Si/O/H/F

39 ! Number of general parameters
50.0000 ! p_boc1 Eq(4c): Overcoordination parameter
9.5469 ! p_boc2 Eq(4d): Overcoordination parameter
26.5405 ! p_coa2 Eq(15): Valency angle conjugation
1.7224 ! p_trip4 Eq(20): Triple bond stabilisation
6.8702 ! p_trip3 Eq(20): Triple bond stabilisation
60.4850 ! k_c2 Eq(19): C2-correction
1.0588 ! p_ovun6 Eq(12): Undercoordination
4.6000 ! p_trip2 Eq(20): Triple bond stabilisation
12.1176 ! p_ovun7 Eq(12): Undercoordination
13.3056 ! p_ovun8 Eq(12): Undercoordination
-70.5044 ! p_trip1 Eq(20): Triple bond stabilization
0.0000 ! Lower Taper-radius (must be 0)
10.0000 ! R_cut Eq(21): Upper Taper-radius
2.8793 ! p_fe1 Eq(6a): Fe dimer correction
33.8667 ! p_val6 Eq(13c): Valency undercoordination
6.0891 ! p_lp1 Eq(8): Lone pair param
1.0563 ! p_val9 Eq(13f): Valency angle exponent
2.0384 ! p_val10 Eq(13g): Valency angle parameter
6.1431 ! p_fe2 Eq(6a): Fe dimer correction
6.9290 ! p_pen2 Eq(14a): Double bond/angle param
0.3989 ! p_pen3 Eq(14a): Double bond/angle param

3.9954 ! p_pen4 Eq(14a): Double bond/angle param
 -2.4837 ! p_fe3 Eq(6a): Fe dimer correction
 5.7796 ! p_tor2 Eq(16b): Torsion/BO parameter
 10.0000 ! p_tor3 Eq(16c): Torsion overcoordination
 1.9487 ! p_tor4 Eq(16c): Torsion overcoordination
 -1.2327 ! p_elho Eq(26a): electron-hole interaction
 2.1645 ! p_cot2 Eq(17b): Conjugation if tors13=0
 1.5591 ! p_vdW1 Eq(23b): vdWaals shielding
 0.1000 ! Cutoff for bond order (*100)
 2.1365 ! p_coa4 Eq(15): Valency angle conjugation
 0.6991 ! p_ovun4 Eq(11b): Over/Undercoordination
 50.0000 ! p_ovun3 Eq(11b): Over/Undercoordination
 1.8512 ! p_val8 Eq(13d): Valency/lone pair param
 0.5000 ! X_soft Eq(25): ACKS2 softness for X_ij
 20.0000 ! d Eq(23d): Scale factor in lg-dispersion
 5.0000 ! p_val Eq(27): Gauss exponent for electrons
 0.0000 ! 1 Eq(13e): disable undecoord in val angle
 2.6962 ! p_coa3 Eq(15): Valency angle conjugation

 6 ! Number of atoms;
 R(sigma);Valence;Atomic;R(VdW);E(VdW);EEM;R(pi);Num;Alpha(VdW);Gamma;
 !
 valency;p(ovun5);p_xel2;EEM;EEM;Type;R(pi2);E(lp);HeatForm;p_boc4;

 ! p_boc3;p_boc5;Softcut(ACKS2);Alpha(e-
 reax);p_ovun2;p_val3;Beta(e-reax);Val^boc;p_val5;R(core);

! E(core);A(core);

| | | | | | | | | |
|----|----------|---------|----------|---------|----------|--------|---------|--------|
| H | 0.8707 | 1.0000 | 1.0080 | 1.4947 | 0.0785 | 0.7599 | -0.1000 | 1.0000 |
| | 8.1936 | 33.9645 | 1.0000 | 0.0000 | 121.1250 | 3.6146 | 9.8692 | 1.0000 |
| | -0.1000 | 0.0000 | 59.3302 | 3.3628 | 2.2226 | 0.0022 | 1.0698 | 0.0000 |
| | -19.4527 | 4.4710 | 1.0338 | 1.0000 | 2.8793 | 0.0000 | 0.0000 | 0.0000 |
| O | 1.4075 | 2.0000 | 15.9990 | 1.4115 | 0.0977 | 1.0950 | 1.0878 | 6.0000 |
| | 9.6471 | 16.6038 | 4.0000 | 38.3368 | 116.0768 | 7.9705 | 8.8485 | 2.0000 |
| | 0.9050 | 27.8683 | -1.0116 | 2.3988 | 4.0090 | 0.0028 | 0.9745 | 0.0000 |
| | -3.3587 | 3.2099 | 1.0493 | 4.0000 | 2.9225 | 0.0000 | 0.0000 | 0.0000 |
| N | 1.2335 | 3.0000 | 14.0000 | 2.2402 | 0.1057 | 0.5903 | 1.3517 | 5.0000 |
| | 9.6729 | 12.7207 | 4.0000 | 31.5285 | 100.0000 | 6.1159 | 7.4005 | 2.0000 |
| | 1.0345 | 0.0868 | 129.5034 | 0.6274 | 7.0842 | 2.7565 | 0.9745 | 0.0000 |
| | -2.0090 | 4.2982 | 1.0183 | 4.0000 | 2.8793 | 0.0000 | 0.0000 | 0.0000 |
| Si | 1.9733 | 4.0000 | 28.0600 | 2.0654 | 0.1928 | 0.7500 | 1.2223 | 4.0000 |
| | 12.1892 | 1.2539 | 4.0000 | 21.4869 | 139.9309 | 1.8038 | 6.0009 | 0.0000 |
| | -1.0000 | 0.0000 | 104.0224 | 8.2570 | 5.2300 | 0.8381 | 0.8563 | 0.0000 |
| | -4.8039 | 2.0754 | 1.0338 | 4.0000 | 2.7786 | 0.0000 | 0.0000 | 0.0000 |
| F | 1.1978 | 1.0000 | 18.9984 | 1.5723 | 0.1254 | 0.3000 | -0.1000 | 7.0000 |
| | 11.3841 | 9.4986 | 4.0000 | 7.3951 | 0.2000 | 9.0000 | 15.0000 | 0.0000 |
| | -1.0000 | 34.9703 | 17.9169 | 7.9796 | 5.1771 | 1.0561 | 0.0000 | 0.0000 |
| | -5.3030 | 3.1624 | 1.0493 | 4.0000 | 2.4240 | 0.0000 | 0.0000 | 0.0000 |
| X | -0.1000 | 2.0000 | 1.0080 | 2.0000 | 0.0000 | 1.0000 | -0.1000 | 6.0000 |
| | 10.0000 | 2.5000 | 4.0000 | 0.0000 | 0.0000 | 8.5000 | 1.5000 | 0.0000 |

-0.1000 0.0000 127.6226 8.7410 13.3640 0.6690 0.9745 0.0000
 -11.0000 2.7466 1.0338 6.2998 2.8793 0.0000 0.0000 0.0000

15 ! Number of bonds;
 E(Sigma);E(Pi);E(Pi2);p_be1;p_bo5;13corr;p_bo6;p_ovun1;

! p_be2;p_bo3;p_bo4;Reserved;p_bo1;p_bo2;ovcoord;p_xell;

1 1 153.3934 0.0000 0.0000 -0.4600 0.0000 1.0000 6.0000
 0.7300

6.2500 1.0000 0.0000 1.0000 -0.0790 6.0552 0.0000
 0.0000

2 2 142.2858 145.0000 50.8293 0.2506 -0.1000 1.0000 29.7503
 0.6051

0.3451 -0.1055 9.0000 1.0000 -0.1225 5.5000 1.0000
 0.0000

3 2 130.8596 169.4551 40.0000 0.3837 -0.1639 1.0000 35.0000
 0.2000

1.0000 -0.3579 7.0004 1.0000 -0.1193 6.8773 1.0000
 0.0000

3 3 0.0000 82.5526 152.5336 0.4010 -0.1034 1.0000 12.4261
 0.5828

0.1578 -0.1509 11.9186 1.0000 -0.0861 5.4271 1.0000
 0.0000

1 2 160.0000 0.0000 0.0000 -0.5725 0.0000 1.0000 6.0000
 0.5626

1.1150 1.0000 0.0000 0.0000 -0.0920 4.2790 0.0000
 0.0000

1 3 205.6821 0.0000 0.0000 -0.3364 0.0000 1.0000 6.0000
 0.4547

| | | | | | | | | |
|---|---|----------|---------|---------|---------|---------|---------|---------|
| | | 6.9381 | 1.0000 | 0.0000 | 1.0000 | -0.1310 | 5.5195 | 0.0000 |
| | | 0.0000 | | | | | | |
| 1 | 4 | 250.0000 | 0.0000 | 0.0000 | -0.7128 | 0.0000 | 1.0000 | 6.0000 |
| | | 0.1186 | | | | | | |
| | | 18.5790 | 1.0000 | 0.0000 | 1.0000 | -0.0731 | 7.4983 | 0.0000 |
| | | 0.0000 | | | | | | |
| 2 | 4 | 272.8709 | 18.4462 | 0.0000 | -0.6107 | -0.3000 | 1.0000 | 36.0000 |
| | | 0.8270 | | | | | | |
| | | 10.2334 | -0.5495 | 29.9954 | 1.0000 | -0.1277 | 7.5863 | 1.0000 |
| | | 0.0000 | | | | | | |
| 3 | 4 | 119.7136 | 41.2405 | 43.3991 | -0.2060 | -0.3000 | 1.0000 | 36.0000 |
| | | 0.7957 | | | | | | |
| | | 0.8189 | -0.2614 | 9.4060 | 1.0000 | -0.1245 | 6.1856 | 1.0000 |
| | | 0.0000 | | | | | | |
| 4 | 4 | 89.5435 | 47.8775 | 30.0000 | 0.6058 | -0.3000 | 1.0000 | 16.0000 |
| | | 0.0146 | | | | | | |
| | | 0.3287 | -0.1777 | 4.6512 | 1.0000 | -0.0606 | 7.8945 | 0.0000 |
| | | 0.0000 | | | | | | |
| 5 | 1 | 211.3004 | 0.0000 | 0.0000 | -0.4643 | -0.2000 | 0.0000 | 16.0000 |
| | | 0.6151 | | | | | | |
| | | 12.3710 | -0.2000 | 15.0000 | 1.0000 | -0.1593 | 7.5013 | 0.0000 |
| | | 0.0000 | | | | | | |
| 5 | 2 | 0.0000 | 0.0000 | 0.0000 | 0.2500 | -0.5000 | 1.0000 | 45.0000 |
| | | 0.6000 | | | | | | |
| | | 0.4000 | -0.2500 | 15.0000 | 1.0000 | -0.1000 | 10.0000 | 1.0000 |
| | | 0.0000 | | | | | | |
| 5 | 3 | 0.0000 | 0.0000 | 0.0000 | -0.4643 | 0.0000 | 1.0000 | 6.0000 |
| | | 0.6151 | | | | | | |

12.3710 1.0000 0.0000 1.0000 -0.0098 8.5980 0.0000
0.0000

5 4 242.0786 0.0000 0.0000 -0.2499 -0.3500 1.0000 25.0000
0.3295

9.9995 -0.2500 15.0000 1.0000 -0.2000 5.4855 1.0000
0.0000

5 5 0.0000 0.0000 0.0000 0.1901 -0.3500 1.0000 35.0000
0.7500

0.3355 -0.2500 25.0000 1.0000 -0.1250 6.5000 1.0000
0.0000

8 ! Number of off-diagonal terms;
E(VdW);R(VdW);Alpha(VdW);R(sigma);R(pi);R(pi2);C(lg);

1 2 0.0283 1.2885 10.9190 0.9215 -1.0000 -1.0000

1 3 0.1242 1.3413 9.9589 0.9997 -1.0000 -1.0000

3 2 0.1201 2.4775 9.0171 1.5285 1.0682 1.2716

1 4 0.1659 1.4000 11.7054 1.3437 -1.0000 -1.0000

2 4 0.1330 2.0545 10.8315 1.7043 1.3773 -1.0000

3 4 0.1297 1.9384 10.9856 1.6175 1.4045 -1.0000

5 1 0.0818 1.7031 10.0000 1.1666 -1.0000 -1.0000

5 4 0.2144 1.2971 13.9999 1.8607 -1.0000 -1.0000

47 ! Number of angles;
Theta0;p_val1;p_val2;p_coal;p_val7;p_pen1;p_val4;

1 1 1 0.0000 27.9213 5.8635 0.0000 0.0000 0.0000 1.0400

2 2 2 89.9934 17.9465 1.7798 0.0000 2.9881 0.0000 1.0538

3 2 2 83.5202 33.7933 1.0337 0.0000 2.9000 0.0000 1.3398

| | | | | | | | | | |
|---|---|---|---------|---------|--------|----------|--------|--------|--------|
| 3 | 2 | 3 | 67.1317 | 42.3748 | 1.7873 | 0.0000 | 3.0072 | 0.0000 | 1.5832 |
| 1 | 2 | 2 | 75.6935 | 50.0000 | 2.0000 | 0.0000 | 1.0000 | 0.0000 | 1.1680 |
| 1 | 2 | 3 | 72.7348 | 20.1071 | 7.5000 | 0.0000 | 0.1000 | 0.0000 | 1.0746 |
| 1 | 2 | 1 | 85.8000 | 9.8453 | 2.2720 | 0.0000 | 2.8635 | 0.0000 | 1.5800 |
| 2 | 3 | 2 | 74.2613 | 20.9008 | 2.8607 | -18.0069 | 3.0701 | 0.0000 | 1.3874 |
| 3 | 3 | 2 | 74.2615 | 27.8669 | 1.6736 | -0.9193 | 3.0117 | 0.0000 | 1.4381 |
| 3 | 3 | 3 | 73.3189 | 24.9685 | 2.2561 | 0.0000 | 2.9983 | 0.0000 | 2.1573 |
| 1 | 3 | 2 | 74.5739 | 45.0000 | 1.4078 | 0.0000 | 0.3956 | 0.0000 | 3.0000 |
| 1 | 3 | 3 | 79.7136 | 45.0000 | 0.5316 | 0.0000 | 0.5437 | 0.0000 | 1.0000 |
| 1 | 3 | 1 | 78.6680 | 6.9060 | 3.7869 | 0.0000 | 0.0223 | 0.0000 | 2.0220 |
| 2 | 1 | 2 | 0.0000 | 15.0000 | 2.8900 | 0.0000 | 0.0000 | 0.0000 | 2.8774 |
| 3 | 1 | 2 | 0.0000 | 1.0574 | 0.1000 | 0.0000 | 0.0000 | 0.0000 | 2.7676 |
| 3 | 1 | 3 | 0.0000 | 0.0100 | 1.0929 | 0.0000 | 0.0000 | 0.0000 | 2.1728 |
| 1 | 1 | 2 | 0.0000 | 8.5744 | 3.0000 | 0.0000 | 0.0000 | 0.0000 | 1.0421 |
| 1 | 1 | 3 | 0.0000 | 0.0019 | 6.0000 | 0.0000 | 0.0000 | 0.0000 | 1.0400 |
| 4 | 4 | 4 | 77.4746 | 39.1276 | 0.8607 | 0.0000 | 0.0024 | 0.0000 | 1.2899 |
| 1 | 4 | 4 | 77.2616 | 5.0190 | 7.8944 | 0.0000 | 4.0000 | 0.0000 | 1.0400 |
| 1 | 4 | 1 | 75.7983 | 14.4132 | 2.8640 | 0.0000 | 4.0000 | 0.0000 | 1.0400 |
| 2 | 4 | 4 | 99.8997 | 26.6610 | 2.1237 | 0.0000 | 0.0100 | 0.0000 | 1.4341 |
| 1 | 4 | 2 | 73.6998 | 40.0000 | 1.8782 | 0.0000 | 4.0000 | 0.0000 | 1.1290 |
| 2 | 4 | 2 | 98.2184 | 38.9429 | 0.7727 | 0.0000 | 1.1658 | 0.0000 | 2.2641 |
| 4 | 2 | 4 | 39.2858 | 1.3068 | 5.6478 | 0.0000 | 3.8972 | 0.0000 | 3.0000 |
| 1 | 2 | 4 | 79.2126 | 4.8973 | 8.0000 | 0.0000 | 1.0859 | 0.0000 | 2.1209 |

| | | | | | | | | | |
|---|---|---|---------|---------|--------|--------|--------|--------|--------|
| 2 | 2 | 4 | 82.7397 | 32.1198 | 1.8862 | 0.0000 | 0.1058 | 0.0000 | 1.5443 |
| 1 | 1 | 4 | 0.0000 | 47.1300 | 6.0000 | 0.0000 | 1.6371 | 0.0000 | 1.0400 |
| 4 | 1 | 4 | 0.0000 | 27.4206 | 6.0000 | 0.0000 | 1.6371 | 0.0000 | 1.0400 |
| 2 | 1 | 4 | 0.0000 | 7.0550 | 3.9236 | 0.0000 | 1.6371 | 0.0000 | 1.0400 |
| 3 | 4 | 4 | 60.6199 | 17.7559 | 1.0576 | 0.0000 | 2.1459 | 0.0000 | 1.0400 |
| 3 | 4 | 3 | 74.1294 | 20.6494 | 2.1244 | 0.0000 | 0.7689 | 0.0000 | 1.0400 |
| 3 | 4 | 2 | 57.0650 | 9.4985 | 0.3423 | 0.0000 | 0.7689 | 0.0000 | 1.0400 |
| 4 | 3 | 4 | 24.1137 | 1.7457 | 0.2198 | 0.0000 | 4.1125 | 0.0000 | 1.0400 |
| 1 | 4 | 3 | 68.7410 | 15.5851 | 1.8545 | 0.0000 | 0.8613 | 0.0000 | 1.0400 |
| 1 | 3 | 4 | 80.9040 | 4.0560 | 1.2284 | 0.0000 | 1.6982 | 0.0000 | 1.0400 |
| 3 | 3 | 4 | 60.0000 | 10.0000 | 0.7500 | 0.0000 | 1.0000 | 0.0000 | 1.0400 |
| 2 | 3 | 4 | 69.8728 | 32.7155 | 1.5875 | 0.0000 | 2.2466 | 0.0000 | 1.0400 |
| 3 | 2 | 4 | 69.8728 | 27.1273 | 1.5875 | 0.0000 | 2.2466 | 0.0000 | 1.0400 |
| 3 | 1 | 4 | 0.0000 | 31.0427 | 4.5625 | 0.0000 | 1.6371 | 0.0000 | 1.0400 |
| 5 | 4 | 4 | 79.7014 | 16.9791 | 1.6839 | 0.0000 | 1.0944 | 0.0000 | 1.0500 |
| 5 | 4 | 5 | 90.9986 | 68.2397 | 4.5675 | 0.0000 | 4.0451 | 0.0000 | 1.0000 |
| 4 | 5 | 4 | 0.0000 | 42.3353 | 7.1082 | 0.0000 | 1.3635 | 0.0000 | 1.0840 |
| 5 | 5 | 4 | 0.0000 | 10.0000 | 2.0000 | 0.0000 | 1.0000 | 0.0000 | 1.2500 |
| 5 | 5 | 5 | 0.0000 | 10.0000 | 2.0000 | 0.0000 | 1.0000 | 0.0000 | 1.2500 |
| 5 | 1 | 5 | 0.0000 | 0.0000 | 0.0000 | 0.0000 | 0.0000 | 0.0000 | 1.0000 |
| 5 | 4 | 2 | 28.9834 | 39.9921 | 1.2589 | 0.0000 | 2.1212 | 0.0000 | 1.0000 |

14 ! Number of torsions;

Theta0;p_val1;p_val2;p_coa1;p_val7;p_pen1;p_val4;

| | | | | | | | | | | |
|---|---|---|---|---------|----------|---------|---------|---------|--------|--------|
| 1 | 2 | 2 | 1 | -2.1995 | -25.0000 | -1.0000 | -2.6000 | -0.9921 | 0.0000 | 0.0000 |
| 1 | 2 | 2 | 2 | -2.5000 | 43.1840 | -0.6826 | -6.6539 | -1.2407 | 0.0000 | 0.0000 |
| 2 | 2 | 2 | 2 | -2.5000 | -25.0000 | 1.0000 | -2.5000 | -0.9000 | 0.0000 | 0.0000 |
| 0 | 1 | 1 | 0 | 0.0000 | 0.0000 | 0.0000 | 0.0000 | 0.0000 | 0.0000 | 0.0000 |
| 0 | 1 | 2 | 0 | 0.0000 | 0.1000 | 0.0200 | -2.5415 | 0.0000 | 0.0000 | 0.0000 |
| 0 | 2 | 2 | 0 | 0.5511 | 25.4150 | 1.1330 | -5.1903 | -1.0000 | 0.0000 | 0.0000 |
| 0 | 1 | 3 | 0 | 0.0000 | 0.1032 | 0.3000 | -5.0965 | 0.0000 | 0.0000 | 0.0000 |
| 0 | 3 | 2 | 0 | 1.1397 | 61.3225 | 0.5139 | -3.8507 | -2.7831 | 0.0000 | 0.0000 |
| 0 | 3 | 3 | 0 | 0.7265 | 44.3155 | 1.0000 | -4.4046 | -2.0000 | 0.0000 | 0.0000 |
| 1 | 4 | 4 | 1 | 0.0000 | 0.0000 | 0.0640 | -2.4426 | 0.0000 | 0.0000 | 0.0000 |
| 1 | 4 | 4 | 4 | 0.0000 | 0.0000 | 0.1587 | -2.4426 | 0.0000 | 0.0000 | 0.0000 |
| 0 | 1 | 4 | 0 | 0.0000 | 0.0000 | 0.1200 | -2.4847 | 0.0000 | 0.0000 | 0.0000 |
| 0 | 3 | 4 | 0 | 0.0000 | 0.0000 | 0.0000 | -2.4426 | 0.0000 | 0.0000 | 0.0000 |
| 0 | 5 | 5 | 0 | 4.0000 | 45.8264 | 0.9000 | -4.0000 | 0.0000 | 0.0000 | 0.0000 |

5 ! Number of hydrogen bonds;
Theta0;p_val1;p_val2;p_coa1;p_val7;p_pen1;p_val4;

| | | | | | | |
|---|---|---|--------|---------|--------|---------|
| 2 | 1 | 2 | 2.1200 | -3.5800 | 1.4500 | 19.5000 |
| 2 | 1 | 3 | 2.1215 | -7.5000 | 1.4500 | 19.5000 |
| 3 | 1 | 2 | 1.7500 | -4.3286 | 1.4500 | 19.5000 |
| 3 | 1 | 3 | 2.4000 | -2.3575 | 1.4500 | 19.5000 |
| 5 | 1 | 2 | 2.1200 | -2.0000 | 1.4500 | 19.5000 |

Chapter 4. Adsorption energy calculations

in Li-S batteries

Reproduced in part with permission from Soochan Kim, Dong Hyun Kim, Misuk Cho, Won Bo Lee, and Youngkwan Lee. Fast-charging lithium-sulfur batteries enabled via lean binder content, *Small*, 2004372 (2020) and Long-life lithium-sulfur battery enabled by a multifunctional gallium oxide shield, *Chemical Engineering Journal* 420, 129772 (2021).

4.1. Elastic chitosan based lean content binder

4.1.1 Introduction

Li-S batteries (LSBs) have received incredible research interest as a next generation energy storage device due to the advantages of sulfur (S), which include its abundance in nature, low-cost, high theoretical specific capacity (1675 mAh g^{-1}). Despite its great potential on high energy density, there are still several challenges in LSB researches: shuttle effects resulting from the dissolution and diffusion of lithium polysulfide (LPS), the insulating nature of S/Li₂S, and severe volume

change (~80%) of S during the charge/discharge process. The main issue is the shuttle effects by LPS and many researches are focused on the suppression of shuttle effects.

Recently, various polar materials have been applied to LSBs like as metal-based compounds and organic materials with abundant functional groups. Outstanding high capacity and long-life Li-S batteries with improved suppression of LPS shuttle effects have been reported. As the commercialization of Li-S batteries is approaching, the needs for fast charging for small applications (portable personal devices, drone, etc.), and the demands for research that enables high-power delivery for large applications such as electric vehicles and electrical grids, is increasing. [Nat. Commun, (2019) 10, 1933; ACS Sustainable Chem. Eng. 2017, 5, 2799–2816; *Adv. Mater.* 2018, 30,

1804084]

For the fast charging and high-power delivery, LSB must be maintained the mechanical properties and capacitive performance at high C-rate, which enabled by high electrode stability and improved ion conductivity. In order to improve the stability of the electrode, a large amount of the polymer binder, which can hold the active materials with current collector, is required. However, since the binder is generally an insulator, raising the content of the binder leads to an increase in the internal resistance of the LSB. Therefore, for stable and remarkable performance of LSB at high C-rate, the polymer binder should be able to improve the stability of the electrode with a small amount and strong mechanical properties.

In this work, we designed a functional binder to realize a durable LSB at high C-rate through modulating the characteristics of chitosan and carboxylated nitrile butadiene rubber (XNBR) and controlling the contents of binder toward extreme low level. The designed binder showed improved toughness accommodating

volume changes of electrode by formation of intermolecular amide and hydrogen bonding, as well as the high LPS adsorption capacity. Chitosan provided the mechanical strength with excellent LPS adsorption ability, and XNBR attributed the toughness and adhesion. In addition, the content of the prepared binder was reduced to an extreme small amount (3 wt. %), thereby improving the overall energy density and enabling facile ion/electron transport to implement an efficient electrochemical system. Prepared Li-S cell using 3 wt. % optimized binder exhibited stable cycling with a capacity retention decay of 0.024 % after 500 cycles (2 C-rate), 0.026 % after 500 cycles (5 C-rate), and 0.034 % after 300 cycles (10 C-rate). Our designed binder could provide new insights toward the development of commercial next generation energy storages capable of high-power delivery.

4.1.2 Model and computational method

Designed new binder is prepared through considering each characteristics of polymers. For the design of new binder, chitosan can provide their high affinity to LPS and mechanical properties and combination with XNBR can support the elasticity and good adhesion like schematic expression shown in **Figure 4.1.1a**, To integrate their properties, they are simply mixed in an aqueous solution, and cross-linked by heat treatment at 90 °C for 1h. Figure 4.1.1b presents a schematic expression about formation of the designed binder (chitosan-XNBR), which is consisted of amide bonding and hydrogen bonding. These intramolecular bonding could improve the mechanical properties of polymer film. Figure 4.1.1c exhibits

the FT-IR spectra of chitosan, chitosan-XNBR, and XNBR. The chitosan showed characteristic absorption peaks at (1654, 1588, 1420, 1380, 1156, and 1036) cm^{-1} for C=O stretching, N-H bending, N-H deformation, C-N stretching, C-O-C stretching, and O-H bending vibration, respectively. The XNBR presented characteristic peak at 2237 cm^{-1} is ascribed to $-\text{C}=\text{N}$ stretching attributing to the nitrile group in the spectrum of XNBR. The peaks around 1650-1700 cm^{-1} are ascribed to $-\text{C}=\text{O}$ stretching attributing to the carboxyl group. The butadiene part of XNBR displayed the distinct peaks at 964 and 915 cm^{-1} is ascribed to $=\text{C}-\text{H}$ bending. In chitosan-XNBR, each characteristic peaks are observed and the peak at 1675 cm^{-1} was attributed to amide I ($\text{R}-\text{CONH}-\text{R}'$, C=O stretching) and that at 1580 cm^{-1} was attributed to amide II ($\text{R}-\text{NH}-\text{R}'$, NH_2 deformation, N-H bending and C-N stretching). Moreover, the 1588 cm^{-1} (from chitosan) were downshifted to 1580 cm^{-1} , which indicated the formation of the new amide bond. In addition, the deformation vibration of $-\text{NH}_2$ at 1420 cm^{-1} downshifted to 1412 cm^{-1} , which implied the formation of chitosan-XNBR network.

Figures 4.1.1d-4.1.1e show the XPS Spectra of chitosan-XNBR. Among the peaks, 289.0 eV of C1s spectrum and 401.2 eV of N1s spectrum exhibited an appearance of the $\text{C}-\text{NHC}=\text{O}$, which indicated amide bond formation between chitosan and XNBR. Moreover, as the result of solubility test, chitosan film is dissolved in acetic acid solution, but prepared chitosan-XNBR film was not dissolved. From this solubility test, it was confirmed the formation of crosslinking in chitosan-XNBR film (**Figure 4.1.2**).

To estimate the chemical adsorption capacity of the prepared polymers for LPS (Li_2S_6), LPS adsorbed on prepared polymers was studied with DFT calculations, which was performed using Vienna ab-initio simulations package (VASP). The

projector augmented wave (PAW) pseudopotential was adopted and the generalized gradient approximation (GGA) exchange-correlation function described by Perdew-Burke-Ernzerhof (PBE). To guarantee convergence, the energy tolerance and force tolerance were set to 10^{-5} and 0.05 eV/Å. The cut-off energy of the plane-wave basis was 400 eV. In order to evaluate the long-range effects, adsorption energies were calculated using the DFT-D3 method with Becke-Jonson damping, where the van der Waals interaction (vdW) was considered. For structural optimizations, the molecules were in a cubic box of $30 \times 30 \times 30 \text{ \AA}^3$ and the nearest distance between polymers and its images were kept over 15 Å to avoid the periodic image interactions. Chitosan and XNBR molecule model for DFT calculations are shown in Figure 4.1.3. The binding energy of LPS and polymers E_{ad} was defined as $E_{ad} \text{ (eV)} = E_{\text{polymer+LPS}} - (E_{\text{polymer}} + E_{\text{LPS}})$ where $E_{\text{polymer+LPS}}$ was the total energy of polymer with LPS, E_{polymer} was the energy of polymer and E_{LPS} was the energy of an isolated LPS molecule.

4.1.3 Results

Chitosan and XNBR molecules adsorbed with LPS molecules with DFT modeling and calculation results are shown in Figure 4.1.4. **Figure 4.1.5** presents the evaluation of compatibility for LSB using the changes of ratio of polymer in chitosan-XNBR. Before various actual evaluations, we estimate the chemical adsorption capacity of the prepared polymers for LPS (Li_2S_6) by computational expectation based on density-functional theory (DFT) (Figure 4.1.5a). Perfect

interaction with LPS by forming Li-O and Li-N bonds is verified and the strong adsorption energy of 1.22 eV (Li-N bonds for chitosan) and 0.92 eV (Li-N bonds for XNBR) are presented (detailed in **Figure 4.1.6**). Considering this results, the properties of affinity for LPS will be influenced by polar functional groups, like as high binding energy of chitosan. In the designed binder (chitosan-XNBR), the amounts of chitosan would play an important role in the regulation of LPS. Based on the computational expectation, UV-Vis spectroscopy was conducted in a 0.1 mM Li_2S_6 DOL-DME solution with 10 mg of the prepared polymer films to evaluate the adsorption capability of LPS (Figure 4.1.5b). An absorption region of 240–450 nm can be observed for the LPS solution. The two characteristic peaks centered at 260 and 280 nm are ascribed to S_6^{2-} species. After adding the prepared polymers into the Li_2S_6 solution, the color of the solution changed noticeably after 4 h. The color of the polymer- Li_2S_6 solution gradually changed from dark yellow to light yellow. Moreover, the peak intensities of the S_6^{2-} species decreased significantly after adding the polymer. In case of XNBR, it showed slightly decreased absorbance at 260 and 280 nm due to their functional groups of CN and COOH. The greatest decrease in absorbance at 260 and 280 nm was observed with chitosan and high amount of chitosan in chitosan-XNBR. These results clearly demonstrate that chitosan adsorbed LPS efficiently due to its abundant functional groups in glycosides and the content of chitosan in chitosan-XNBR is dominant in anchoring the LPS.

To confirm the mechanical properties of electrode according to prepared various polymers, nano-indentation was carried out under a force of 500 μN , and for increased precision, the process was repeated 5 times at 10 different sites (Figure 4.1.5c). The reduced modulus and elastic recovery parameter were calculated from

the load-displacement curves by the Oliver–Pharr method. Overall, electrodes with chitosan-XNBR polymers presented robust mechanical properties due to their intermolecular bonding (covalent bonding and hydrogen bonding). Increasing the content of chitosan in chitosan-XNBR presented the improved mechanical properties because of the strong mechanical properties of chitosan. On the other hand, increasing the content of XNBR displayed relatively ductile due to the elastic properties of XNBR. Among the various ratio of chitosan-XNBR polymer, X1C3 presented the most improved mechanical properties, which would lead to the effective control of volume changes of sulfur and low degradation of capacity of battery in cycling.

As well as LPS affinity and mechanical properties, ionic conductivity is also important factor to design the binder of LSB. Through the electrochemical impedance spectroscopy, prepared polymer films are evaluated the ionic conductivity. Like as high ionic conductivity of polysaccharides, chitosan presented high ionic conductivity ($8.17 \times 10^{-6} \text{ S cm}^{-1}$) and chitosan-XNBR films showed improved ionic conductivity according to the contents of chitosan. (detailed in **Figure 4.1.7**) Considering the various evaluations about prepared polymer shown in Figures 4.1.2 and 4.1.7, Li-S cell with X1C3 polymer binder is expected to show the most improved battery performance even at high C-rates (as shown in Figure 4.1.5d).

Figure 4.1.8a shows the results of the battery performance tests performed using the prepared binders (amounts of binder in cathode; 5 wt. %). The Li–S cell with chitosan and XNBR binder showed an initial specific capacity of 1190 and 1069 mAh g⁻¹ at 0.2 C, and a specific capacity of 581 and 445 mAh g⁻¹ after 50 cycles, respectively. According to the increasing the chitosan contents in chitosan-XNBR

binder, the specific capacity is remarkably enhanced (After 50 cycles at 0.2C, Li-S cell with X3C1 binder; 657 mAh g⁻¹, with X1C1 binder; 848 mAh g⁻¹, and with X1C3 binder; 1054 mAh g⁻¹). The improved battery performance of Li-S cell with X1C3 binder was attributed by their robust mechanical properties and high affinity to LPS and it meant that this system can maintain mechanical and electrochemical stability.

In order to examine the electrochemical characteristics according to the amount of the binder, the cathode was prepared by adjusting the amount to 3, 5, and 10 wt. % of binder. In the preparation of cathode with less than 5 wt. % the binder, the active material was not properly attached to the current collector when chitosan or XNBR binder was used (there are not changed loading mass after drying). However, in case of X1C3 binder, it presented well-loading on the current collector. Based on the well-properties of X1C3 binder, prepared Li-S cells with different amount of X1C3 binder (3, 5, and 10 wt. %) are evaluated by cyclic voltammetry (1.7 – 2.8 V vs. Li/Li⁺, at 0.1 mV s⁻¹) and galvanostatic charge-discharge test at 0.2 C for 100 cycles (Figure 4.1.8b-4.1.8c). In the graphs of cyclic voltammetry about Li-S cell with 3, 5, and 10% of X1C3 binder, the increased redox current density peaks and low voltage difference in Li-S cell with 3 wt. % binder was observed and it meant that the Li-S cell with low amount of binder provided the efficient electrochemical system (**Figure 4.1.9**). Based on this result, the prepared Li-S cell showed outstanding performance despite using a small amount of a polymer binder of 3 wt. % (Initial specific capacity; 1560 mAh g⁻¹ at 0.05C and 947 mAh g⁻¹ after 100 cycles at 0.2C). However, in the Li-S cell with 10 wt.% X1C3 binder, the battery performance was decreased to 748 mAhg⁻¹ of specific capacity after 100 cycles at 0.2C. As previously mentioned, a large amount of polymer can decrease the

efficiency of electrochemical system, so it is ideal to use a small amount of binder. This excellent performance comes from the efficient electrochemical system by low amount of binder, as well as the improved mechanical properties of the X1C3. This result can be predicted to not only operate an efficient electrochemical system with only 3% of the binder, but also to perform stable cycling.

4.1.4 Conclusions

In summary, the lean tough binder for durable LSB at high rate was designed through the combination of chitosan and XNBR in aqueous system. The chitosan-XNBR binder provided the robust mechanical strength and highly regulation of LPS despite of its extreme small amount in cathode. Moreover, decreased the content of the binder improved the overall energy density and enabling facile ion/electron transport to implement an efficient electrochemical system. Prepared Li-S cell using 3 wt. % optimal binder presented stable battery performance for 500 cycles at high rate of 5 C and it achieved superior capacitive performance, even at an ultrahigh rate of 20 C. Our designed binders will provide a new strategy for next generation energy storage that requires fast charging and high-power delivery.

4.1.5 Acknowledgement

This work was supported by the Basic Science Research Program through the National Research Foundation of Korea (NRF) funded by the Ministry of Science and ICT (NRF-2019R1A2C1003594 and NRF-2019R1A2C1003551) and the Ministry of Education (NRF-2020R1A6A3A13074137).

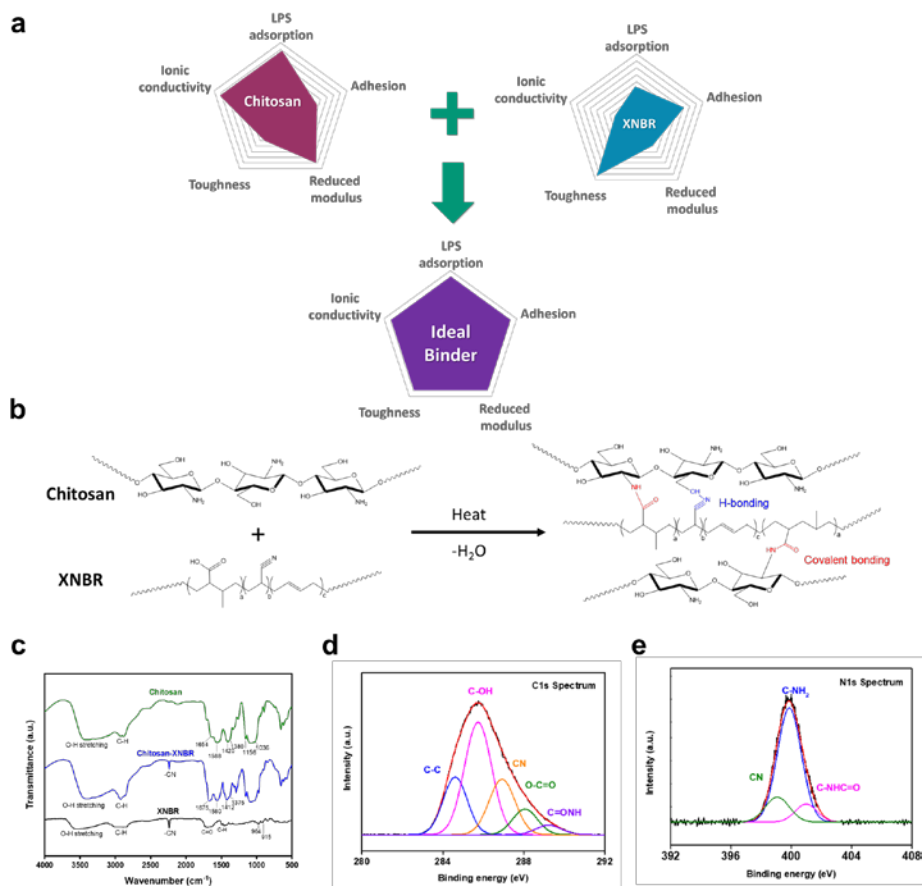


Figure 4.1.1 (a) Schematic expression of modulating binder, (b) formation of intramolecular bond between chitosan and XNBR (c) Characterization of chitosan, chitosan-XNBR, and XNBR by FT-IR, (d) XPS C1s core-level spectra and (e) N1s core-level spectra of chitosan-XNBR.

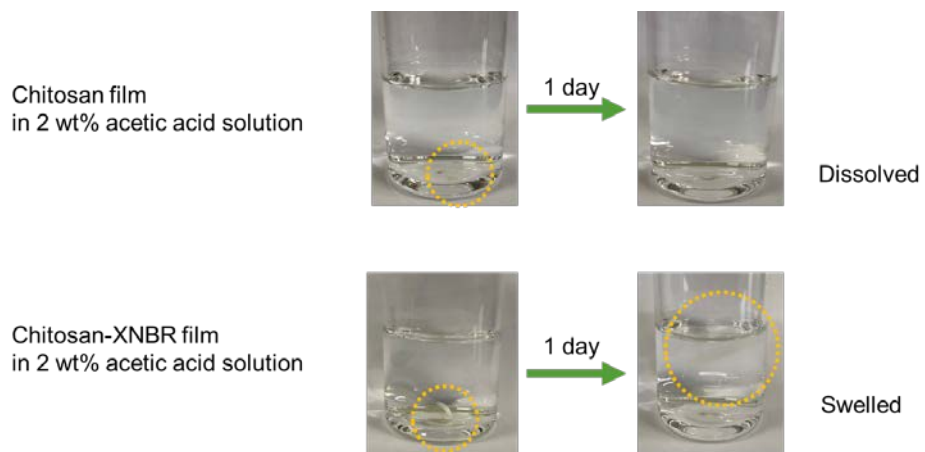


Figure 4.1.2 Solubility test in acetic acid of prepared polymer films

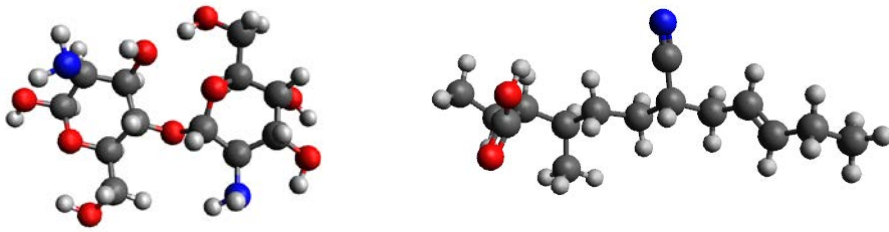


Figure 4.1.3 DFT modeling for chitosan and XNBR molecules.

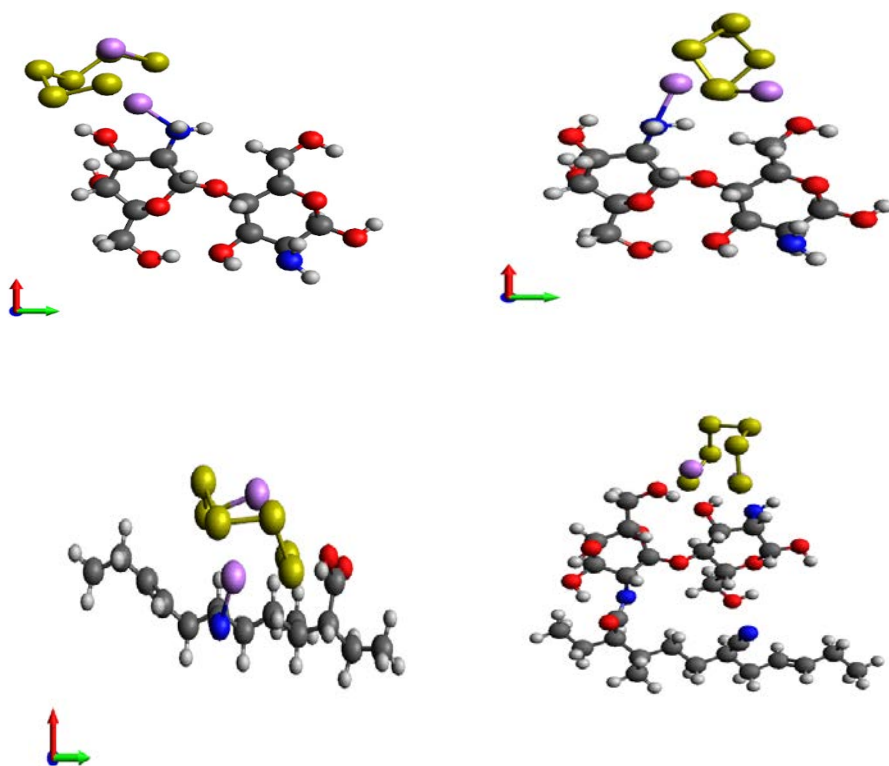


Figure 4.1.4 DFT modeling for chitosan and XNBR molecules adsorbed with Li_2S_6 molecules.

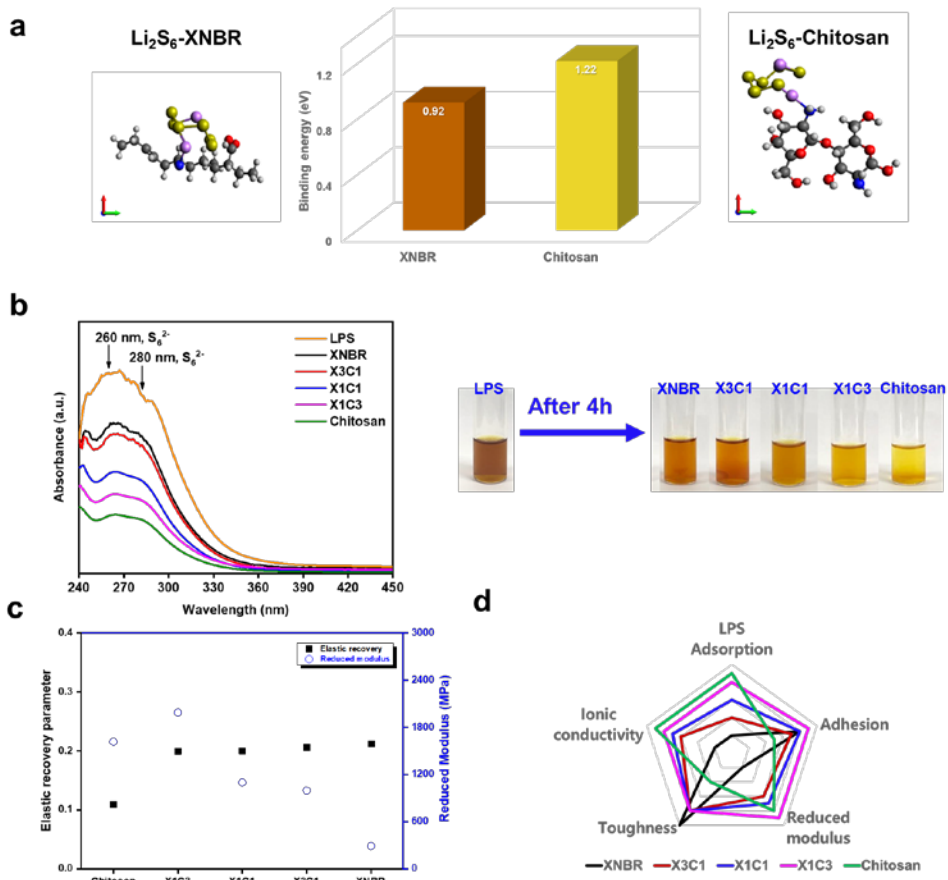
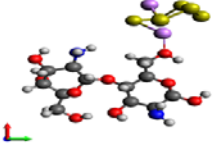
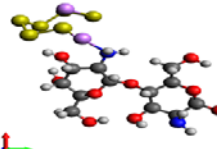


Figure 4.1.5 (a) computational calculation of polymer-LPS(Li_2S_6) binding energy using density-functional theory, (b) UV-Vis spectra of Li_2S_6 and various polymer films according to ratio of chitosan and XNBR (right; optical images), (c) Average reduced moduli and elastic recovery parameter of electrode with prepared various binders determined *via* nanoindentation, and (d) Evaluation chart of prepared binders for Li-S battery

Li₂S₆-Chitosan

| Binding site | Final state | E _{ad} (eV) |
|----------------------|---|----------------------|
| Monodentate (O-site) |  | -0.8282 |
| Monodentate (N-site) |  | -1.2219 |

Li₂S₆-XNBR

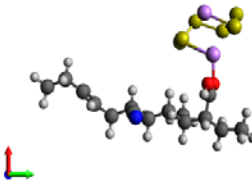
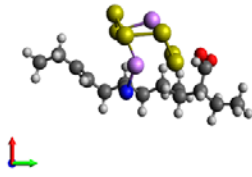
| Binding site | Final state | E _{ad} (eV) |
|----------------------|---|----------------------|
| Monodentate (O-site) |  | -0.9047 |
| Monodentate (N-site) |  | -0.9275 |

Figure 4.1.6 Computational calculation of polymer-LPS(Li₂S₆) binding energy using density-functional theory

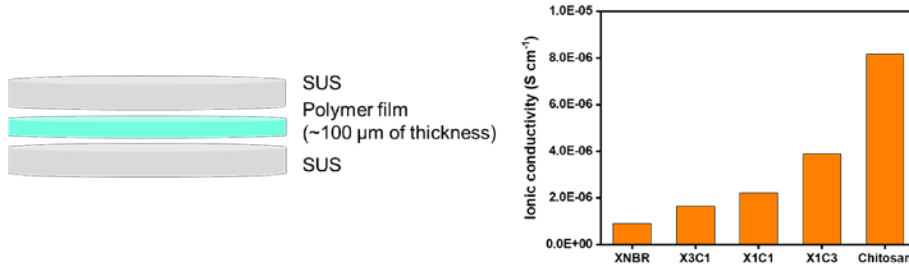


Figure 4.1.7 Ionic conductivity of prepared polymer films at 25 °C from EIS (electrochemical impedance spectroscopy).

Each polymer film was sandwiched between a stainless steel (SS) disc ($d = 1.6 \text{ cm}$) in the 2032 type coin cell. The cell was sealed to prevent contamination from oxygen, moisture, and other substances in glove box under Ar atmosphere. The ionic conductivity was calculated from the electrolyte resistance (R_s) obtained from the intercept of the AC impedance spectra with the real axis, the film thickness (l , ~100 μm), and the electrode area (A , 2 cm²) by the equation 1.

$$\sigma (\text{Ionic conductivity}) = \frac{l}{R_s \times A} \dots\dots\dots (\text{Equation 1})$$

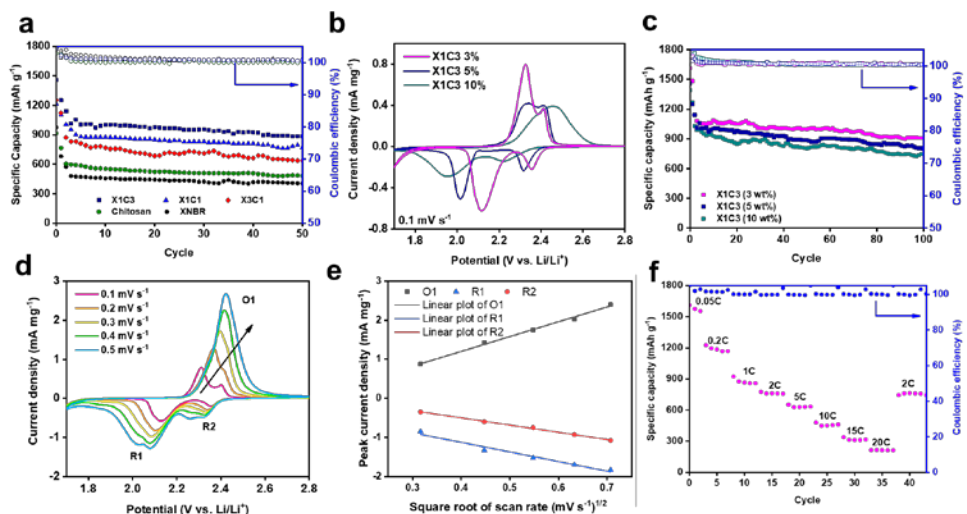


Figure 4.1.8 (a) discharging specific capacities of the Li-S cells at a rate of 0.2 C, (b) cyclic voltammetry of Li-S cell with various amount of X1C3 binder, (c) discharging specific capacities of the Li-S cells according to the contents of X1C3 binder at a rate of 0.2 C, (d) cyclic voltammetry of Li-S cell with 3 wt.% X1C3 binder at 0.1-0.5 mV s^{-1} , (e) Linear relationship of redox peak current from Figure 3(d), and (f) rate capability test of the Li-S cell with 3 wt.% X1C3 binder at 0.05, 0.2, 1, 2, 5, 10, 15, and 20 C.

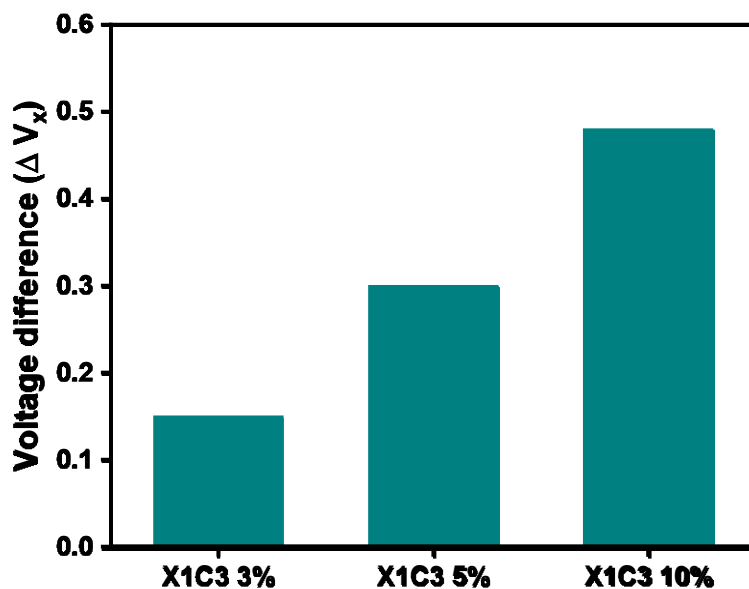


Figure 4.1.9 The voltage difference between the charge and discharge plateau of prepared Li-S cells

The voltage difference (ΔV_x) between the charge and discharge plateau shows the polarization and roundtrip energy efficiency of cell. Lower polarization (lower voltage difference) represents a more kinetically efficient reaction process with smaller barrier.

4.2. Multifunctional Ga₂O₃ shield for Li-S batteries

4.2.1 Introduction

Rechargeable lithium–sulfur batteries are emerging as promising energy storage systems due to their low cost and the high energy density of sulfur cathodes. The successful development of such batteries is expected to transform fossil fuels into renewable energy, thus paving a new way to realize an effective energy system in the long run. However, several factors limit the practical application of lithium–sulfur batteries such as safety and stability issues including the rapid degradation of battery life and unexpected accident. In our work, we introduced a multifunctional gallium oxide shield as an interlayer to regulate the shuttling effect of polysulfide in the sulfur cathode as well as to suppress Li-dendrite growth in Li-anode. This work presents appealing and competitive lithium–sulfur batteries with great potential for stationary storage applications.

4.2.2 Model and computational method

Figure 4.2.1a presents the schematic expression of the multifunctional

Ga₂O₃ shield, which can suppress the LPS shuttle effects in the cathode, and regulate Li-dendrite growth in the anode, thus, leading to an ultra-stable long-term cycling of LSB. The TEM images of the Ga₂O₃ nanoplates (Fig. 4.2.1b) prepared from Ga metal by sonication and mechanical ball-milling-assisted method,²² confirmed their structure and size of approximately 60 × 100 (±20) nm. The XRD pattern of the crystal phase of the as-prepared Ga₂O₃, is shown in Fig. 4.2.1c. As shown in Fig. 4.2.1c, a typical peak corresponding to β-Ga₂O₃ was observed in the XRD spectra of Ga₂O₃. In addition, no peaks corresponding to the presence of impurities were observed due to the origin of the Ga metal. In the XPS spectra of the as-prepared Ga₂O₃ as shown in Fig. 4.2.1d and Fig. 4.2.2, the peak observed at the binding energy of 532.1 eV can be attributed to the valence state O 1s in Ga₂O₃.²²

To estimate the chemical adsorption capacity of LPS (Li₂S₄, Li₂S₆, and Li₂S₈) by Ga₂O₃, LPS adsorbed on the Ga₂O₃ was studied using density functional theory (DFT) calculations, which was performed using the Vienna ab-initio simulations package (VASP). [1,2] The projector augmented wave (PAW) pseudopotential and the generalized gradient approximation (GGA) exchange-correlation function described by Perdew–Burke–Ernzerhof (PBE) was adopted. [1,2] To guarantee convergence, the energy tolerance and force tolerance were set to 10⁻⁵ and 0.05 eV/Å, respectively. The cut-off energy of the plane-wave basis was 400 eV. To evaluate the long-range effects, adsorption energies were calculated using the DFT-D3 method with Becke-Jonson damping, wherein, the van der Waals interaction (vdW) was considered. [3] The vacuum over z-direction were set to exceeds 20 Å, and the nearest distance between LPS and its images were kept over 10 Å to avoid periodic image interactions. The binding energy of LPS and metal oxides (E_{ad}) was

defined as: $E_{\text{ad}}(\text{eV}) = E_{\text{MO+LPS}} - (E_{\text{MO}} + E_{\text{LPS}})$ where $E_{\text{MO+LPS}}$ is the total energy of the metal oxide with LPS, E_{MO} is the energy of the metal oxide, and E_{LPS} is the energy of an isolated LPS molecule. Additionally, adsorption energy between well-known metal oxides and LPS were calculated for comparison (detailed in Figure 4.2.3).

4.2.3 Results

The adsorption capability of Ga_2O_3 to LPS was investigated by predicting the interaction of the as-prepared Ga_2O_3 with LPS using DFT calculations, actual adsorption evaluation with LPS by UV-Vis spectroscopy, and confirmation of the chemical bonding states of Ga_2O_3 by XPS after LPS adsorption in Fig. 4.2.4.

To investigate the interaction between Ga_2O_3 , Al_2O_3 , and Li_2S_n (LPS, $n=4, 6$ and 8), the first-principles calculation method using DFT was employed to calculate the adsorption energy. The bond structure diagrams of the optimized chemisorption configurations are demonstrated in Fig. 4.2.5. The electron-rich S in Li_2S_n prefers to bind with positively charged Ga, while the Li^+ tends to bond with electron-rich O. The adsorption energies for Li_2S_4 , Li_2S_6 , and Li_2S_8 were -7.44 , -7.38 , and -7.67 eV, respectively. Ga_2O_3 displayed a powerful interaction to LPS. These results indicate that Ga_2O_3 thermodynamically modulates more favorable bond interactions and chemical anchoring toward LPS than previously reported metal oxides. From the computational prediction, the actual evaluation of the adsorption capability of Ga_2O_3 was conducted by UV-Vis spectroscopy in a 0.5 mM Li_2S_6

DOL/DME solution using 10 mg of the Ga₂O₃. An absorption region of 200–500 nm was observed for the LPS solution. In addition, three characteristic peaks centered at 260, 280, and 340 nm were observed, which were ascribed to the S₆²⁻ species.^{24,25} After the addition of the Ga₂O₃ into the Li₂S₆ solution, a noticeable change in color was observed after 6 h (Fig. 4.2.4b (inset)). The color of the Ga₂O₃–Li₂S₆ solution gradually changed from dark yellow to light yellow. In addition, the peak intensities of the S₆²⁻ species decreased significantly after the addition of the Ga₂O₃. These results clearly demonstrate the efficient adsorption of LPS by Ga₂O₃ due to its favorable bond interactions and chemical anchoring toward LPS. After the LPS adsorption, a newly emerging peak at 20.56 eV was observed in the Ga 3d XPS spectra, which corresponds to the binding energy of Ga-S environment.²⁶ In addition, a characteristic peak at 167.2 eV was observed in the S 2p XPS spectra, which corresponds to the thiosulfate species generated by the surface adsorption reaction between the LPS and the Ga₂O₃. Furthermore, the peak observed at 168.6 eV was assigned to the polythiosulfate species that resulted from the further reaction between the LPS and thiosulfate species.²⁷ It can be demonstrated as shown in Fig. 4.2.2e according to the suggestions provided by Nazar's group.²⁸ The long-chain LPSs can be converted to thiosulfate and polythiosulfate species by metal-based catalysts, thus, confirming the interfacial catalytic reaction at the surface of the Ga₂O₃ interlayer.^{28,29} In addition, the formation of O–Li bonding configuration was observed at 532.9 eV in the O 1s core-level XPS spectra after LPS adsorption.³⁰ These results indicate the efficient adsorption of LPS by Ga₂O₃, which can be attributed to the strong affinity of Ga₂O₃ to LPS, and thiosulfate–polythiosulfate conversion.

Figure 4.2.6 shows the application of the Ga₂O₃ shield as an interlayer and the

characterization of its effects on the Li-metal anode and sulfur cathode. Generally, Ga₂O₃ materials are known as good ion-conductive materials compared to Al₂O₃ materials, which are commonly used in industries. To characterize the interfacial behaviors and Li-ion diffusivity of the prepared interlayers (CB; interlayer with carbon black and GX; interlayer with X wt. % of Ga₂O₃), each prepared interlayer was sandwiched between two stainless-steel disks in the 2032 coin-type cell, and the ionic conductivity of the interlayers was confirmed through EIS. For the CB interlayer, the 100% carbon black coating with no ionic conductivity acted as a physical trap, and might have interfered with the transport of lithium ions. In contrast, the ionic conductivity of the GX interlayer increased with an increase in the amount of Ga₂O₃ until $1.8 \times 10^{-5} \text{ S cm}^{-1}$ (G60). However, the ionic conductivity decreased when 100% Ga₂O₃ (G90) was coated. This can be seen from the SEM images in Fig. 4.2.6 (G60) and Fig. 4.2.7 (G90). This is because an excessive amount of Ga₂O₃ can block the transport of lithium ions due to their plate-like morphology. Therefore, an improved ionic conductivity is achieved when the proper amount of Ga₂O₃ is coated. The stability of the Li-metal anode during Li plating and stripping was evaluated using the G60 interlayer, which showed the most improved ionic conductivity. The tests were conducted at a high current density of 2 mA cm^{-2} (4 mAh cm^{-2}). As shown in Fig. 6C, the symmetric cell with the G60 interlayer showed a stable voltage plot for Li plating and stripping above 200 h, indicating a uniform Li-anode growth with stable solid electrolyte interphase, however, the cell with Celgard 2500 (PP) died with a big voltage change. Furthermore, as shown in Fig. 4.2.8, the Li-dendrite growth in the Li-metal anode with the G60 interlayer was regulated, however, the Li-metal anode with the PP separator showed drastic growth of Li-dendrites. These results indicate that the use

of the G60 interlayer in LSB can improve the long-term cycling stability of LSB, and effectively control the growth of Li-dendrite.

In Fig. 4.2.6d, the thermal stability of the as-prepared G60 interlayer was characterized via heat treatment (150 °C for 1 h). As shown in Fig. 4.2.6d, Ga₂O₃ has a high thermal stability, which is responsible for the high thermal stability of the interlayer. In addition, no shrinkage or deformation was observed in the interlayer, indicating that the G60 interlayer has a higher thermal resistance compared to the PP separator.

In addition to the previously evaluated LPS adsorption capacity of Ga₂O₃ (Fig. 4.2.4), the LPS blocking capacity of the as-prepared G60 interlayer was determined using a H-type cell with 5 mM Li₂S₆ DOL/DME solution. The results revealed that the G60 interlayer was well-blocked by the LPS, which is due to the enhanced LPS adsorption properties of Ga₂O₃ obtained from their various OV. These results indicate the effectiveness of Ga₂O₃ in producing a long-life ultra-stable LSBs.

Figure 4.2.9 compares the electrochemical characterizations of the full Li–S coin cell constructed with the G60 interlayer and that constructed with the PP separator (expressed as without (w/o) interlayer). Figure 4.2.9a shows the cycling performance of the as-prepared Li–S cells at 0.2 C. As shown in Fig. 4.2.9a, the Li–S cell with the G60 interlayer exhibited a superior battery performance with a high discharging capacity of 1245 mAh g⁻¹ after 50 cycles, which indicates a 400% increase in the specific capacity, compared to that of the Li–S cell without an interlayer. In addition, the specific capacity increased with an increase in the Ga₂O₃ content in the interlayer (specific capacity of the Li–S cells utilizing each of the listed interlayer after 50 cycles at 0.2 C: CB–420, G30–710, G45–1080, and G90–908 mA h g⁻¹). At the highest content (G90) of Ga₂O₃ in the interlayer, the initial

battery performance was similar to that of the Li–S cell with the G60 interlayer, however, a rapid capacity decay was observed due to the low ion transport of the densely coated Ga_2O_3 . Figure 4.2.9b and Fig. 4.2.10 present the initial galvanostatic charge–discharge profiles of the as-prepared Li–S cells at 0.2 C after activation at 0.05 C for 2 cycles. The Li–S cell with the G60 interlayer exhibited an enhanced specific capacity of 1368 mAh g^{-1} , which indicates a 400% increase in capacity compared to that of the Li–S cell constructed without an interlayer. In the profiles, the voltage difference (ΔV_x) observed between the charge and discharge plateaus indicates the polarization and roundtrip energy efficiency of the cell.^{24,28,31} Lower polarization (lower voltage difference) represents a more kinetically efficient reaction process with a smaller barrier.^{24,28,31} As shown in Fig. 4.2.11,

ΔV_x presented 173, 150, 145, 137, and 148 mV (w/o interlayer, with G30, G45, G60, and G90 interlayer, respectively). As shown in Fig. 4.2.11, the G60 interlayer, exhibited the most efficient reaction kinetics, thus leading to its high battery performance. Moreover, in the EIS analysis (detailed in Fig. 4.2.15), the as-prepared Li–S cell with the G60 interlayer presented a small increase in the electrolyte-, charge-transfer-, and interfacial contact resistance value after 50 cycles, compared to the Li–S cell without interlayer, which exhibited an increased resistance. Small increases of resistance in EIS represents the efficiency of the electrochemical system and the potential to extend the cycling life.

CV measurements were executed at different scan rates from 0.1 to 0.5 mV s^{-1} to explore the kinetics of Li^+ insertion/extraction and Li^+ diffusion rate in the battery, in which the Li–S cells with the G60 interlayer and without interlayer were assessed within a voltage window of 1.7–2.8 V vs. Li/Li^+ (Fig. 4.2.9c and Fig. 4.2.12). All the anodic and cathodic peak currents maintained a linear relationship

with the square root of the scan rates (Fig. 4.2.13). The Li^+ diffusion capability can be estimated using the classical Randles–Sevcik equation.³² According to the Randles–Sevcik equation, the relationship between the slopes of the curves and the corresponding Li^+ diffusion is a positive correlation. For the Li–S cell with the G60 interlayer, the slope-obtained oxidation peak currents (O1) increased by 120 % compared to that of the Li–S cell w/o interlayer. In addition, the slope-obtained reduction peak currents were enhanced by 253% (R1) and 106 % (R2) compared to that of the Li–S cell without an interlayer. The significant enhancement from using G60 interlayer in Li^+ diffusion kinetics may be ascribed to the provision of a more efficient electrochemical system from the dual-shielding effect of the regulation of the LPS shuttle effects and the suppression of Li-dendrite growth. To further analyze the battery performance of the fabricated Li–S cells, the Li–S cells were evaluated in terms of their rate capabilities with current densities ranging from 0.05 to 8 C. As shown in Fig. 4.2.9d, the average discharge capacities obtained for the Li–S cell constructed using the G60 interlayer showed a highly stable rate capabilities comparable to those of the Li–S cells prepared w/o interlayer. Moreover, the Li–S cell constructed using the G60 interlayer delivered a desirable battery performance at high C-rates (908 mAh g^{-1} at 2 C and 583 mAh g^{-1} at 8 C). The efficient electrochemical system of the as-prepared interlayer result in a high performance of the Li–S battery at a high C-rate. For commercial applications, a long-term cycling, and high loading density of sulfur at fast charging rates are important factors.^{6,31} Figure 4.2.4e shows the results of the long-term cycling test obtained for the Li–S cell prepared with the G60 interlayer operated at 2 C. The Li–S cell with the G60 interlayer exhibited an initial discharge capacity of 908 mAh g^{-1} at 2 C, at which most portable batteries are rated, and its capacity

remained at 613 mAh g⁻¹ after over 4,000 cycles (a capacity retention decay of 0.010% per cycle). To the best of our knowledge, this is the first time such outstanding ultra-stable long-term cycling effect of a metal oxide interlayer system is reported (shown in Fig. 4.2.14 and Table 4.2.1), and we believe this will accelerate the commercialization of LSBs. In addition, no increase was observed in the resistance of the Li–S cell with the G60 interlayer after 4,000 cycles, and the G60 interlayer also maintained their morphologies without critical collapse, as shown in Fig. 4.2.15.

An increased sulfur loading is important for the commercial application of LSBs. For example, the batteries used in electric vehicles require a sulfur loading of >2.0 mg cm⁻² for a specific energy density of >400 Wh kg⁻¹.³³ Thus, the specific capacity of the Li–S cell prepared with the G60 interlayer was evaluated as a function of the sulfur loading (2.1, 4.3, and 6.1 mg cm⁻²) at 2 C for 100 cycles. Figure S12 shows that the Li–S cell maintained its stability with an increase in sulfur loading, and its Coulombic efficiency reached ~99%. The multifunctional shielding of the Ga₂O₃ interlayer result in long-term cycling stability, with high rate and a high sulfur loading due to their multifunctional shielding. These results indicate the promising potential of Ga₂O₃ interlayer for the production of LSB, as well as multivalent ion batteries such as sodium–sulfur and potassium–sulfur batteries, which suffer from the shuttling effects of intermediates and dendrite growth in the metal anode.

4.2.4 Conclusions

In summary, Ga₂O₃ was introduced as a multifunctional shield for ultra-stable and long-life LSBs for the first time. The shield as an interlayer provides an efficient electrochemical system by highly suppressing the LPS shuttle effects. In addition, the various OV in Ga₂O₃ not only enhances LPS adsorption, but also greatly improves the catalytic ability and ionic conductivities. Additionally, the shield presents stable Li plating and stripping through the suppression of Li-dendrites growth. The multifunctional shielding of Ga₂O₃ interlayer in Li-S batteries remarkably improves the cycling performance with a low capacity retention decay of 0.010 % after 4,000 cycles at a high charging/discharging rate (2 C). Moreover, the high performance of Ga₂O₃ presents stable cycling performance at high sulfur loading (6.1 mg cm⁻²). We believe that the fabricated Ga₂O₃ shield will provide insights for a facile, scalable, and controllable approach for the fabrication of commercially viable LSBs with assistance of high technologies such as atomic layer deposition and nano-patterning.

4.2.5 Acknowledgement

This work was supported by the Basic Science Research Program through the National Research Foundation of Korea (NRF) funded by the Ministry of Science and ICT (NRF-2019R1A2C1003594) and the Ministry of Education (NRF-2020R1A6A3A13074137).

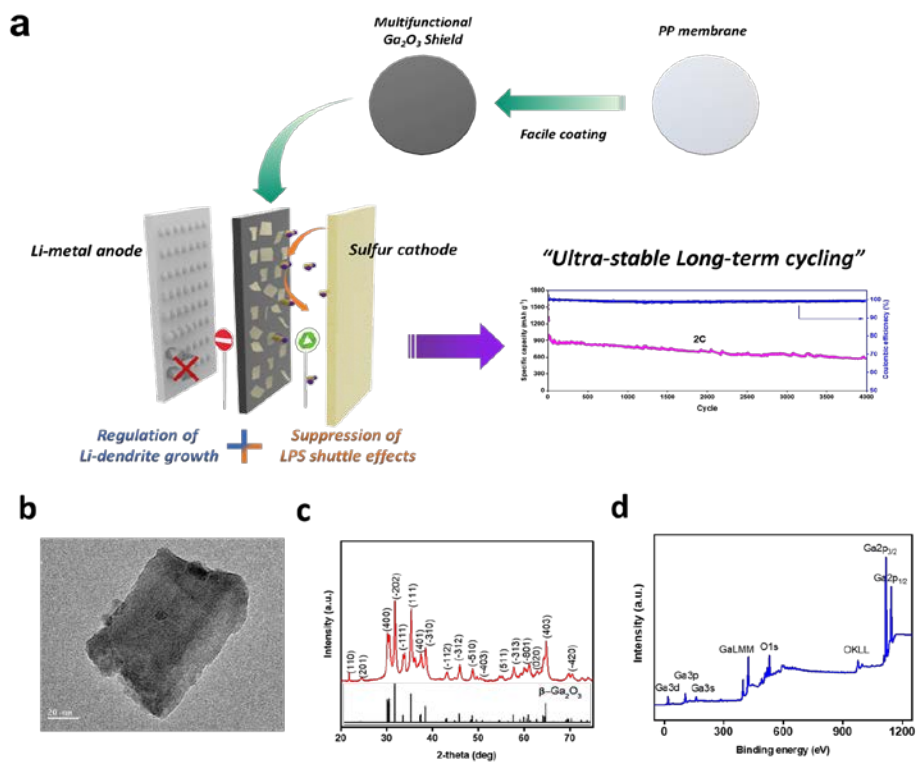


Figure 4.2.1 (a) Schematic expression of the multifunctional Ga_2O_3 shield in LSBs, (b) TEM images of the as-prepared Ga_2O_3 , (c) XRD pattern of the as-prepared Ga_2O_3 , and (d) XPS spectra of the as-prepared Ga_2O_3 .

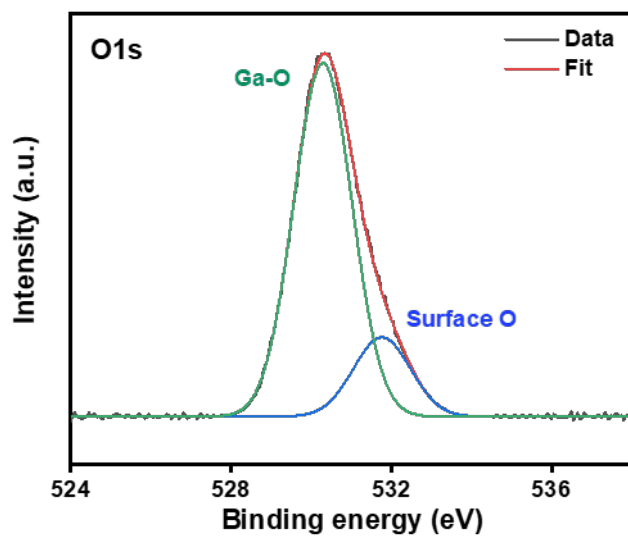


Figure 4.2.2 XPS spectra of pristine Ga₂O₃ at O 1s core level

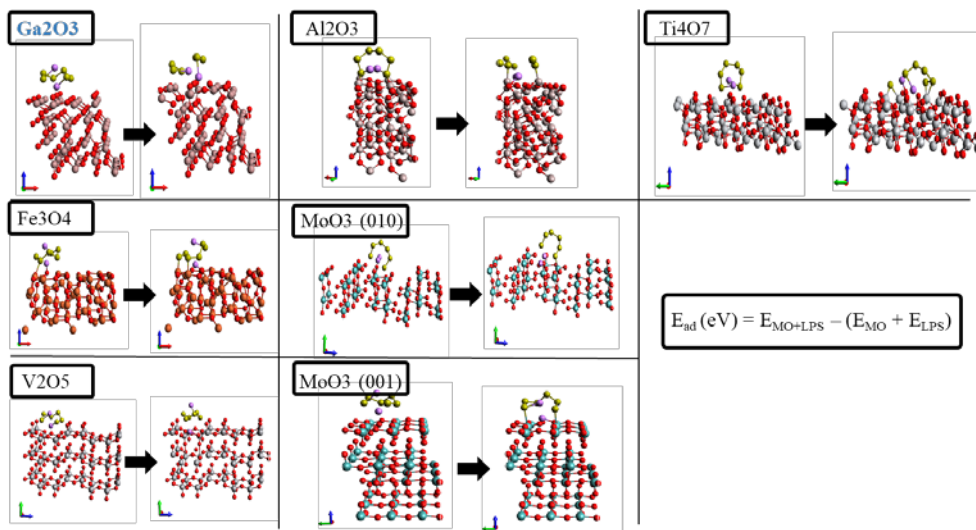


Figure 4.2.3 Computational calculation of interaction between various metal oxides (Ga₂O₃, Al₂O₃, Ti₄O₇, Fe₃O₄, MoO₃ (010), MoO₃ (001), and V₂O₅).

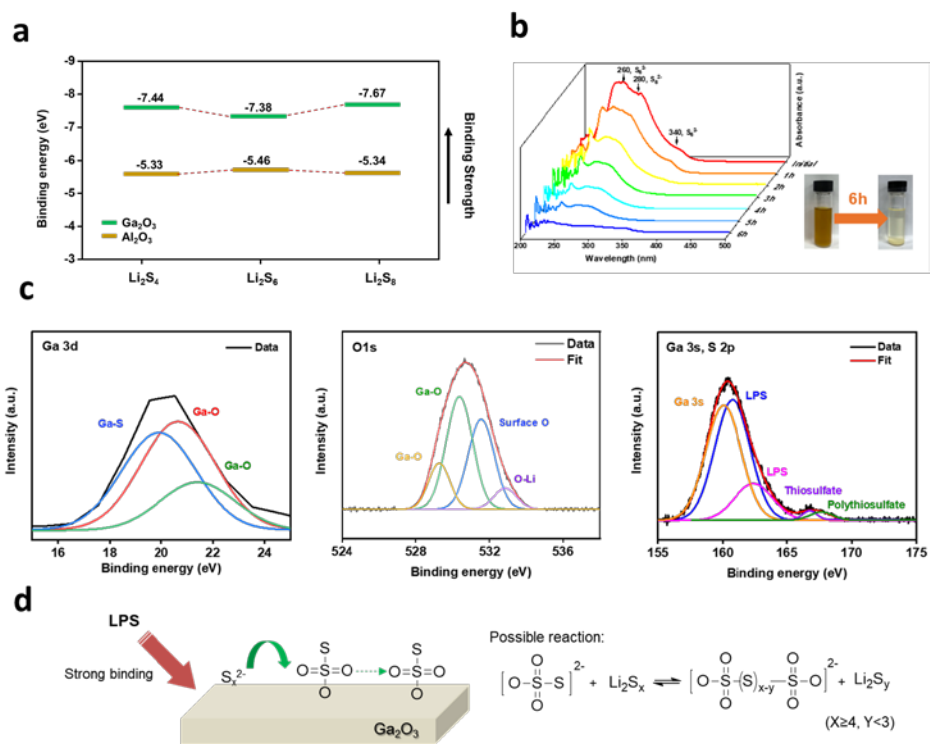
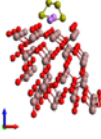
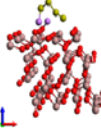
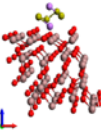
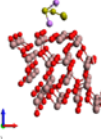
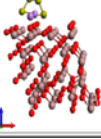
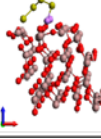
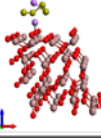
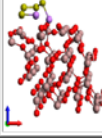
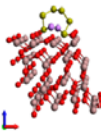
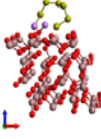
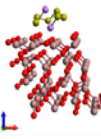
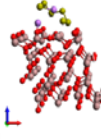
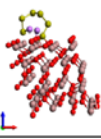
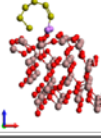
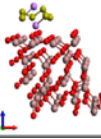
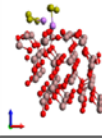


Figure 4.2.4 (a) DFT calculation results of the interaction between Ga₂O₃, Al₂O₃, and LPS, (b) UV-Vis spectra of Ga₂O₃ in LPS solution for 6 h and optical image (inset), (c) XPS spectra of Ga₂O₃ after adsorption in LPS solution, and (d) Schematic expression of the oxidation of the initially formed polysulfides by Ga₂O₃ to form thiosulfate on the surface.

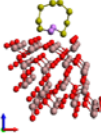
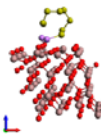
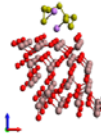
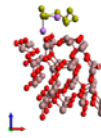
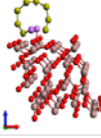
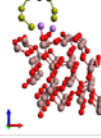
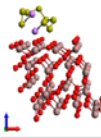
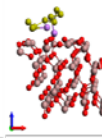
• $\text{Ga}_2\text{O}_3 + \text{Li}_2\text{S}_4$

| Sample number | Initial state | Final state | E _{ad} (eV) | Sample number | Initial state | Final state | E _{ad} (eV) |
|---------------|---|---|----------------------|---------------|---|--|----------------------|
| 1 |  |  | -4.52948 | 3 |  |  | -4.87177 |
| 2 |  |  | -7.44366 | 4 |  |  | -7.14249 |

• $\text{Ga}_2\text{O}_3 + \text{Li}_2\text{S}_6$

| Sample number | Initial state | Final state | E _{ad} (eV) | Sample number | Initial state | Final state | E _{ad} (eV) |
|---------------|--|--|----------------------|---------------|--|---|----------------------|
| 1 |  |  | -4.49718 | 3 |  |  | -4.41454 |
| 2 |  |  | -6.99074 | 4 |  |  | -7.38462 |

• $\text{Ga}_2\text{O}_3 + \text{Li}_2\text{S}_8$

| Sample number | Initial state | Final state | E _{ad} (eV) | Sample number | Initial state | Final state | E _{ad} (eV) |
|---------------|---|---|----------------------|---------------|---|--|----------------------|
| 1 |  |  | -4.72015 | 3 |  |  | -5.79772 |
| 2 |  |  | -7.03833 | 4 |  |  | -7.67219 |

14

Figure 4.2.5 Computational calculation of interaction between Ga_2O_3 and Li_2S_n (n=4, 6, and 8)

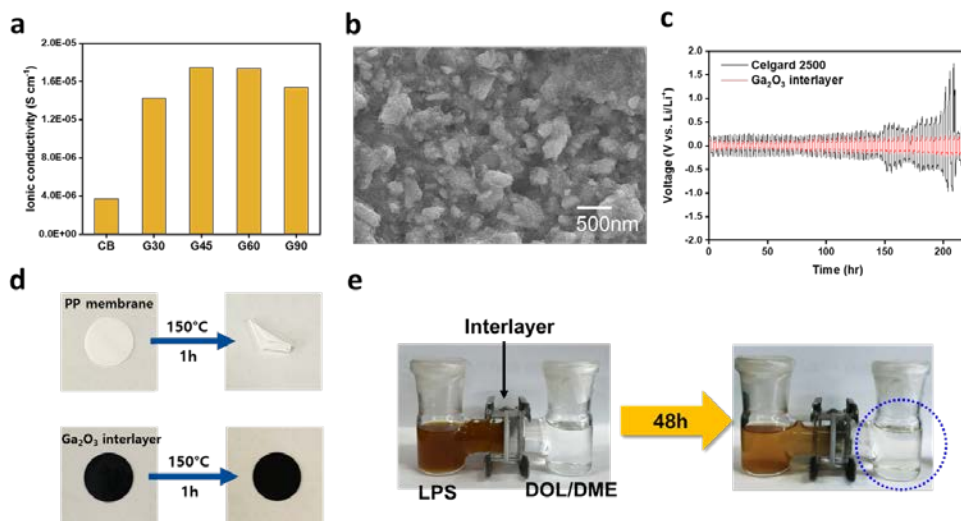


Figure 4.2.6 (a) Ionic conductivity with various contents of Ga₂O₃ evaluated by EIS, (b) SEM images of Ga₂O₃ shield (surface, scale bar; 500 nm), (c) Voltage profiles of lithium symmetric cells with Celgard 2500 (PP) and Ga₂O₃ shield as separators at a current density of 2 mA cm⁻² (4 mAh cm⁻²), (d) optical images of the PP separator and the as-prepared Ga₂O₃ shield after heating at 150 °C for 1 h, and (e) optical image of the diffusion of LPS: H-type cell with the as-prepared Ga₂O₃ shield after 48 h.

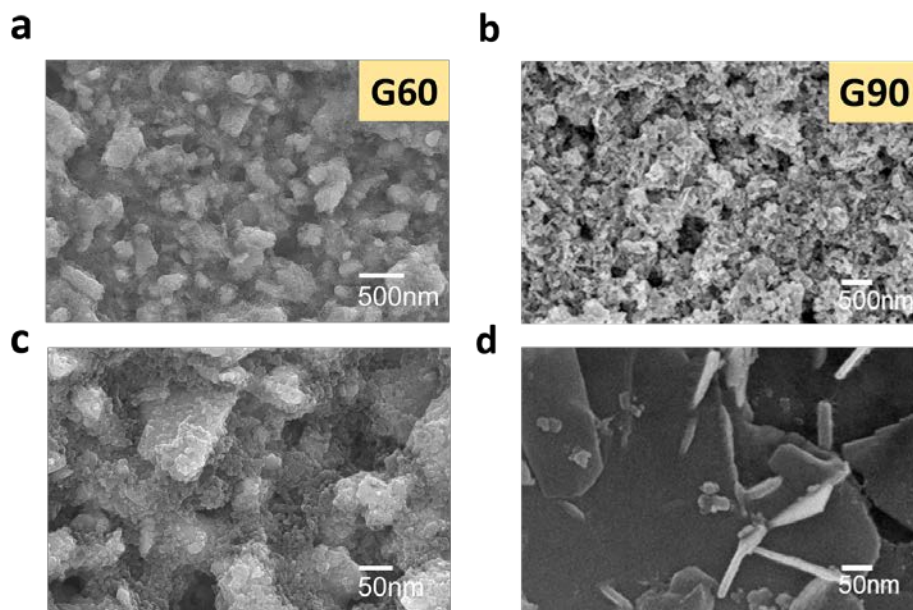


Figure 4.2.7 SEM images of prepared G60 interlayer (a), (c) and G90 interlayer (b), (d) (surface, scale bar; 500 nm and 50 nm).

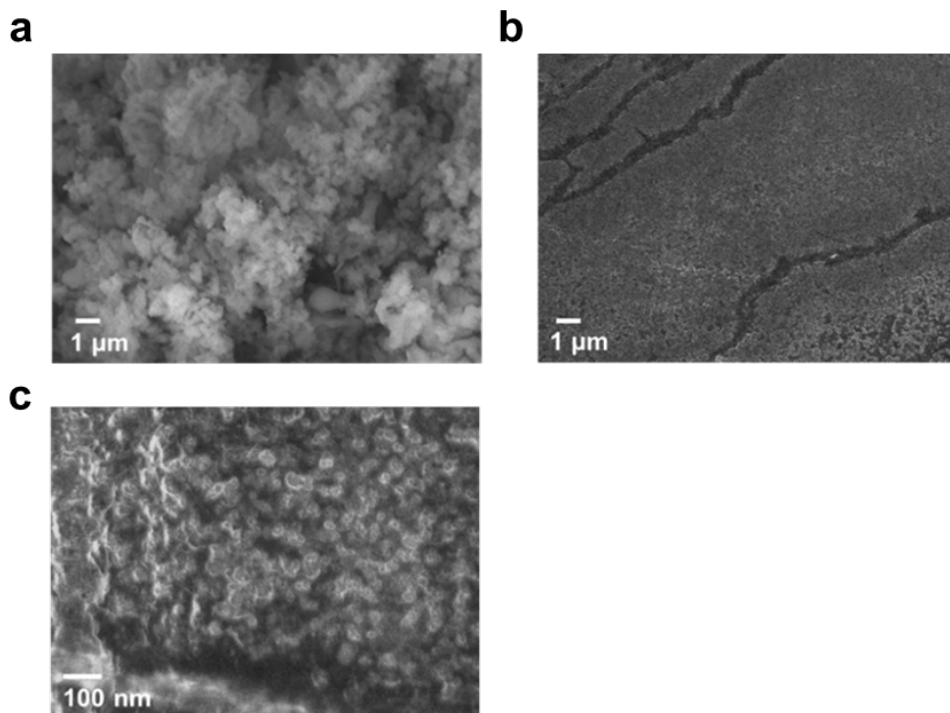


Figure 4.2.8 SEM images of Li-metal surface after Li symmetric cell test (Fig. 3c); (a) Li metal with Celgard 2500 (PP membrane), (b) Li-metal with G60 interlayer, and (c) magnification of (b).

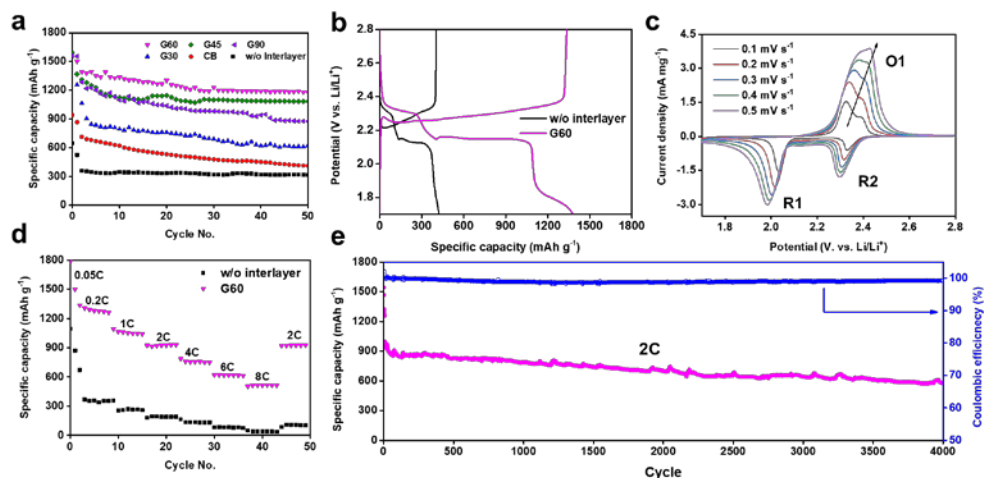


Figure 4.2.9 (a) Discharging specific capacities of the as-prepared Li-S cells at a rate of 0.2 C, (b) Galvanostatic charge-discharge profiles of the Li-S cells without interlayer, and with the G60 interlayer at the initial cycle (0.2 C) (c) CV profiles of the Li-S cells with the G60 interlayer according to various scan rates, (d) Rate capability test of the Li-S cells without interlayer and with the G60 interlayer at 0.2 to 8 C, and (e) Long-term cycling of the as-prepared Li-S cells with the G60 interlayer at 2 C for 4,000 cycles.

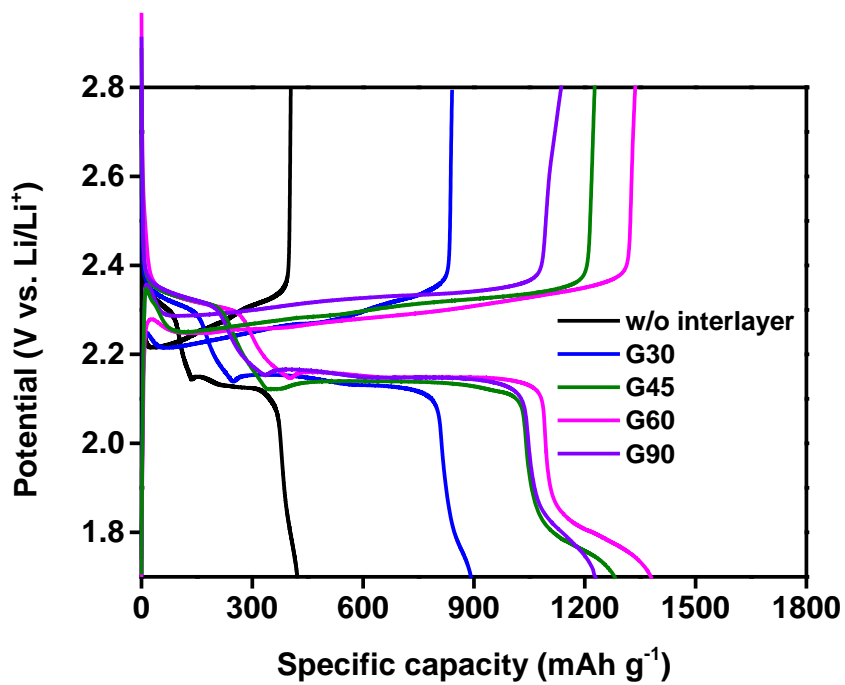


Figure 4.2.10 Galvanostatic charge-discharge profiles of prepared LSBs at the initial cycle of 0.2C.

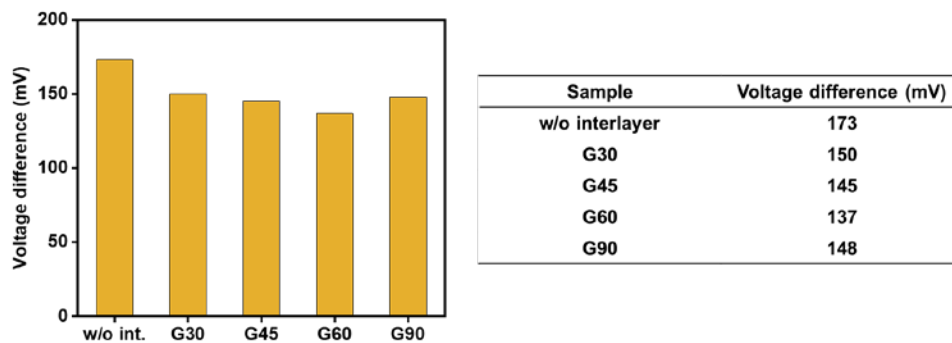


Figure 4.2.11 Voltage difference of prepared LSBs obtained from galvanostatic charge-discharge profiles and its results.

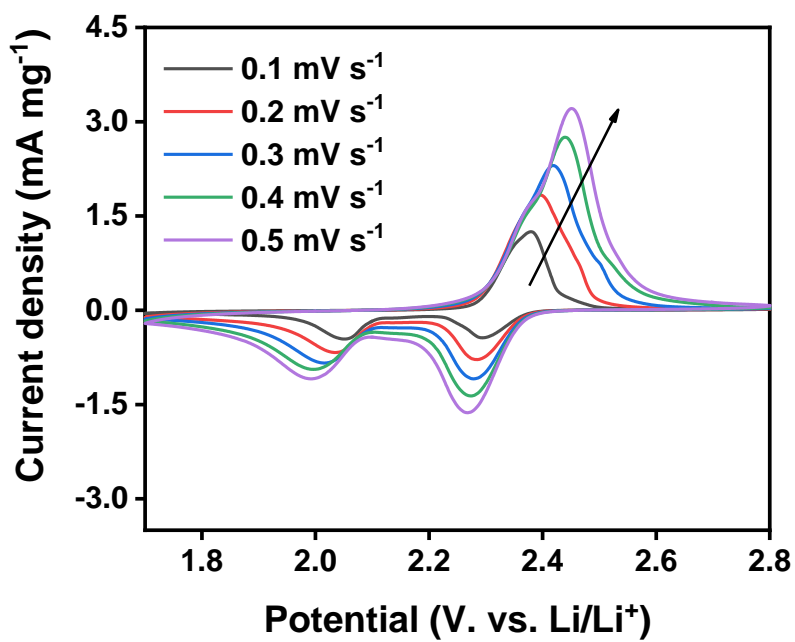


Figure 4.2.12 Cyclic voltammetry of prepared Li-S cell without interlayer (PE separator) according to various scan rates.

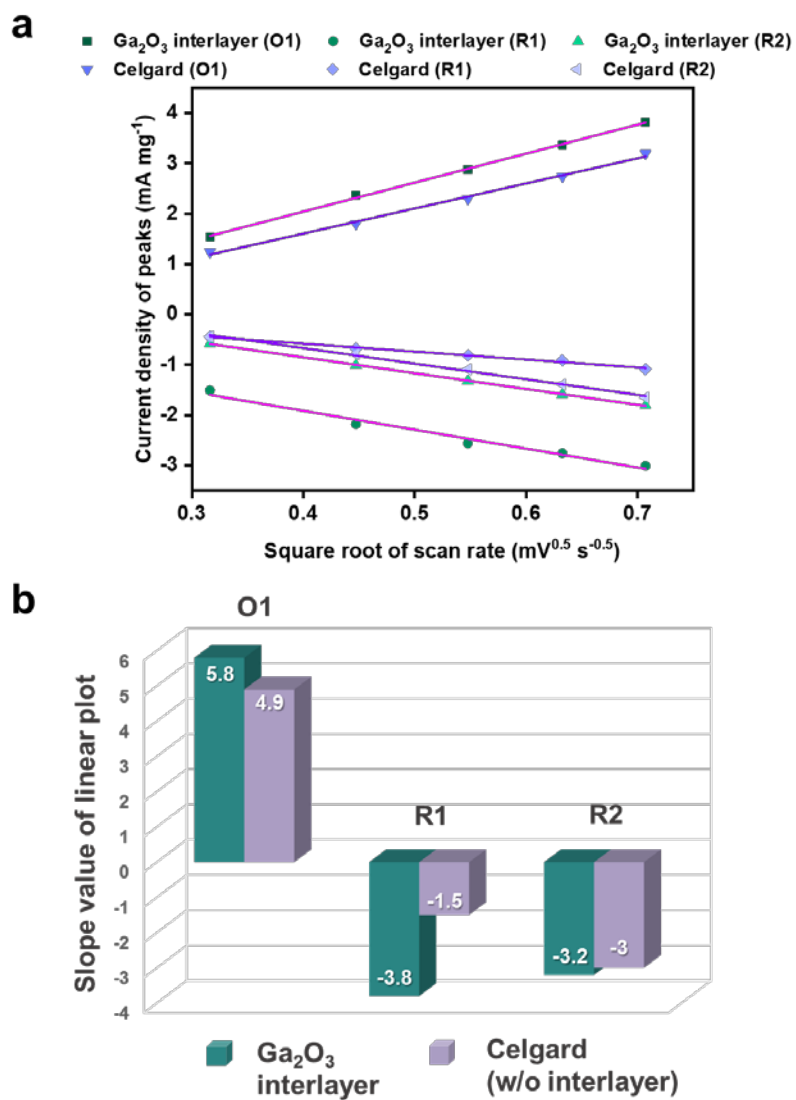


Figure 4.2.13 (a) The relationships between current density of redox peaks and square root of scan rate about prepared Li-S cells (without interlayer and with G60 interlayer) and (b) its detailed slope values.

Periodic Table of Metal Oxide-based Interlayer for Li-S Batteries

| Li | Be | Element | | | | | | | | | | B | C | N | O |
|----|------------------------------|--|---|---|--|---|---|----|-----------------------------|----|------------------------------|---|--|----|----|
| Na | Mg MgO (100) (0.29) | Metal oxide (Cycle) (Capacity decay retention per cycle) | | | | | | | | | | Al Al ₂ O ₃ (450) (0.1) | Si SiO ₂ (200) (0.05) | P | S |
| K | Ca CaO (250) (0.11) | Sc | Ti Ti ₂ O ₃ (2500) (0.030) | V V ₂ O ₅ (600) (0.057) | Cr | Mn MnO ₂ (500) (0.07) | Fe Fe ₂ O ₃ (2000) (0.024) | Co | Ni NiO (100) (0.4) | Cu | Zn ZnO (100) (0.51) | Ga Ga ₂ O ₃ (4000) (0.013) | Ge | As | Se |
| Rb | Sr | Y Y ₂ O ₃ (200) (0.112) | Zr ZrO ₂ (500) (0.069) | Nb | Mo MoO ₃ (500) (0.120) | Tc | Ru RuO ₂ (300) (0.052) | Rh | Pd | Ag | Cd | In | Sn SnO ₂ (500) (0.064) | Sb | Te |
| Cs | Ba | La La ₂ O ₃ (200) (0.127) | Hf HfO ₂ (500) (0.055) | Ta Ta ₂ O ₅ (500) (0.11) | W WO ₃ (200) (0.1) | Re | Os | Ir | Pt | Au | Hg | Tl | Pb | Bi | Po |
| | | Ce CeO ₂ (800) (0.022) | | | | | | | | | | | | | |

*“Ultra-stable
Long-term cycling”*

■ Alkali metals

■ Alkaline earth metals

■ Lanthanides

■ Post-transition metals

■ Reactive nonmetals

■ Metalloids

■ Transition metals

Figure 4.2.14 Periodic table of reported metal-oxide-based interlayer for LSBs, and their battery performance (cycle life of LSBs and capacity decay retention per cycle).

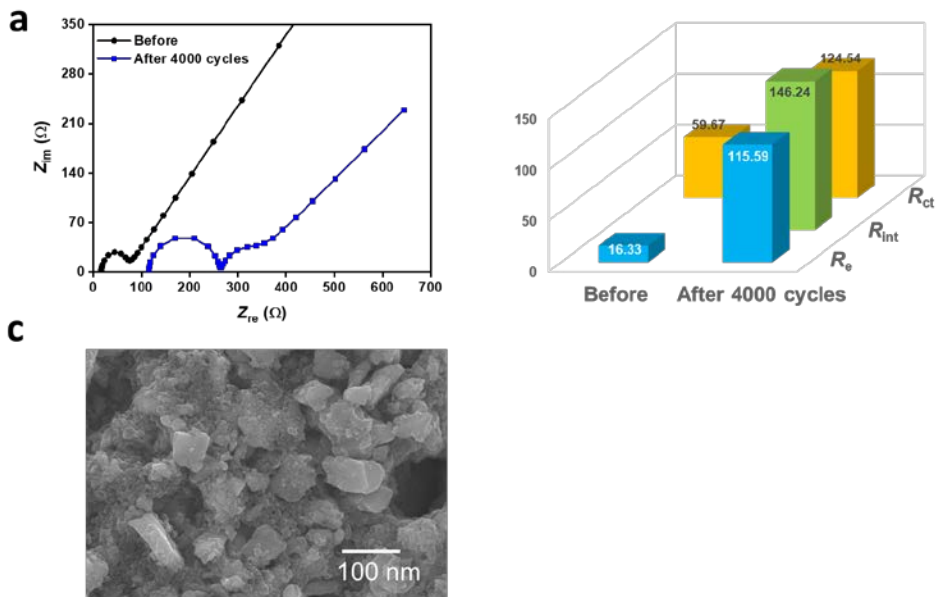


Figure 4.2.15 Electrochemical impedance spectroscopic data of the Li-S cell before and after 4000 cycles. (a) Nyquist plot and (b) detailed data of Fig. S11a. SEM image of prepared G60 interlayer after 4000 cycles (surface, scale bar; 100 nm).

Table 4.2.1 Reported LSB performance with metal-oxide interlayer system

| Metal oxide for interlayer | Specific capacity (mAh g ⁻¹) | Cycle | C-rate | Capacity decay retention per cycle (%) | Ref. |
|------------------------------------|--|------------------------------|------------|--|---|
| NiO | 655 | 100 | 0.1 | 0.400 | ACS Appl. Energy Mater. 2018, 1, 6, 2942-2954 |
| ZnO | 579 | 100 | 0.2 | 0.510 | Nanoscale Research Letters volume 13, Article number: 307 (2018) |
| MgO | 875 | 100 | 0.2 | 0.290 | Nanoscale Adv., 2019, 1, 1589-1597 |
| Y ₂ O ₃ | 816 | 200 | 1.0 | 0.112 | Journal of Solid State Electrochemistry volume 21, pages3229–3236(2017) |
| SiO ₂ | 603 | 200 | 0.2 | 0.050 | ACS Appl. Mater. Interfaces 2017, 9, 8, 7499-7504 |
| La ₂ O ₃ | 720 | 200 | 1.0 | 0.127 | Materials Research Bulletin Volume 94, October 2017, Pages 104-112 |
| WO ₃ | 727 | 200 | 0.5 | 0.100 | Journal of Alloys and Compounds Volume 833, 25 August 2020, 154969 |
| CaO | 873 | 250 | 0.5 | 0.110 | Journal of Materials Chemistry A 2016, 4 (42), 16627-16634 |
| RuO ₂ | 665 | 300 | 0.2 | 0.052 | Chem. Commun., 2016,52, 8134-8137 |
| Al ₂ O ₃ | 730 | 450 | 1.0 | 0.100 | Adv. Funct. Mater. 2018, 28, 1704294 |
| MoO ₃ | ~600 | 500 | 0.5 | 0.120 | Phys. Chem. Chem. Phys., 2020, 22, 2157 |
| Ta ₂ O ₅ | 523 | 500 | 0.2 | 0.110 | Int. J. Electrochem. Sci., 14 (2019) 6628 – 6642 |
| MnO ₂ | 550 | 500 | 1.0 | 0.070 | Nano Lett. 2016, 16, 11, 7276-7281 |
| ZrO ₂ | 570 | 500 | 2.0 | 0.069 | Chemical Engineering Journal Volume 349, 1 October 2018, Pages 376-387 |
| SnO ₂ | 423 | 500 | 0.2 | 0.064 | Journal of Membrane Science Volume 563, 1 October 2018, Pages 380-387 |
| HfO ₂ | 721 | 500 | 1.0 | 0.055 | Carbon 139 (2018) 896-905 |
| V ₂ O ₅ | 441 | 600 | 1.0 | 0.069 | Chemical Engineering Journal Volume 393, 1 August 2020, 124570 |
| CeO ₂ | 838 | 800 | 1.0 | 0.022 | ACS Nano 2019,13,1923 |
| Fe ₃ O ₄ | 356 | 2,000 | 1.0 | 0.024 | ACS Appl. Mater. Interfaces 2018, 10, 31, 26264-26273 |
| Ti ₄ O ₇ | ~200 | 2,500 | 3.0 | 0.030 | Chemical Engineering Journal 355 (2019) 390–398 |
| Ga₂O₃ | 714 613 | 2,000 4,000 | 2.0 | 0.010 0.010 | Our work |

Chapter 5. Conclusions

In this thesis, firstly, a new ReaxFF reactive force field has been developed to describe reactions in the Si-O-H-F system. The ReaxFF force field parameters have been fitted to a quantum mechanical (QM) training set containing structures and energies related to bond dissociation energies, angle and dihedral distortions, and reactions between silicon dioxide and hydrogen fluoride as well as experimental crystal structures, heats of formation and various reaction mechanisms. Model configurations for the training set were based on density functional theory (DFT) calculations on molecular clusters and periodic bulk and surface systems. ReaxFF reproduces accurately the QM training data for structures and energetics of small clusters and surfaces. The results of ReaxFF match reasonably well with those of QM for energies of initial etching process, transition state, and final production process. In addition to this, this force field was applied to etching simulations for silicon dioxide and hydrogen fluoride gas. In etching simulations, silicon dioxide slab models with hydrogen fluoride gas were used in molecular dynamics simulations. The etching yield and number of reaction products with different incident energies of hydrogen fluoride etchant are investigated. For SiO₂ etching, it is found that both the incident energy of etchant gas and temperature are important. Sufficient incident energy plays an important role in etching reaction since dissociation probability of incident molecule and effective collision are affected by incident energy. To successfully simulate etching

reaction, purge process was included in simulation. The etching yield increases with incident energy and temperature.

Secondly, the adsorption energies of LPS with functional binder and functional shield in lithium-sulfur batteries were calculated with DFT method. Before various actual evaluations, the chemical adsorption capacity of the prepared polymer binders composed with chitosan and carboxylated nitrile butadiene rubber (XNBR) for LPS (Li_2S_x , $x = 4, 6, 8$) based on DFT calculations. In addition, the adsorption capability of metal oxides to LPS was investigated by predicting the interaction of the as-prepared metal oxides with LPS with DFT calculations. Calculation included well-known metal oxides for comparison. As a result, with computational method, functional binder and functional shield for enhanced lithium-sulfur batteries were investigated. In this work, from the computational modelling, it is possible to designed binders will provide a new strategy for next generation energy storage that requires fast charging and high-power delivery and a multifunctional gallium oxide shield as an interlayer to regulate the shuttling effect of polysulfide in the sulfur cathode as well as to suppress Li-dendrite growth in Li-anode. This work presents appealing and competitive lithium-sulfur batteries with great potential for stationary storage applications.

Bibliography

F. Jensen, Introduction to Computational Chemistry, Wiley, 2007.

E. G. Lewars, Computational Chemistry, Springer, 2011.

Jung, J.-E.; Barsukov, Y.; Volynets, V.; Kim, G.; Nam, S. K.; Han, K.; Huang, S.; Kushner, M. J. Highly selective Si₃N₄/SiO₂ etching using an NF₃/N₂/O₂/H₂ remote plasma. II. Surface reaction mechanism. *J. Vac. Sci. Technol. A.* **2020**, *38*, 023008.

Tinck, S.; Neyts, E.; Bogaerts, A. Fluorine–silicon surface reactions during cryogenic and near room temperature etching. *J. Phys. Chem. C.* **2014**, *118*, 30315.

Tu Y.-Y.; Chuang, T. J.; Winters, H. F. Chemical sputtering of fluorinated silicon. *Phys. Rev. B.* **1981**, *23*, 823.

Winters, H. F.; Houle, F. A. Gaseous products from the reaction of XeF₂ with silicon. *Journal of Applied Physics.* **1983**, *54*, 1218.

Winters, H. F.; Coburn, J. W. Surface science aspects of etching reactions. *Surf. Sci. Rep.* **1992**, *14*, 162.

- Fortuno, G. Study of reactive ion etching of Si and SiO₂ for CF_xCl_{4-x} gases. *Plasma Chem. Plasma Process.* **1988**, *8*, 19-34.
- Hoshino, T. Etching process of SiO₂ by HF molecules. *J. Chem. Phys.* **1999**, *111*, 2109.
- Kang, J. K.; Musgrave, C. B. The mechanism of HF/H₂O chemical etching of SiO₂. *J. Chem. Phys.* **2002**, *116*, 275.
- Abrams, C.; Graves, D. Molecular dynamics simulations of Si etching by energetic CF₃. *J. Appl. Phys.* **1999**, *86*, 11.
- Barone, M. E.; Graves, D. B. Molecular-dynamics simulations of direct reactive ion etching of silicon by fluorine and chlorine. *J. Appl. Phys.* **1995**, *78*, 6604.
- Ohta, H.; Hamaguchi, S. Molecular dynamics simulation of silicon and silicon dioxide etching by energetic halogen beams. *J. Vac. Sci. Technol. A.* **2001**, *19*, 2373.
- Iwakawa, A.; Nagaoka, T.; Ohta, H.; Eriguchi, K.; Ono, K. Molecular dynamics simulations of Si etching in Cl- and Br-based plasmas: Cl⁺ and Br⁺ ion incidence in the presence of Cl and Br neutrals. *J. Appl. Phys.* **2008**, *47*, 8560.
- Brichon, P.; Despiau-Puno, E.; Joubert, O. MD simulations of low energy Cl_x⁺ ions interaction with ultrathin silicon layers for advanced etch processes. *J. Vac.*

Sci. Technol. A. **2014**, *32*, 021301.

Miyake, M.; Ito, T.; Isobe, M.; Karahashi, K.; Fukasawa, M.; Nagahata, K.; Tatsumi, T.; Hamaguchi, S. Characterization of polymer layer formation during SiO₂/SiN etching by fluoro/hydrofluorocarbon plasmas. *Jpn. J. Appl. Phys.* **2014**, Part 1, *53*, 03DD02.

Nakazaki, N.; Takao, Y.; Eriguchi, K.; Ono, K. Surface smoothing during plasma etching of Si in Cl₂. *J. Appl. Phys.* **2015**, *118*, 233304.

Numazawa, S.; Machida, K.; Isobe, M.; Hamaguchi, S. Molecular dynamics study on fluorine radical multilayer adsorption mechanism during Si, SiO₂, and Si₃N₄ etching processes. *J. Appl. Phys.* **2016**, *55*, 116204.

van Duin, A. C. T.; Dasgupta, S.; Lorant, F.; Goddard III, W. A. Reaxff: a reactive force field for hydrocarbons. *J. Phys. Chem. A.* **2001**, *105*, 9396.

Yang, W.; Mortier, W. J. The use of global and local molecular parameters for the analysis of the gas-phase basicity of amines. *J. Am. Chem. Soc.* **1986**, *108*, 5708.

Chenoweth, K.; van Duin, A. C. T.; Goddard III, W. A. Reaxff reactive force field for molecular dynamics simulations of hydrocarbon Oxidation. *J. Phys. Chem. A.* **2008**, *112*, 1040.

Goken, E. G.; Joshi, K. L.; Russo, Jr, M. F.; van Duin, A. C. T.; Castleman, Jr, A.

W. Effect of formic acid addition on water cluster stability and structure. *J. Phys. Chem. A.* **2011**, *115*, 4657.

Ojwang, J. G. O.; van Santen, R.; Kramer, G. J.; van Duin, A. C. T.; Goddard III, W. A. Predictions of melting, crystallization, and local atomic arrangements of aluminum clusters using a reactive force field. *J. Chem. Phys.* **2008**, *129*, 244506.

LaBrosse, M. R.; Johnson, J. K.; van Duin, A. C. T. Development of a transferable reactive force field for cobalt. *J. Phys. Chem. A.* **2010**, *114*, 18, 5855-5861.

Chenoworth, K.; van Duin, A. C. T.; Persson, P.; Cheng, M.; Oxgaard, J.; Goddard, III, W. A. Development and application of a reaxff reactive force field for oxidative dehydrogenation on vanadium oxide catalysts. *J. Phys. Chem. C.* **2008**, *112*, 14645.

Aryanpour, M.; van Duin, A. C. T.; Kubicki, J. D. Development of a reactive force field for iron–oxyhydroxide systems. *J. Phys. Chem. A.* **2010**, *114*, 6298.

Kim, S. Y.; van Duin, A. C. T. Simulation of titanium metal/titanium dioxide etching with chlorine and hydrogen chloride gases using the reaxff reactive force field. *J. Phys. Chem. A.* **2013**, *117*, 5655-5663.

Rahnamoun, A.; van Duin, A. C. T. Reactive molecular dynamics simulation on the disintegration of Kapton, POSS polyimide, amorphous silica, and Teflon during atomic oxygen impact using the reaxff reactive force-field method. *J. Phys. Chem.*

A. **2014**, *118*, 2780.

Hansen, N. *The CMA evolution strategy: A comparing review. In Towards a new evolutionary computation*, Lazano, J. A.; Larranaga, P.; Inza, I.;

Bengoetxea, E., Springer, Berlin, Heidelberg, 2006; pp 75-102.

Trnka, T.; Tvaroska, I.; Koca, J. Automated training of reaxff reactive force fields for energetics of enzymatic reactions. *J. Chem. Theory Comput.* **2018**, *14*, 291.

ReaxFF 2019.3, SCM, Theoretical Chemistry, Vrije Universiteit, Amsterdam, The Netherlands, <http://www.scm.com>.

ADF 2019.3 SCM, Theoretical Chemistry, Vrije Universiteit, Amsterdam, The Netherlands, <http://www.scm.com>.

Jonsson, H.; Mills, G.; Jacobsen, K. W. *Nudged elastic band method for finding minimum energy paths of transitions. In Classical and Quantum Dynamics in Condensed Phase Simulations*, Berne, B. J.; Ciccotti, G.; Coker, D. F., World Scientific Publishing Company, 1998; pp. 385-404.

Henkelman G.; Jonsson, H. A dimer method for finding saddle points on high dimensional potential surfaces using only first derivatives. *J. Chem. Phys.* **1999**, *111*, 7010.

Henkelman, G.; Uberuaga, B. P.; Jonsson, H. A climbing image nudged elastic band method for finding saddle points and minimum energy paths. *J. Chem. Phys.* **2000**, *113*, 9901.

Kresse, G.; Hafner, J. Ab initio molecular dynamics for liquid metals. *J. Phys. Rev. B.* **1993**, *47*, 558.

Perdew, J. P.; Burke, K.; Ernzerhof, M. Generalized gradient approximation made simple. *Phys. Rev. Lett.* **1996**, *77*, 3865.

Kresse, G.; Hafner, J. Efficiency of ab-initio total energy calculations for metals and semiconductors using a plane-wave basis set. *J. Phys. Condens. Matt.* 1994, *6*, 8245.

Kresse, G.; Joubert, D. From ultrasoft pseudopotentials to the projector augmented-wave method. *Phys. Rev. B.* **1999**, *59*, 1758.

Z. Li, L. Yuan, Z. Yi, Y. Sun, Y. Liu, Y. Jiang, Y. Shen, Y. Xin,

Z. Zhang, Y. Huang, *Adv. Energy Mater.* **2014**, *4*, 1301473.

A. Manthiram, Y. Fu, Y.-S. Su, *Acc. Chem. Res.* **2013**, *46*, 1125.

J. Kim, D.-J. Lee, H.-G. Jung, Y.-K. Sun, J. Hassoun, B. Scrosati, *Adv. Funct. Mater.* **2013**, *23*, 1076.

G. Xu, Q.-b. Yan, A. Kushima, X. Zhang, J. Pan, J. Li, *Nano Energy* **2017**, 31, 568.

X. Liang, C. Y. Kwok, F. Lodi-Marzano, Q. Pang, M. Cuisinier, H. Huang, C. J. Hart, D. Houtarde, K. Kaup, H. Sommer, T. Brezesinski, J. Janek, L. F. Nazar, *Adv. Energy Mater.* **2016**, 6, 1501636.

X. Zhang, Y. Fan, M. A. Khan, H. Zhao, D. Ye, J. Wang, B. Yue, J. Fang, J. Xu, L. Zhang, J. Zhang, *Batteries Supercaps* **2020**, 3, 108.

X. Wang, T. Gao, X. Fan, F. Han, Y. Wu, Z. Zhang, J. Li, C. Wang, *Adv. Funct. Mater.* **2016**, 26, 7164.

R. Tian, S.-H. Park, P. J. King, G. Cunningham, J. Coelho, V. Nicolosi, J. N. Coleman, *Nat. Commun.* **2019**, 10, 1933.

A. Eftekhari, *ACS Sustain. Chem. Eng.* **2017**, 5, 2799.

W. Chen, T. Lei, W. Lv, Y. Hu, Y. Yan, Y. Jiao, W. He, Z. Li, C. Yan, J. Xiong, *Adv. Mater.* **2018**, 30, 1804084.

D. Bresser, D. Buchholz, A. Moretti, A. Varzi, S. Passerini, *Energy Environ. Sci.* **2018**, 11, 3096.

H. Yuan, J.-Q. Huang, H.-J. Peng, M.-M. Titirici, R. Xiang, R. Chen, Q. Liu, Q.

Zhang, *Adv. Energy Mater.* **2018**, 8, 1802107.

O. Galant, S. Bae, M. N. Silberstein, C. E. Diesendruck, *Adv. Funct. Mater.* **2020**, 30, 1901806.

S. Kim, M. Cho, Y. Lee, *Adv. Funct. Mater.* **2020**, 30, 1907680.

L. Ibarra, A. Marcos-Fernández, M. Alzorriz, *Polymer* **2002**, 43, 1649.

E. C. Griffith, V. Vaida, *Proc. Natl. Acad. Sci. U.S.A.* **2012**, 109, 15697.

T. Riaz, R. Zeeshan, F. Zarif, K. Ilyas, N. Muhammad, S. Z. Safi, A. Rahim, S. A. Rizvi, I. U. Rehman, *Appl. Spectrosc. Rev.* **2018**, 53, 703.

X. Fu, L. Scudiero, W.-H. Zhong, *J. Mater. Chem. A* **2019**, 7, 1835.

H. Wang, V. Sencadas, G. Gao, H. Gao, A. Du, H. Liu, Z. Guo, *Nano Energy* **2016**, 26, 722.

L. Zhong, Y. Mo, K. Deng, S. Wang, D. Han, S. Ren, M. Xiao, Y. Meng, *ACS Appl. Mater. Interfaces* **2019**, 11, 28968.

S. Kim, M. Cho, Y. Lee, *J. Mater. Chem. A* **2020**, 8, 10419.

W. C. Oliver, G. M. Pharr, *J. Mater. Res.* **1992**, 7, 1564.

R. H. Y. Subban, A. H. Ahmad, N. Kamarulzaman, A. M. M. Ali, *Ionics* **2005**, *11*, 442.

D. Xu, J. Jin, C. Chen, Z. Wen, *ACS Appl. Mater. Interfaces* **2018**, *10*, 38526.

J. Liang, L. Yin, X. Tang, H. Yang, W. Yan, L. Song, H.-M. Cheng, F. Li, *ACS Appl. Mater. Interfaces* **2016**, *8*, 25193.

H. Zhang, Z. Zhao, Y.-N. Hou, Y. Tang, J. Liang, X. Liu, Z. Zhang, X. Wang, J. Qiu, *J. Mater. Chem. A* **2019**, *7*, 9230.

Z. Deng, Z. Zhang, Y. Lai, J. Liu, J. Li, Y. Liu, *J. Electrochem. Soc.* **2013**, *160*, A553.

S. Kim, M. Cho, Y. Lee, *Adv. Energy Mater.* **2020**, *10*, 1903477.

S. Kim, M. Cho, C. Chanthad, Y. Lee, *J. Energy Chem.* **2020**, *44*, 154.

M. A. Pope, I. A. Aksay, *Adv. Energy Mater.* **2015**, *5*, 1500124.

Y.-J. Li, J.-M. Fan, M.-S. Zheng and Q.-F. Dong, *Energy Environ. Sci.*, 2016, **9**, 1998-2004.

Y.-S. Su and A. Manthiram, *Nat. Commun.*, 2012, **3**, 1166.

P. Albertus, S. Babinec, S. Litzelman and A. Newman, *Nat. Energy*, 2018, **3**, 16-21.

W. Xu, J. Wang, F. Ding, X. Chen, E. Nasybulin, Y. Zhang and J.-G. Zhang, *Energy Environ. Sci.*, 2014, **7**, 513-537.

C. Wang, X. Wang, Y. Wang, J. Chen, H. Zhou and Y. Huang, *Nano Energy*, 2015, **11**, 678-686.

K. Fu, Y. Gong, G. T. Hitz, D. W. McOwen, Y. Li, S. Xu, Y. Wen, L. Zhang, C. Wang, G. Pastel, J. Dai, B. Liu, H. Xie, Y. Yao, E. D. Wachsman and L. Hu, *Energy Environ. Sci.*, 2017, **10**, 1568-1575.

E. Cha, M. D. Patel, J. Park, J. Hwang, V. Prasad, K. Cho and W. Choi, *Nature Nanotechnol.*, 2018, **13**, 337-344.

J.-Q. Huang, Q. Zhang and F. Wei, *Energy Storage Mater.*, 2015, **1**, 127-145.

L. Fan, M. Li, X. Li, W. Xiao, Z. Chen and J. Lu, *Joule*, 2019, **3**, 361-386.

X. Huang, *J. Solid State Electrochem.*, 2011, **15**, 649-662.

X. Liu, J.-Q. Huang, Q. Zhang and L. Mai, *Adv. Mater.*, 2017, **29**, 1601759.

C. J. Orendorff, *Interface Mag.*, 2012, **21**, 61-65.

Z. Zhang, Y. Lai, Z. Zhang, K. Zhang and J. Li, *Electrochim. Acta*, 2014, **129**, 55-61.

X. Tao, J. Wang, C. Liu, H. Wang, H. Yao, G. Zheng, Z. W. Seh, Q. Cai, W. Li, G. Zhou, C. Zu and Y. Cui, *Nat. Commun.*, 2016, **7**, 11203.

J. B. Varley, J. R. Weber, A. Janotti and C. G. V. d. Walle, *Appl. Phys. Lett.*, 2010, **97**, 142106.

Y.-X. Pan, Z.-Q. Sun, H.-P. Cong, Y.-L. Men, S. Xin, J. Song and S.-H. Yu, *Nano Res.*, 2016, **9**, 1689-1700.

A. M. Glass and K. Nassau, *J. Appl. Phys.*, 1980, **51**, 3756-3761.

Y. Wu, L. Huang, X. Huang, X. Guo, D. Liu, D. Zheng, X. Zhang, R. Ren, D. Qu and J. Chen, *Energy Environ. Sci.*, 2017, **10**, 1854-1861.

X. Tang, X. Huang, Y. Huang, Y. Gou, J. Pastore, Y. Yang, Y. Xiong, J. Qian, J. D. Brock, J. Lu, L. Xiao, H. D. Abruña and L. Zhuang, *ACS Appl. Mater. Interfaces*, 2018, **10**, 5519-5526.

N. Syed, A. Zavabeti, M. Mohiuddin, B. Zhang, Y. Wang, R. S. Datta, P. Atkin, B. J. Carey, C. Tan, J. van Embden, A. S. R. Chesman, J. Z. Ou, T. Daeneke and K. Kalantar-zadeh, *Adv. Funct. Mater.*, 2017, **27**, 1702295.

G. Pozina, M. Forsberg, M. A. Kaliteevski and C. Hemmingsson, *Sci. Rep.*, 2017, **7**, 42132.

S. Kim, S. Shirvani-Arani, S. Choi, M. Cho and Y. Lee, *Nano-Micro Lett.*, 2020, **12**, 139.

N. Schneider, M. Frégnaux, M. Bouttemy, F. Donsanti, A. Etcheberry and D. Lincot, *Mater. Today Chem.*, 2018, **10**, 142-152.

Y. Luo, N. Luo, W. Kong, H. Wu, K. Wang, S. Fan, W. Duan and J. Wang, *Small*, 2018, **14**, 1702853.

X. Liang, C. Hart, Q. Pang, A. Garsuch, T. Weiss and L. F. Nazar, *Nat. Commun.*, 2015, **6**, 5682.

W. Kong, D. Wang, L. Yan, Y. Luo, K. Jiang, Q. Li, L. Zhang, S. Lu, S. Fan, J. Li and J. Wang, *Carbon*, 2018, **139**, 896-905.

Y. Zhong, K. R. Yang, W. Liu, P. He, V. Batista and H. Wang, *J. Phys. Chem. C*, 2017, **121**, 14222-14227.

국문 초록

계산화학 방법론을 이용한 표면 반응 모사 및

해석에 관한 연구

서울대학교 대학원

화학생물공학부

김동현

본 박사과정 졸업 논문에서는, 다양한 계산화학 방법론을 통해 규소 산화막의 불화 수소를 통한 식각 공정과 리튬-황 배터리의 구성 요소인 양극재 바인더, 그리고 분리막 코팅 재료와 반응 부산물인 황화 리튬 간의 흡착 에너지에 대한 모델링 및 계산을 수행하였다.

첫 번째로, 규소(Si)-산소(O)-수소(H)-불소(F)를 포함한 식각 공정을 모델링 하기 위해 분자동역학 기법 중 하나인 ReaxFF 힘장을 개발하였다. ReaxFF 힘장 매개 변수는 양자역학 계산을 통해 생성된 물질의

구조, 결합 길이에 따른 에너지, 결합 각 차이에 따른 에너지, 그리고 규소 산화막과 불화 수소 간 반응에 대한 에너지 등의 학습 자료들을 기반으로 다시 구성되었다. 반응 에너지를 위한 계산 자료들은 작은 단위의 분자 모델과 표면 모델로 구성하여 계산하였다. 새로 학습된 ReaxFF 힘장은 양자역학 계산을 통한 분자 모델 및 표면 모델에서 발생하는 식각 공정 메커니즘의 에너지를 잘 모사하였다. 이렇게 새로 개발된 힘장을 통해 불화 수소를 통한 규소 산화막의 식각 공정을 분자동역학을 통해 모사하였다. 이를 통해 주입되는 식각 기체인 불화 수소에 주입되는 초기 에너지에 따른 식각 정도를 식각 수율 및 생성물의 양적 차이를 통해 비교하였다.

두 번째로, 리튬-황 배터리의 구성 요소 중 양극재 바인더와 분리막에 코팅된 금속 산화막의 개선을 통한 배터리 내구성 및 효율 증대를 위해 양자역학 계산 방법론 중 밀도 범함수 이론을 통해 황화 리튬과 구성 요소 간의 흡착 메커니즘 및 에너지를 확인하였다. 실제 실험 및 측정에 앞서, 이론적인 계산화학 방법론을 통해 양극재 바인더인 키토산과 XNBR로 구성된 분자를 모사하고 황화 리튬과의 흡착 메커니즘을 확인하고 흡착 에너지를 계산하였다. 또한, 분리막에 코팅하는 산화막의 종류에 따른 황화 리튬과의 흡착 메커니즘 및 흡착 에너지를 계산하여 최적의 양극재 바인더 및 금속 산화막에 대한 정보를 계산 화학을 통해 규명하고 이를 실험을 통해 확인하였다.